POLITECNICO DI MILANO

School of Industrial and Information Engineering
Master Degree in Engineering Physics

Master of Science Thesis Work

X-ray Emission Spectroscopy to retrieve the local spin moment in 3d transition metal compounds

The particular case of iron

Candidate:
Andrea Carlantuono
Matricola 837318

Thesis advisor:
Prof. Giacomo Claudio Ghiringhelli

Research supervisors:
Doct. Sara Lafuerza
Doct. Pieter Glatzel

Academic Year 2016/2017

"The things you gotta remember are the details.
The details sell your story."

Mentor of Mr. Orange

Reservoir Dogs. Dir. Quentin Tarantino. 1992. Film.

Abstract

A study on a large variety of iron compounds via X-ray Emission Spectroscopy (XES) will be presented in this work. In particular the Kβ and to less extent the Kα emission lines are evaluated as tools to extract quantitative information about the local 3d spin moment. Despite that the Kβ and Kα emission lines arise from core-to-core transitions, they have a strong sensitivity to the spin state which comes from the exchange interaction between the core-hole left in the 3p (Kβ) or 2p (Kα) states and the 3d electrons. The aim of this work was to carry out a systematic study on a wide range of iron compounds in order to understand the role of other factors different from the 3d shell spin like the degree of ionicity/covalency, metallicity, local coordination, etc in the K-emission spectra. We have found significant variations in the Kβ spectra for groups of samples with the same formal oxidation and spin state depending on the ligand, type of coordination or even the metallic character. These spectral changes can be interpreted in term of a reduced 3p-3d exchange interaction due to the delocalization of the 3d states. Using samples with very different nature to perform a calibration between the relevant parameters in the spectra and the nominal spin may lead to wrong conclusions. This result is of fundamental relevance to the scientific community applying K-emission to perform spin-state determination studies.

Sommario

L'obiettivo di questo lavoro è di studiare una vasta gamma di composti del ferro utilizzando la tecnica spettroscopica XES (X-ray Emission Spectroscopy). In particolare le linee di emissione Kβ e Kα sono risultate essere estremamente utili per estrarre informazioni quantitative sul momento locale di spin degli elettroni 3d. Nonostante esse derivano da transizioni core-to-core, hanno comunque un'elevata sensibilità allo spin degli elettroni di valenza mediante l'interazione tra la buca di core nella shell 3p o 2p, rispettivamente, e gli elettroni 3d. Lo scopo di questo lavoro è di effettuare uno studio sistematico in una serie di composti basati sul ferro in modo da poter comprendere meglio il ruolo che hanno fattori differenti dallo spin della shell 3d sulle linee K di emissione, come, per esempio, il grado di covalenza/ionicità del composto, il carattere metallico, la coordinazione locale, ecc. Le conclusioni tratte da questo studio sono applicabili anche alle linee di emissione K di altri metalli 3d. Abbiamo riscontrato variazioni significative negli spettri di emissione Kβ per gruppi di composti con lo stesso stato di ossidazione e di spin a seconda dei diversi ligandi, tipi di coordinazione locale e anche differente carattere metallico/isolante. Queste variazioni spettrali possono essere interpretate in una ridotta interazione di scambio tra gli elettroni 3d e 3p a causa della maggiore delocalizzazione degli orbitali 3d di valenza. Usare campioni di differente natura per una calibrazione tra i parametri rilevanti degli spettri di emissione e il valore nominale di spin può portare a conclusioni errate. Questo lavoro potrà risultare di grande utilità alla comunità scientifica per possibili studi sulla daterminazione dello stato di spin.

Contents

List of Figures

List of Tables

Introduction

During the last 20 years, remarkable and fundamental progress has been made in the field of the so-called inner-shell spectroscopies. They are element specific and concern an incoming x-ray photon which interacts with a given atomic species in the target sample and creates a core-hole, leaving the system in an excited state. This state may decay radiatively, that is emitting a photon. Recording the intensity of these x-rays photons as a function of the emitted energy is called x-ray emission spectroscopy (XES). In particular K-emission spectroscopy has been widely applied to study 3d transition metals compounds due to its strong sensitivity to the metal 3d states. Both Kβ (3p→1s) and Kα (2p→1s) emission lines are useful tools to extract local spin moment information as they are shaped by the 3p-3d and 2p-3d exchange interactions respectively which confer them an indirect sensitivity to the net 3d shell spin. The spin moment sensitivity of the Kβ and Kα emission lines was first established theoretically in early 1960s [1–3] and then was proved experimentally [4–6]. Due to the fact that the 3p-3d interaction is stronger than the 2p-3d, traditionally Kβ spectroscopy has been preferred over Kα for spin-state determination studies. To name a few examples, Kβ XES has been successfully applied for the study of temperature [7], pressure [8] and doping [9] dependent spin state transitions or to derive the spin moment in a series of new Fe-based superconductors [10]. The aim of this work was the study on a large variety of iron compounds in order to get a deeper understanding of the factors influencing the lineshape of Kβ and Kα XES in addition to the nominal spin-state. To achieve this goal we measured a set of more than 30 iron-containing compounds with different oxidation (+2, +3, +4 and mixed-valence), spin state (high spin/low spin and mixed-spin), ligands (fluorides, sulfides, oxides, etc.), local coordination (octahedral, tetrahedral) and different covalent and metallic degrees.

The structure of this thesis is divided into four different chapters. Chapter 1 presents the theoretical background behind the x-ray emission process and introduces the different types of K-emission lines. Chapter 2 is concerned with the basics of the atomic multiplet theory which is necessary to understand the origin of the Kβ and Kα emission lines. Chapter 3 covers the technical aspects about XES experiments in synchrotron radiation facilities and describes the ID26 beamline of the ESRF synchrotron where the experiment was performed. In Chapter 4 the experimental results and their quantitative analysis are presented divided into the Kβ and Kα XES parts. A

last point on conclusions and outlook is presented at the end, where we describe our interpretation of the Kβ and Kα XES analysis and we discuss future possible studies to complement our work.

CHAPTER 1

X-ray emission spectroscopy

In this chapter, we start with a brief introduction about the x-ray-matter interaction, followed by the derivation of the Kramers-Heisenberg equations governing the second order processes (including x-ray emission). Finally, a general overview about the different emission lines will be given.

1.1 Interaction of x-rays with matter

X-rays are defined as the portion of the electromagnetic spectrum with a wavelength λ smaller than the UV radiation. The starting λ after which the radiation is used to be called x-rays is conventionally set around 10 nm. In principle there is no lower limit of x-ray wavelengths, although radiation below 1 pm is usually called gamma radiation. As follows from the well-known equation $E = h\nu$, where h is the Planck's constant and ν is the radiation frequency, the relation between the energy and the wavelength can be expressed as

$$\lambda[\text{Å}] = \frac{hc}{E} = \frac{12.398}{E[\text{keV}]} \tag{1.1}$$

From a quantum mechanical point of view the low energy limit for x-rays is around 100 eV [11] and a further subdivision distinguishes soft x-rays between 100 eV and 3 keV and hard x-rays above 3 keV (see Figure 1.1, where also the different penetration depth depending on the energy is showed). When photons hit a solid many interactions can take place depending on their energy. The cross section quantifies the probability that an interaction will occur and it is defined as [13]

$$\frac{d\sigma}{d\Omega} = \frac{I(\theta, \phi)}{I_0} \tag{1.2}$$

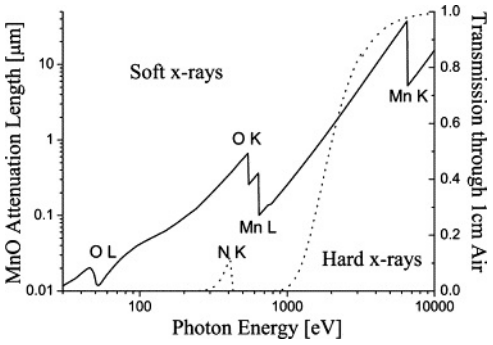

Figure 1.1: *X-rays attenuation length in MnO (solid) and transmission through 1* cm *of air at ambient pressure and room temperature. Figure taken from ref. [12].*

where I_0 is the incident flux of photons and $I(\theta, \phi)$ is the scattered flux in the differential solid angle $d\Omega = \sin\theta d\theta d\phi$. The total cross section is found integrating (1.2) over the full solid angle $\Omega = 4\pi$:

$$\sigma = \oint_{4\pi} \frac{d\sigma}{d\Omega} d\Omega \tag{1.3}$$

As can be seen in Figure 1.2 the interaction which dominates depends on the photon energy. In the x-ray range (going from few eV to hundred of keV) the most important ones are coherent (elastic) and incoherent (inelastic) scattering as well as the photoelectric absorption.

Thomson scattering is an elastic process, meaning that the kinetic energy of the scattered electron and the photon energy do not change as a result of the scattering. The total Thomson cross section from a single electron scattering [14] is

$$\sigma_{coh} \approx \frac{8\pi r_e^2}{3} \tag{1.4}$$

The Thomson formula is, however, inadequate to treat the higher-energy photoelectric and Compton effects. Klein and Nishina [15] derived the scattering cross-section according to Dirac's relativistic theory of the electron [14]:

$$\sigma_{KN} \approx 8\pi r_e^2 \frac{1 + 2k + 1.2k^2}{3(1 + 2k)^2} \tag{1.5}$$

where r_e is the classic electron radius and $k = E/mc^2$ is the photon energy measured in units of the electron rest energy. Thomson scattering can be viewed as the low energy limit $k \to 0$ of the Klein and Nishina formula.

The real difference comes when we deal with atoms. In that case, if the scattering leaves the atom in the ground state, we deal with coherent scattering (i.e. Thomson scattering); whereas if the electron is ejected from the atom, the scattering is incoherent (i.e. Compton scattering). At high energies, the total Compton cross section approaches $\sigma_{incoh} \approx Z\sigma_{KN}$. At low energies and small scattering angles, binding effects are very important: the Compton cross section is significantly reduced and coherent scattering dominates (see Figure 1.2). Compton scattering [16] is an inelastic process between the incoming photon and electrons in the solid. Some energy of the photon is transferred to the recoil electron, which gains kinetic energy and can be emitted

from the material. The overall momentum of the process is conserved because the photon of the remaining energy is scattered with a different angle with respect to the incoming one.

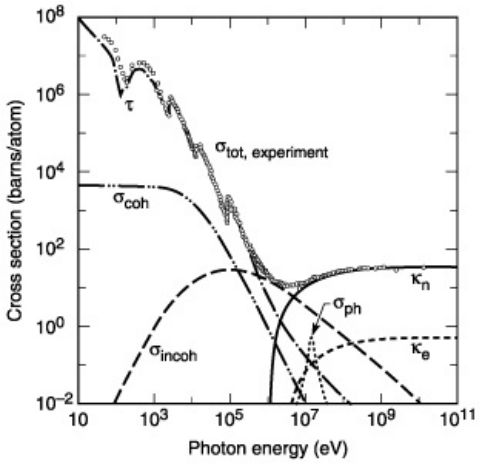

Figure 1.2: *The total experimental cross section σ_{tot} in Pb as a function of the photon energy, showing the contributions from different processes: τ, atomic photo-effect (electron injection, photon absorption); σ_{coh}, coherent scattering (Thomson); σ_{incoh}, incoherent scattering (Compton); κ, pair production; σ_{ph}, photoelectric absorption. Figure taken from ref. [14].*

The last important process that can happen when x-rays interact with matter is the photoelectric effect. When the photons collide with a solid, they transfers some energy to the electrons in it. If the energy of the photon is less than the energy required to remove a core electron from the solid, then an electron will not be ejected, regardless the intensity of the radiation. This effect was discovered by A. Einstein in 1905 [17]. The kinetic energy $E_k = \hbar^2 k^2/2m$ of the ejected electron is given by

$$E_k = h\nu_{inc} - E_B - \phi, \tag{1.6}$$

where E_B is the binding energy of a core level electron (in the case that the incoming radiation $h\nu_{inc}$ is in the x-rays range) and ϕ is the work function (that is the energy needed to remove an electron from a solid, thus is material specific).

1.2 Scattering cross section terms

The scattering process is the first consequence of the x-rays-matter interaction, which is simply schematized in Figure 1.3. An incoming photon defined by its frequency ω_{in}, wavevector $\mathbf{k}_{in}$ and polarisation $\boldsymbol{\epsilon}_{in}$ enters the sample and leaves with ω_{out}, $\mathbf{k}_{out}$ and $\boldsymbol{\epsilon}_{out}$. The angle θ between $\mathbf{k}_{in}$ and $\mathbf{k}_{out}$ is called scattering angle. $\mathbf{q} = \mathbf{k}_{in} - \mathbf{k}_{out}$ and $\hbar\omega_{in} - \hbar\omega_{out}$ define the momentum and energy transfer, respectively. The scattering process is called *inelastic* if $\hbar\omega_{in} \neq \hbar\omega_{out}$ and *elastic* otherwise. For x-rays $k_{in} \sim k_{out}$ [18], so that

$$q \approx 2k_{in} \sin\left(\frac{\theta}{2}\right) \tag{1.7}$$

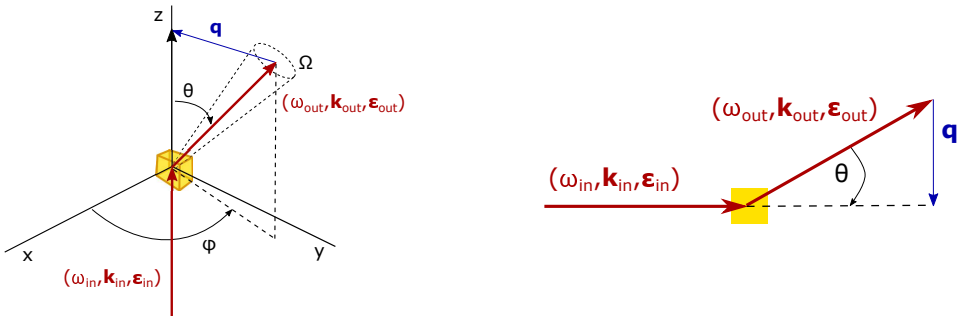

Figure 1.3: *Right: geometry for a scattering process. The angle θ between $\mathbf{k}_{in}$ and $\mathbf{k}_{out}$ is the scattering angle. Ω is the solid angle of the scattered photon. Left: plane view for a fixed φ.*

The momentum transfer depends only on the scattering angle and the incoming wavevector. A quantum mechanical treatment of the scattering of x-rays by matter was done by H. Kramers and W. Heisenberg in 1925. In their famous paper [19] they derived an expression which treats the interaction of the quantized electromagnetic field, which defines the incoming photon and is described by the vector potential $\mathbf{A}(\mathbf{r})$ with the atomic electrons. Following the work of M. Blume [20], we report a brief derivation of the double differential scattering cross sections (DDSCS). The starting point is to consider the total Hamiltonian of the interaction:

$$\begin{aligned}\mathcal{H}_{tot} = &\sum_j \frac{1}{2m}\left(\mathbf{p}_j - \frac{e}{c}\mathbf{A}(\mathbf{r}_j)\right)^2 + \sum_{jj'} V(\mathbf{r}_{jj'}) - \frac{e\hbar}{2mc}\sum_j \mathbf{s}_j \cdot \nabla \times \mathbf{A}(\mathbf{r}_j) \\ &+ \frac{e\hbar}{2(mc)^2}\sum_j \mathbf{s}_j \cdot \mathbf{E}(\mathbf{r}_j) \times \left(\mathbf{p}_j - \frac{e}{c}\mathbf{A}(\mathbf{r}_j)\right) + \sum_{\mathbf{k}\lambda} \hbar\omega_k \left(c^\dagger_\lambda(k)c_\lambda(k) + \frac{1}{2}\right) = \\ &= \mathcal{H}_1 + \mathcal{H}_2 + \mathcal{H}_3 + \mathcal{H}_4 + \mathcal{H}_5 \end{aligned} \tag{1.8}$$

where $\mathbf{E} = -\nabla\Phi - \frac{1}{c}\dot{\mathbf{A}}(\mathbf{r}_j)$ (Φ is the Coulomb potential) describes the electric field of the radiation, $\mathbf{r}_j$, $\mathbf{s}_j$ and $\mathbf{p}_j$ are the electron position, spin and momentum operators and $V(\mathbf{r}_{jj'})$ is the scalar potential describing the electron repulsion. The sum over j runs over all the electrons.

The terms not depending on $\mathbf{A}(\mathbf{r})$ in (1.8), that is the $\mathbf{p}$-dependent part of $\mathcal{H}_1$ and $\mathcal{H}_2$, can be

included in the non-interacting part, $\mathcal{H}_0$. The other two terms represent the Zeeman interaction ($\mathcal{H}_3$) and the spin-orbit interaction ($\mathcal{H}_4$). The last term ($\mathcal{H}_5$) contains the creation and annihilation operators. The overall Hamiltonian can be simplified omitting the linear terms in $\mathbf{A}(\mathbf{r})$[1] and the Zeeman term, motivated by the fact that the magnetic x-ray scattering cross section is smaller by $(\hbar\omega/mc^2)^2$ with respect to the charge scattering one [22]. These simplifications lead to the following Hamiltonian:

$$\mathcal{H} = \mathcal{H}_0 + \mathcal{H}_i + \mathcal{H}_R, \tag{1.9}$$

where the non-interacting part is

$$\mathcal{H}_0 = \sum_j \frac{1}{2m}\mathbf{p}_j^2 + \sum_{jj'} V(\mathbf{r}_{jj'}), \tag{1.10}$$

the interacting part is

$$\mathcal{H}_i = \sum_j \frac{e^2}{2mc^2}\mathbf{A}^2(\mathbf{r}_j) - \frac{e}{mc}\mathbf{A}(\mathbf{r}_j)\cdot\mathbf{p}_j = \mathcal{H}_a + \mathcal{H}_b. \tag{1.11}$$

and the part relative to radiation is

$$\mathcal{H}_R = \sum_{\mathbf{k}\lambda} \hbar\omega_k \left(c_\lambda^\dagger(k)c_\lambda(k) + \frac{1}{2} \right) \tag{1.12}$$

The scattering cross section can be calculated assuming the system in an initial ground state $|1\rangle$ which is an eigenstate of $\mathcal{H}_0$ with energy E_1 and a photon $(\mathbf{k}, \lambda)$. Then the probability of a transition induced by $\mathcal{H}_i$ to a state $|2\rangle$ with a single photon $(\mathbf{k}', \lambda')$ can be calculated, taking into account the photon-electron interaction. The transition probability rate is given by the Fermi's golden rule (to the second order):

$$w = \frac{2\pi}{\hbar}\left| \langle 2;\mathbf{k}'\lambda'|\mathcal{H}'|1;\mathbf{k}\lambda\rangle + \sum_n \frac{\langle 2;\mathbf{k}'\lambda'|\mathcal{H}'|n\rangle\langle n|\mathcal{H}'|1;\mathbf{k}\lambda\rangle}{E_n - E_1} \times \delta(E_2 - E_1) \right|^2, \tag{1.13}$$

with

$$|g\rangle = |1;\mathbf{k}\lambda\rangle; \quad |f\rangle = |2;\mathbf{k}'\lambda'\rangle; \quad E_1 = E_g + \hbar\omega_{in}; \quad E_2 = E_f + \hbar\omega_{out},$$

where $|g\rangle$, $|n\rangle$, $|f\rangle$ denote the ground, intermediate and final states with energy E_g, E_n and E_f, respectively. The δ function ensures the energy conservation between the final and ground state. Rewriting, knowing that $\mathcal{H}_1$ contributes to the first order and $\mathcal{H}_2$ to the second order, we have:

$$w = \frac{2\pi}{\hbar}\left| \langle f|\mathcal{H}_a|g\rangle + \sum_n \frac{\langle f|\mathcal{H}_b|n\rangle\langle n|\mathcal{H}_b|g\rangle}{E_n - E_g - \hbar\omega_{in}} \times \delta(E_f - E_g - \hbar(\omega_{in} - \omega_{out})) \right|^2, \tag{1.14}$$

The DDSCS $d^2\sigma/d\Omega dE$ is defined as the number of incident photons scattered with a given energy and momentum within an energy range dE and a solid angle $d\Omega$. In our process, which is

[1] spin-orbit correction $\mathcal{H}_4$ of the unperturbed Hamiltonian $\mathcal{H}_{unp} = \sum_j \frac{1}{2m}\mathbf{p}_j^2 + \sum_{jj'} V(\mathbf{r}_{jj'})$ is already smaller by the square of the fine structure constant, $\mathcal{H}_4/\mathcal{H}_{unp} \approx \alpha^2$ [21].

described with the standard notation for incoming and outgoing photon with wavevector, energy and polarisation $(\mathbf{k}_{in}, \hbar\omega_{in}, \boldsymbol{\epsilon}_{in})$- $(\mathbf{k}_{out}, \hbar\omega_{out}, \boldsymbol{\epsilon}_{out})$, we can write the DDSCS as [23]

$$\left(\frac{d^2\sigma}{d\Omega dE}\right) = w\frac{\rho(E_f)}{J_0}, \tag{1.15}$$

where $\rho(E_f)$ is the density of final states of scattered particles, J_0 is the incident flux and w is the rate of transition between initial and final states. For zero mass particles, the latter two quantities can be written as:

$$\rho(E_f) = \frac{V_0}{(2\pi)^3}\frac{\omega_{out}^2}{\hbar c}, \quad J_0 = \frac{c}{V_0},$$

where V_0 is the quantization volume. If we include the transition probability given by the Fermi's golden rule and we expand the vector potential [20] we finally get the expressions for the non-resonant (NR) and resonant (R) DDSCSs. The first order term $\mathcal{H}_a$ (proportional to $\mathbf{A}^2$) dominates far from any resonance and leads to the non-resonant scattering cross section:

$$\left(\frac{d^2\sigma}{d\Omega dE}\right)_{NR} = r_0^2\frac{\omega_{out}}{\omega_{in}}|\boldsymbol{\epsilon}_{in}\cdot\boldsymbol{\epsilon}_{out}|^2\sum_f\left|\langle f\left|\hat{O}\right|g\rangle\right|^2\delta(E_f - E_g - \hbar(\omega_{in}-\omega_{out})) =$$
$$= r_0^2\frac{\omega_{out}}{\omega_{in}}|\boldsymbol{\epsilon}_{in}\cdot\boldsymbol{\epsilon}_{out}|^2 S(\mathbf{q}, \omega_{in}-\omega_{out}) \tag{1.16}$$

with

$$\hat{O} = \sum_i e^{i\mathbf{q}\cdot\mathbf{r}_i},$$

where $r_0 = \frac{e^2}{mc^2}$ is the classical electron radius. The momentum transfer $\mathbf{q} = \mathbf{k}_{in} - \mathbf{k}_{out}$ appears in the exponential function connecting the final and ground state. $S(\mathbf{q}, \omega_{in} - \omega_{out})$ is the dynamical structure factor and relates NR scattering process to the excitations of the electron system allowed by energy and momentum conservation. (1.16) describes NR Raman, Compton and Thomson scattering. Since the synchrotron radiation is naturally linearly polarized, the dot product between incoming and outgoing polarization gives an angular dependence of:

$$\sin^2\phi + \cos^2\theta\cos^2\phi. \tag{1.17}$$

The second order term $\mathcal{H}_b$ (proportional to $\mathbf{A}\cdot\mathbf{p}$) becomes dominant when the incoming energy is tuned to the vicinity of a absorption edge[2], leading to the resonant cross section, which is known as the Kramers-Heisenberg equation:

$$\left(\frac{d^2\sigma}{d\Omega dE}\right)_R = r_0^2\frac{\omega_{out}}{\omega_{in}}\sum_f\left|\sum_n\frac{\langle f|\hat{O'}^\dagger|n\rangle\langle n|\hat{O}|g\rangle}{E_n - E_g - \hbar\omega_{in} - i\Gamma_n/2}\right|^2$$
$$\times\,\delta(E_f - E_g - \hbar(\omega_{in}-\omega_{out})) \tag{1.18}$$

[2]The total absorption coefficient tends to infinity [24].

with

$$O'^{\dagger} = \sum_{j'} (\boldsymbol{\epsilon}^*_{out} \cdot \mathbf{p}_{j'}) e^{-i\mathbf{k}_{out}\cdot\mathbf{r}_{j'}} \quad \text{and} \quad O' = \sum_{j} (\boldsymbol{\epsilon}^*_{in} \cdot \mathbf{p}_{j}) e^{-i\mathbf{k}_{in}\cdot\mathbf{r}_{j}}. \tag{1.19}$$

The sums run over all the final and intermediate states. As in (1.14), the δ function requires the energy transfer equal to the energy difference in the system. The process described by (1.18) is the excitation of the system in the ground state $|g\rangle$ due to the absorption of a photon, leading the system to an intermediate state $|n\rangle$ with a core-hole. The intermediate state decays with a lifetime τ_n by the emission of a photon (radiative decay) or an electron (Auger decay). The denominator of (1.18) contains a Lorentzian profile in which the linewidth $\Gamma_n = \hbar/\tau_n$ accounts for the finite lifetime broadening of the intermediate state. A second Lorentzian can be added to consider also the finite lifetime τ_f of the final state replacing the δ function in (1.18)[3] [25]:

$$\delta(E_f - E_g - \hbar(\omega_{in} - \omega_{out})) \rightarrow \frac{\frac{\Gamma_f}{2\pi}}{(E_f - E_g - \hbar(\omega_{in} - \omega_{out}))^2 + \Gamma_f^2/4} \tag{1.20}$$

The photoionization process may lead to several $|n\rangle$ intermediate states that can interfere with each other [26] and all contribute to the emission process described by (1.18). This interference can change spectral intensities but not the energies of the transition. If we simplify and ignore the interference effect and consider only the lowest intermediate state we end up with the simplified Kramers-Heisenberg equation:

$$\left(\frac{d^2\sigma}{d\Omega dE}\right)_R \approx r_0^2 \frac{\omega_{out}}{\omega_{in}} \sum_f \sum_n \frac{\left|\langle f|\hat{O'^{\dagger}}|n\rangle\right|^2 \left|\langle n|\hat{O}|g\rangle\right|^2}{(E_n - E_g - \hbar\omega_{in})^2 + \Gamma_n^2/4} \times \frac{\frac{\Gamma_f}{2\pi}}{(E_f - E_g - \hbar(\omega_{in} - \omega_{out}))^2 + \Gamma_f^2/4} \tag{1.21}$$

When the incident energy $\hbar\omega_{in}$ is tuned close to an absorption edge, we have an excited intermediate state with a hole in the core level. There are usually referred to as "resonant" excitations. The terms Resonant Inelastic X-ray Scattering (RIXS) or Resonant X-ray Spectroscopy (RXES) describe this process. When the incident energy is tuned well above an absorption edge and the emitted energy is scanned over a fluorescence line, we have the Non-Resonant X-ray Emission Spectroscopy (NRXES) or simply XES. Nevertheless, both of them are second order processes because they involve the presence of an intermediate state and are described by (1.21). The process behind X-ray Raman Scattering (XRS) is described by the non-resonant term, i.e. by (1.16). But XRS can be also used to study an absorption edge and thus can be a "resonant" excitation. This adds some odds to the term "resonant", which has to be used with care depending on the theoretical background. According to this definition also when the incoming energy is tuned well above an absorption edge we have a "resonant" process, because it's in any case described by (1.21).

[3] Other corrections include convolution by Gaussian functions to account for the experimental finite resolution and incident energy bandwidth.

1.3 X-ray emission process

We now provide an introduction to non-resonant XES, which is the technique used in our study. As mentioned before, XES is described by the Kramers-Heisenberg resonant cross section, but actually it is not a "resonant" process because the incident energy is tuned well above the absorption edge of the element of interest. There is no fundamental difference for excitation close or well above a resonance level, so the formalism of (1.21) can be used with some modifications to treat this process. The cross section within the first tenths of eV above an absorption edge shows a $1/E^3$ dependence [27]. Hence we can say that for this range the photoelectron (described by its energy ϵ), does not interact with the remaining ion. The intermediate and final state can be then written as $|n\rangle = |n';\epsilon\rangle$, $E_n = E_{n'} + \epsilon$ and $|f\rangle = |f';\epsilon\rangle$, $E_f = E_{f'} + \epsilon$ (Figure 1.4). Then, for each intermediate and final state n' and f' an infinite possible number of states characterized by the kinetic energy of the photoelectron can be achieved.

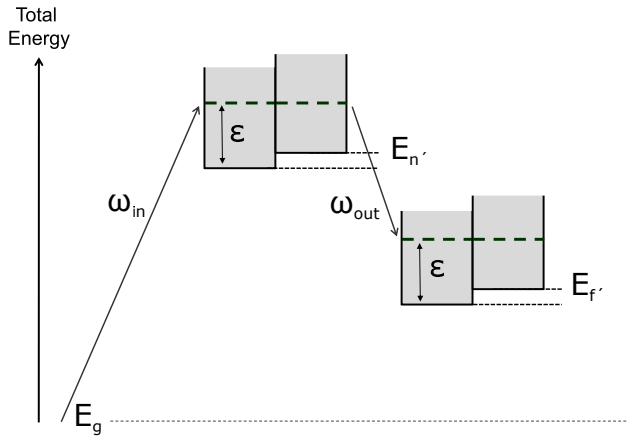

Figure 1.4: *Simple total energy description for XES. A continuum of intermediate and final states is reached whose energies depends on the photoelectron kinetic energy ε. Figure taken from ref. [27].*

Equation (1.21) becomes:

$$\left(\frac{d^2\sigma}{d\Omega dE}\right)_R \propto \sum_{f'}\sum_{n'}\left|\langle f';\epsilon|\hat{O'^{\dagger}}|\epsilon;n'\rangle\right|^2\left|\langle n';\epsilon|\hat{O'}|g\rangle\right|^2 \times \int_\epsilon \frac{1}{(E_g-(E_{n'}+\epsilon)+\hbar\omega_{in})^2+\Gamma_n^2/4} \times \int_\epsilon \frac{\Gamma_f/2\pi}{((E_{f'}+\epsilon)-E_g-\hbar(\omega_{in}-\omega_{out}))^2+\Gamma_f^2/4}. \quad (1.22)$$

The integral over all the possible photoelectron energies is a convolution of two Lorentzian with width $\Gamma_n + \Gamma_f$, which takes into account the intermediate and final state energy broadening. This spectral energy broadening is independent of the incident energy because the photoelectron kinetic energy does not influence the convoluted Lorentzian.

In XES the system under study is excited with an energy sufficient to remove a core electron, leaving the system in an intermediate excited state with a core-hole, which is immediately filled ($\tau \sim 10^{-15}$ s [28]) by an electron of an outer shell. This process results in an emission of an electron or a x-ray photon. The former process is called Auger emission and is not treated in this

work. The latter is the x-ray fluorescence emission and is what is thesis is mainly about.

The exponential part of the transition operator $\hat{O}$ which govern the transitions can be expanded as:

$$e^{i\mathbf{k}\cdot\mathbf{r}} \sim 1 + i\mathbf{k}\cdot\mathbf{r} - \frac{1}{2}(\mathbf{k}\cdot\mathbf{r})^2 + ... \tag{1.23}$$

We recall that $\mathbf{k}$ is the (incoming or outgoing) photon propagation wavevector and $\mathbf{r}$ is the spacial coordinate of the electron. Considering only the unity term of (1.23) leads to treating the interaction between the electromagnetic field with an electron in the dipole approximation which implies the selection rule $\Delta l = \pm 1$ for the atomic angular momentum. Keeping also the second term of (1.23) leads to the electric quadrupole approximation (magnetic dipole terms are negligible in the x-ray range [29]) with the selection rule $\Delta l = 0, \pm 2$. The matrix elements associated with quadrupole electric transition are of the order of the fine structure constant $\alpha \sim 1/137$, much smaller than the electric dipole ones and thus are difficult to observe.

K-shell fluorescence lines result from the emission of photons after the creation of a 1s core-hole. Similarly, photons emitted after the creation of a 2s or 2p core-hole form the L-shell emission spectrum. The two fluorescence types lead to different total energy broadenings and fluorescence yields, depending on the lifetime of the core-hole. The yield represents the probability of a core-hole in the K or L shell to be filled by radiative process, in competition with non-radiative processes (including Auger). In this work we measured only the K-fluorescence lines, which have a higher yield, compared to the L-shell fluorescence (see Figure 1.5). There are several K-emission lines

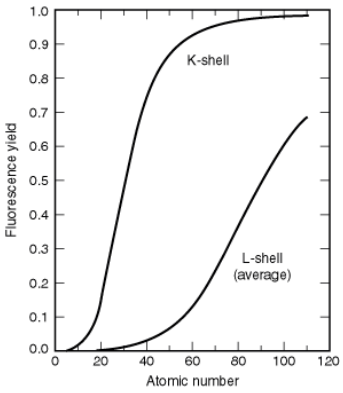

Figure 1.5: *Fluorescence yield for K and L shells for different atomic numbers. Figure taken from ref. [14].*

depending on from which shell the electron decays to fill the 1s core-hole. Figure 1.6 summarizes all the possible K-emission lines. The strongest are the Kα lines, which arise from 2p to 1s transitions and are split by the 2p spin-orbit interaction into a doublet ($K\alpha_1$ and $K\alpha_2$). Approximately eight times weaker are the Kβ mainlines, also called core-to-core (CTC) Kβ lines, which result from 3p to 1s transitions. Finally, approximately 500 times weaker, are the Kβ satellites, which arise from transitions to the 1s shell from valence orbitals[4] and are also called valence-to-core (VTC) Kβ lines for this reason.

[4]The valence orbitals are metal-ligand hybridized states.

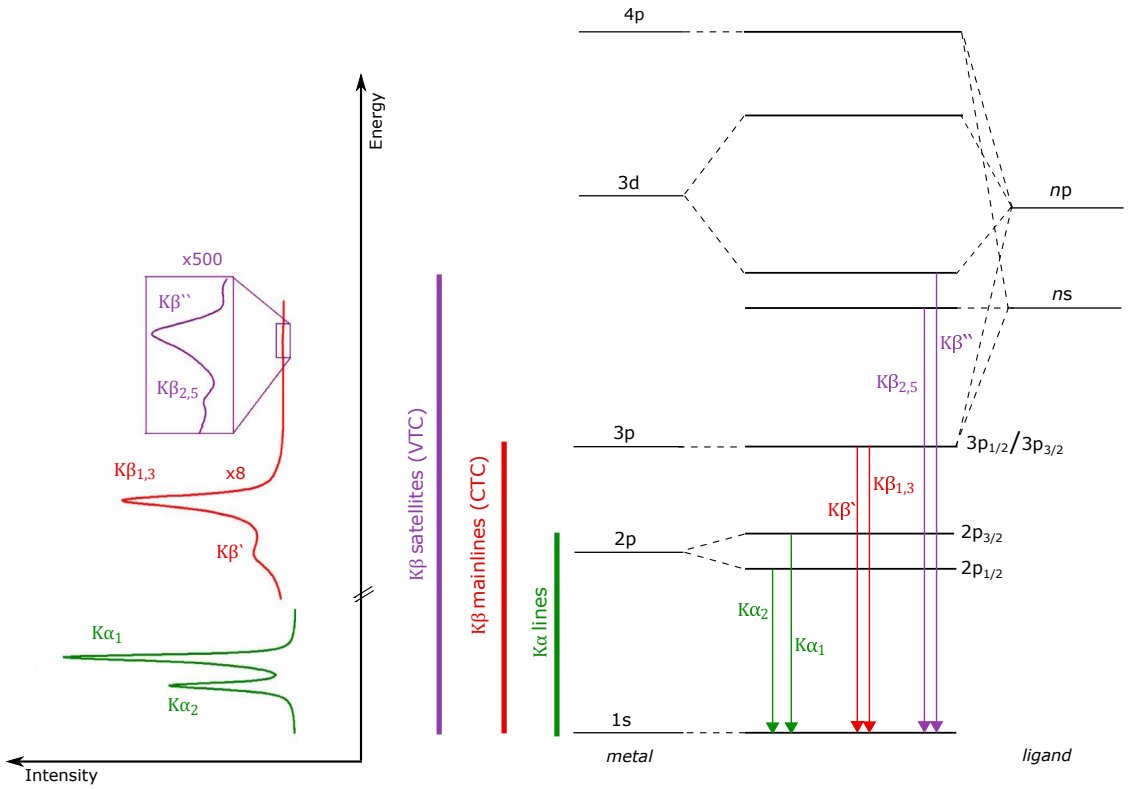

Figure 1.6: *Left: spectral shape of the different emission lines. Right: one electron picture of the different K-emission lines.*

CHAPTER 2

The physics behind the K-emission mainlines

2.1 Basics of Atomic Multiplet Theory

Some basics of the atomic multiplet theory will be discussed in this section, following the analysis of F. de Groot and A. Kotani [11]. The starting point to understand the shape of the core-level spectra (including emission spectra) is to understand the way how the core-hole is created in the absorption process affects the whole electronic system. This completely localized approach makes possible to treat in detail the core-hole, but is not sufficient to fully understand the ground state of a solid, which requires an more itinerant and general approach. The atomic Hamiltonian $\mathcal{H}_{atom}$ for an N-electrons system is:

$$\mathcal{H}_{atom} = \sum_N \frac{\mathbf{p}_i^2}{2m} + \sum_N \frac{-Ze^2}{\mathbf{r}_i} + \sum_{ij} \frac{e^2}{\mathbf{r}_{ij}} + \sum_N \zeta(\mathbf{r}_i) l_i \cdot s_i, \tag{2.1}$$

where the first term contains the kinetic energy of the N electrons, the second is the electrostatic interaction of the N electrons with the nuclear charge Z, the third is the electron-electron repulsion ($\mathcal{H}_{ee}$) and the last term is the spin-orbit coupling ($\mathcal{H}_{ls}$). The kinetic and electrostatic terms are the same for a given atomic configuration and they define the average energy of a certain state. The difficulty to solve the Schrödinger equation using the atomic Hamiltonian is that $\mathcal{H}_{ee}$ is too large to be treated as a perturbation. Therefore one needs to introduce the *central field approximation*, in which the spherical average of the electron-electron interaction is separated from the non-spherical part. The modified $\mathcal{H}_{ee}$ is written as:

$$\mathcal{H}_{ee}^{cf} = \mathcal{H}_{ee} - \langle \mathcal{H}_{ee} \rangle = \sum_{ij} \frac{e^2}{\mathbf{r}_{ij}} - \left\langle \sum_{ij} \frac{e^2}{\mathbf{r}_{ij}} \right\rangle \tag{2.2}$$

At the end only $\mathcal{H}_{ee}^{cf}$ and $\mathcal{H}_{ls}$ determine the energies of the different levels within a given atomic configuration. A specific notation called *term symbol* $^{2S+1}L_J$ is used to label te different electronic symmetry configurations, which are determined by their orbital angular moment L, spin moment S and total moment J (which can go from $J_{min} = |L - S|$ to $J_{max} = L + S$ in steps of 1). The orbital moment is labelled with the letters S, P, D, F, G, etc. which correspond to L=0, 1, 2, 3, 4, etc. The term symbol is a short notation which gives all the three quantum numbers and so determines the symmetry and the energy of a certain atomic configuration. For example a single 1s electron has L=0, S=1/2 and J=1/2. This is written with a term symbol $^2S_{1/2}$. A 2p electron has two possible symmetries $^2P_{1/2}$ and $^2P_{3/2}$ depending on the spin-orbit coupling. A $3d^1$ configuration is a 10-fold degenerate and has term symbols $^2D_{5/2}$ and $^2D_{7/2}$. In the absence of the spin-orbit coupling, all terms with the same L and S have the same energy and the total degeneracy is $(2L + 1)(2S + 1)$. When the spin-orbit coupling is important, all terms are split in energy to their J-values with a degeneracy of $2J+1$. The usual approach to solve the Hamiltonian is to distinguish when the spin-orbit coupling is important or not, giving either the jj-coupling and the LS-coupling, respectively. This because the spin-orbit coupling commutes only with J. For valence electrons usually spin orbit coupling is small (especially in light elements) and we can neglect $\mathcal{H}_{ls}$ and use the pure LS-coupling. For the heavier atoms we have to include the spin-orbit coupling in the description of the ground state. For example, for a core-hole not interacting with other electrons the spin orbit coupling is larger than electrostatic interactions and pure jj-coupling has to be used. However, in many cases, an intermediate coupling is necessary.

Coupling schemes For K-shell XES on transition metals (TMs) the important ground state is $3d^n$, while the final state can be either a 2p or a 3p hole[1]. For more than one electron configuration the total L is given by the sum of the individual l values. For example for a $2p^2$ configuration we have a total $L = l_1 + l_2 = 2$ and $S = 1/2 + 1/2 = 1$. The total degeneracy of the state is 15. Taking into account the magnetic quantum numbers $m_l = -1, 0, 1$ and $m_s = -1, 0, 1$ the term symbols can be derived depending on their combinations, which corresponds to the possible arrangements of the 2 electrons in the shell. One can start from the state with total $L = 2$ and $S = 0$, which gives a ^1D term symbol. Moreover, this state generate pairs of total (M_l, M_s)= (2,0), (1,0), (0,0), (-1,0) and (-2,0) according to $M_l = -2, -1, 0, 1, 2$ and $M_s = 0$. Such arrangements are all ^1D term symbols. Proceeding with $L = 1$, but $S = 1$ we have the ^3P term, belonging to all the couples (M_l, M_s)= (1,1), (1,0), (1,-1), (0,1), (0,0), (0,-1), (-1,1), (-1,0) and (-1,1). The last term symbol ^1S corresponds to $L = 0$ and $S = 0$ and the only way to arrange the electrons is with (M_l, M_s)=(0,0). The relative degeneracy are: 5, 3, 1 for ^1D, ^3P, ^1S, respectively. Including J we have the values $^1D_2$, $^1S_0$, $^3P_2$, $^3P_1$, $^3P_0$. The possible arrangements of the electrons obey to the Pauli exclusion principle. However, the latter does not have to be satisfied when we found the term symbol for a mixed configuration, for example a 2p3p has 6x6 possible terms [11]. To calculate the term symbols of a mixed configuration we have to multiply individually each term symbol. This operation is indicated with $A \otimes B$, which gives the possible $|L_A - L_B| \leq L \leq L_A + L_B$ and $|S_A - S_B| \leq S \leq S_A + S_B$ values. For $^2P \otimes {}^2P$, this gives to $L = 0, 1, 2$ and $S = 0, 1$ with term

[1]The principal quantum number has no effect on the term symbols, which are the same, for example, for a 2p or 3p hole.

symbols ^1S, ^1P, ^1D, ^3S, ^3P, ^3D with their degeneracies summing up to 36. For the d electrons we have up to 10 degenerate position of each state. The degeneracy of a $3d^2$ configuration is $10 \times 9/2 = 45$, where 9 arises from the Pauli exclusion principle (only 9 possible states after adding the second electron) and the division by two to account for the fact that the sequence of the quantum states for the 2 electrons makes no difference. A $3d^3$ configuration has 120 different states, i.e. $10 \times 9/2 \times 8/3$. The general formula to determine the degeneracy of a $3d^n$ configuration is:

$$\binom{10}{n} = \frac{10!}{(10-n)!n!} \tag{2.3}$$

The degeneracies can be also calculated by sorting the different M_l and M_s values according to the Pauli exclusion principle. A useful example for K-shell XES is that of the $np^5 3d^5$ final state, which is the one involved in the Kβ and Kα emission lines for a $3d^5$ system. The total degeneracy is given by:

$$6 \times \binom{10}{5} = 6 \times \frac{10!}{5!\,5!} \tag{2.4}$$

(2.4) gives 1512 possible states, which are divided into 205 term symbols[2], which can be determined with the product $^2P \otimes {}^6D$. This implies, in principle, 205 possible final states. As we will see later in this chapter, dipole selection rules limit the number to only three possible final states which are crucial to understand Kβ mainline emission spectra.

Matrix elements The energies of each configuration can be estimated computing the matrix elements of the atomic Hamiltonian $\mathcal{H}_{atom}$, omitting the kinetic term and the interaction with the nucleus, which are equal for all the electrons, as already explained. We restrict ourselves only to the matrix elements of the electron-electron interaction. Because $\mathcal{H}_{atom}$ commutes with L^2, S^2, L_Z, S_z the off-diagonal terms are all zero. A simple example is a 1s2s configuration consisting of ^1S and ^3S terms. The respective energies are:

$$\langle {}^1S|\frac{e^2}{\mathbf{r}_{12}}|{}^1S\rangle = F^0(1s2s) + G^0(1s2s), \tag{2.5}$$

$$\langle {}^3S|\frac{e^2}{\mathbf{r}_{12}}|{}^3S\rangle = F^0(1s2s) - G^0(1s2s) \tag{2.6}$$

F^0 and G^0 are the Slater parameters for direct Coulomb repulsion and Coulomb exchange interaction, respectively. The main result can be stated as follows: "the singlet and the triplet states are split by the exchange interaction and the energy difference between the two configurations is $2G^0(1s2s)$" [11]. An analogous result can be obtained for a 1s2p state for which triplet and singlet states are split by $2/3G^0(1s2p)$. The general formulation of the matrix elements for two electrons is the following:

$$\langle {}^{2S+1}L_J|\frac{e^2}{\mathbf{r}_{12}}|{}^{2S+1}L_J\rangle = \sum_k f_k F^k + \sum_k g_k G^k \tag{2.7}$$

[2] All term symbols for a $np^5 3d^n$ configuration can be found at pag. 104 of ref. [11].

f_k and g_k are the angular parts and can be calculated with the angular momentum coupling [11]. This result is obtained separating F^k and G^k with the Wigner-Eckhart theorem [30]. Expression (2.7) is used to calculate the different energies of the term symbols of a given electronic configuration and is a key factor to understand the origin of the different emission lines and to predict their shapes with computational methods.

2.1.1 Ligand Field Multiplet Theory

The next step towards a real $3d^n$ atomic system is to mimic the environment in which the metal ion is, which can be done by approximating the TM ion surrounded by a distribution of charges. This approach is treated by the Crystal Field Theory (CFT), which describes the breaking of the orbital degeneracy in TM complexes due to the presence of the ligands which are approximated as point charges. Starting with the spherical (SO_3) ideal symmetry of a free ion, the real ligand environment is considered by branching from spherical symmetry to the local symmetry. Most of the 3d TMs have either octahedral (O_h) or tetrahedral (T_d) symmetry, which consists in the TM cation surrounded by 6 ligand atoms on the vertex of an octahedron or 4 ligands on the vertex of a tetrahedron, respectively (Figure 2.1). Table 2.1 gives the branching rules[3] for the symmetry elements from the SO_3 atomic group[4] to the O_h and T_d subgroups. From these rules we can say the following for an O_h environment symmetry: (i) S symmetry remains the same, a non degenerate orbital (label "A") with all the symmetry operations. (ii) P symmetry became triply degenerate (label "T") and antisymmetric with respect to the center of inversion (subscript "u"). (iii) D symmetry branches to E_g and T_{2g} orbital symmetries, respectively 2 non-degenerate and 3 degenerate, all symmetric with respect to the inversion[5]. The same is found for a T_d symmetry, with the only differences in the absence of the inversion symmetry and the slightly different branching for the P symmetry.

Table 2.1: *Branching rules in the Mulliken notation [31] for the symmetry elements going from spherical (SO_3) to octahedral (O_h) and tetrahedral (T_d) symmetries.*

SO_3	O_h	T_d
S	A_{1g}	A_1
P	T_{1u}	T_2
D	E_g+T_{2g}	E+T_2

To determine which symmetry of the d orbitals has lower energy in a ligand environment some simple electrostatic considerations are needed. In Figure 2.1 the spatial arrangement of the d orbitals in both O_h and T_d environment is given together with the ligand positions. In an O_h environment the CF splits the 3d levels into low-lying t_{2g} and high-lying e_g levels. The t_{2g} levels result lower in energy because the lobes of the 3d orbitals point in between the ligand p orbitals and the electrostatic repulsion is minimized. In an T_d environment, on the contrary, e levels fall

[3] Determined from group theory [30].
[4] SO_3 is the group of all rotation about the origin in 3 dimensions.
[5] A more detailed explanation of the symmetry classes can be found at ref. [30, 31].

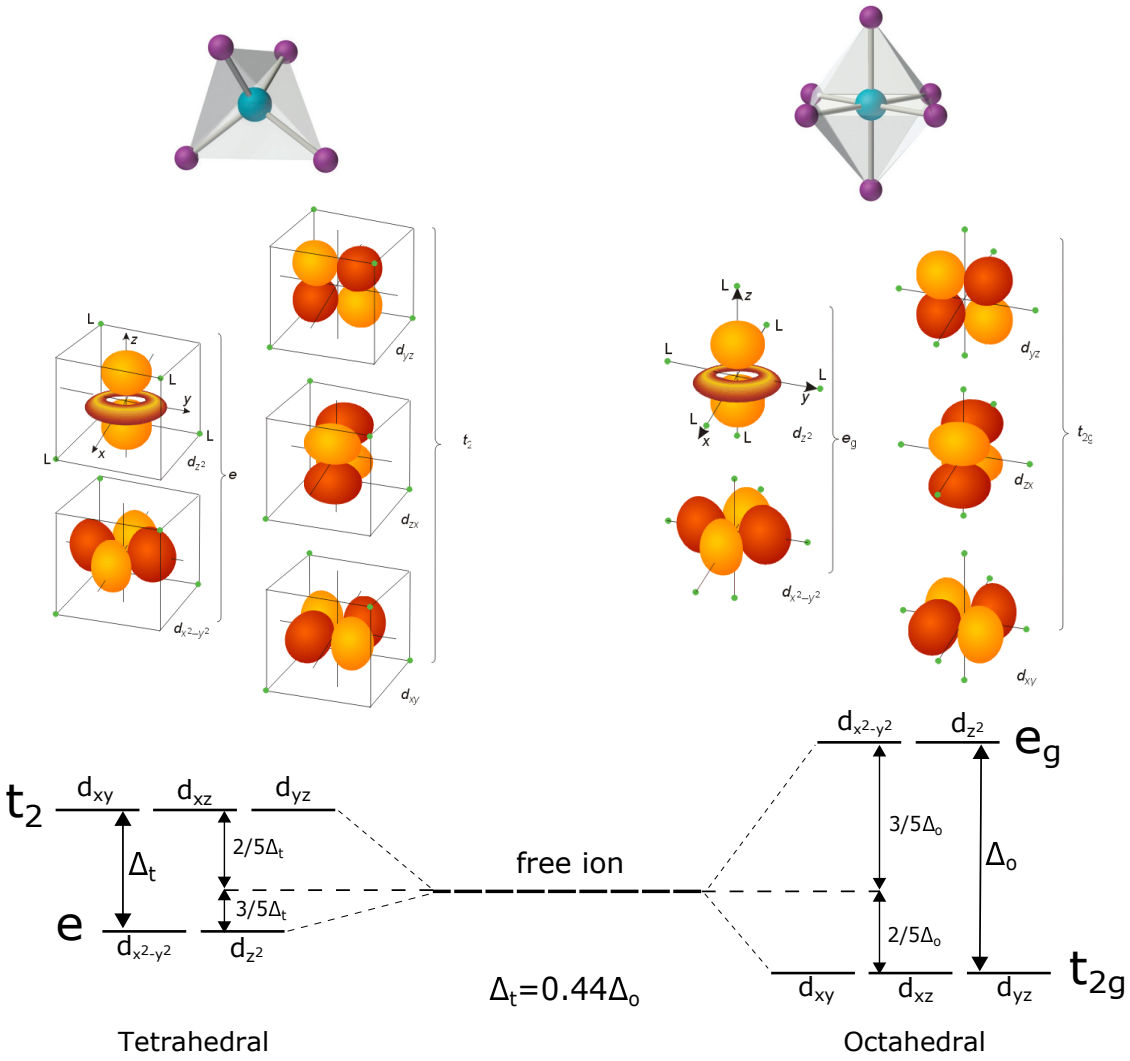

Figure 2.1: *Upper part: T_d and O_h environments with the metal cation (light blue) in the center. The violet spheres represent the ligands. Middle part: spatial arrangement of the d orbitals in a T_d and O_h environments. Green points represent the ligands. Lower part: CF splitting of the d levels in T_d and O_h environments.*

lower in energy. In an O_h symmetry the crystal field depends on a unique parameter Δ_o (also referred to $10D_q$), defined as the average separation between the split d orbitals, t_{2g} and e_g. In the case of T_d environment the crystal field splitting parameter is still unique, but smaller, as explained hereafter. The reason can be understood simply thinking that in a T_d environment there are only four ligands (compared to the six of the O_h case), hence the splitting is roughly 2/3 of the octahedral one. Another reduced 2/3 factor has to be added because the direction of the ligand approach in T_d environment does not coincide with the d-orbitals (see Figure 2.1). The resulting splitting is $\Delta_t = 2/3 \times 2/3\Delta_o \sim 0.44\Delta_o$. The crystal field splitting depends on the nature of the ligands, on the charge of the metal ion and whether the metal is a 3d, 4d or 5d element. The so-called spectrochemical series list the ligands and metal ions according to their capacity to modify the crystal filed energy splitting. Following the Hund's rule the lowest lying levels (t_{2g} or e in O_h and T_d cases, respectively) have to be filled first. However, the precise order in which the

orbitals are filled depends on the competition between the crystal field energy and the Coulomb energy cost of putting two electrons in the same orbital, i.e. the 3d-3d exchange interaction (also named pairing energy). If the crystal field is lower than the pairing energy (weak-field case) the electron will first singly occupy each orbital before any orbital becomes doubly occupied and the system is said to be in a high-spin (HS) state. Conversely, if the crystal field energy is larger than the pairing one (strong-field case), electrons will first doubly occupy the lower energy orbitals before occupying the higher energy levels and a low-spin (LS) state is reached. In Table 2.2 we summarize the different configurations for the Fe ion with formal oxidation state +2, +3 and +4 in O_h and T_d symmetries, which are the main cases subject of study in this work.

Table 2.2: *Iron ground state electronic configuration and spin values for different high-spin and low-spin cases and oxidation state, ranging from +2 to +4 in an O_h and T_d symmetry environment.*

Fe ion oxidation state	**Sym.**	**Spin state**	**Ground state configuration**	**Local spin moment**
Fe^{2+}	O_h	HS	$t_{2g\uparrow}^3\, t_{2g\downarrow}\, e_{g\uparrow}^2$	2
Fe^{2+}	O_h	LS	$t_{2g\uparrow}^3\, t_{2g\downarrow}^3$	0
Fe^{3+}	O_h	HS	$t_{2g\uparrow}^3\, e_{g\uparrow}^2$	5/2
Fe^{3+}	O_h	LS	$t_{2g\uparrow}^3\, t_{2g\downarrow}^2$	1/2
Fe^{4+}	O_h	HS	$t_{2g\uparrow}^3\, e_{g\uparrow}$	2
Fe^{4+}	O_h	LS	$t_{2g\uparrow}^2\, t_{2g\downarrow}^2$	0
Fe^{2+}	T_d	HS	$e_{\downarrow}\, e_{\uparrow}^2\, t_{2\uparrow}^3$	2
Fe^{2+}	T_d	LS	$e_{\downarrow}^2\, e_{\uparrow}^2\, t_{2\downarrow}\, t_{2\uparrow}$	0
Fe^{3+}	T_d	HS	$e_{\uparrow}^2\, t_{2\uparrow}^3$	5/2
Fe^{3+}	T_d	LS	$e_{\downarrow}^2\, e_{\uparrow}^2\, t_{2\uparrow}$	1/2
Fe^{4+}	T_d	HS	$e_{\uparrow}^2\, t_{2\uparrow}^2$	2
Fe^{4+}	T_d	LS	$e_{\downarrow}^2\, e_{\uparrow}^2$	0

From an energetic point of view, in a 3d TM, the crystal field is treated as a perturbation and is stronger than the spin-orbit coupling but can be either stronger or weaker than electron-electron interaction. One usually refers to these two cases as strong and intermediate crystal field, respectively. The crystal field Hamiltonian consists in an additional term $\mathcal{H}_{CF} = -e\phi(\mathbf{r})$ in the atomic Hamiltonian (2.1), which is simply the electronic charge e times a potential that describes the surroundings, $\phi(\mathbf{r})$. The latter can be expanded in terms of spherical harmonics Y_{LM}:

$$\phi(\mathbf{r}) = \sum_{l=0}^{\infty} \sum_{m_l=-l}^{+l} \mathbf{r}^l A_{LM} Y_{LM}(\psi, \phi) \tag{2.8}$$

What and how many terms keep in the expansion depends on the specific environment symmetry. For example in a high symmetry as in the case of an O_h environment all terms containing $\mathbf{r}$ in odd power vanishes. The crystal field is treated as a perturbation of the atomic multiplet results, meaning that is necessary to determine the matrix elements of $\phi(\mathbf{r})$ with respect, for example, to

the 3d orbitals, thus it is necessary to compute $\langle 3d|\phi(\mathbf{r})|3d\rangle$. The matrix elements can be separated into a radial part and a spherical part. The former gives the strength of the crystal field interaction and the latter can be completely written in spherical symmetry using the angular momentum coupling already mentioned for the atomic multiplets [11]. The main success of the Ligand Field Multiplet Theory (LFMT) is that most of the explained properties are determined by symmetry considerations. Group theory [30] makes possible a close link from the atomic multiplet theory to the LFMT by simply "translating" the results obtained in the atomic symmetry (spherical) to cubic symmetry (O_h or T_d) and further symmetries to any other lower symmetry point group. The crystal field effect modifies the energies of the atomic multiplets, according to the different expansion of the crystal field term in the Hamiltonian. The diagrams which give the energies with respect to the normalized cubic crystal field are known as Sugano-Tanabe diagrams. For example, Figure 2.2 gives the energy levels for a $3d^5$ configuration in O_h symmetry. The ground state is ^6S and has a A_{1g} symmetry. Increasing the crystal field Δ the ground state becomes T_{2g} (arising from the fall in energy of the ^2I excited state symmetry). For states to cross each other or not, it depends whether their symmetries allow them to form linear combinations.

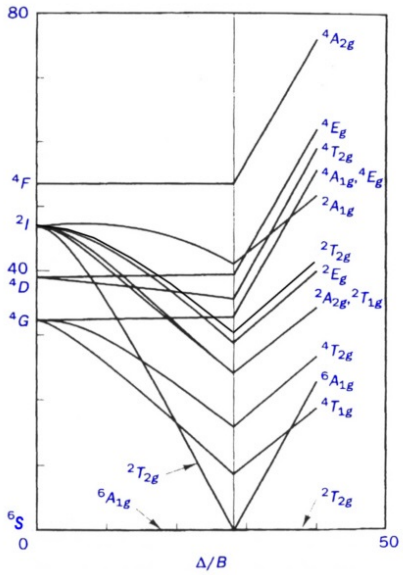

Figure 2.2: *Sugano-Tanabe diagram in a O_h symmetry for a $3d^5$ configuration. Image taken from ref. [32].*

2.1.2 Charge Transfer Multiplet Theory

Until now we have considered the metal ligands only in terms of local geometry and ligand field splitting. The atomic multiplet and LFM theory use a single configuration to describe the ground state and the final state. For a more quantitative treatment, charge fluctuations between the ground and final states have to be included. The physics behind can be described by a few parameters, namely the on-site dd Coulomb repulsion U_{dd}, the charge transfer energy Δ, the ligand p-TM d hybridization energy $V(\Gamma)$ (where Γ is the ligand molecular orbital) and the core-hole potential $-U_{dc}$. Two additional term in the Hamiltonian have to be added, leading to the following

expression for the charge-transfer (CT) Hamiltonian [11, 33]:

$$\mathcal{H}_{CT} = \sum_{\Gamma,\sigma} \epsilon_\Gamma a^\dagger_{\Gamma\sigma} a_{\Gamma\sigma} + \sum_{\Gamma,\sigma} V(\Gamma)(a^\dagger_{d\Gamma\sigma} a_{\Gamma\sigma} + a^\dagger_{\Gamma\sigma} a_{d\Gamma\sigma}), \tag{2.9}$$

where $a^{(\dagger)}_{\Gamma\sigma}$ and $a^{(\dagger)}_{d\Gamma\sigma}$ are the electron annihilation (creation) operators for ligand molecular orbital Γ with spin σ and for a 3d state (Γ, σ), respectively. ϵ_Γ is the band dispersion of the orbital Γ. The first term adds energy to the ligand orbitals, while the second term represents the metal-to-ligand hopping. An electron is created at the metal site and annihilated at the ligand and vice versa. The summation Γ runs over the branched representations (e.g. t_{2g} and e_g in a O_h symmetry) and over all the possible spin states σ. Two hopping terms exist in octahedral surrounding, one with hybridization energy $V(E_g)$ which mixes wavefunctions with E_g symmetry (d_{z^2} and $d_{x^2-y^2}$) in case of d orbitals) and $V(T_{2g})$ which mixes the T_{2g} symmetries. From the Coulomb repulsion energy considerations done previously, one can expect a stronger mixing[6] for E_g symmetry because the ligands are located on the octahedron axes. In the final state the core-hole potential is added:

$$\mathcal{H}_{CT_f} = \mathcal{H}_{CT} - U_{dc} \sum_{\Gamma,\sigma} \epsilon_\Gamma a^\dagger_{d\Gamma\sigma} a_{d\Gamma\sigma} \tag{2.10}$$

As an example, we can describe the simple case with two configurations, $3d^n$ and $3d^{n+1}\underline{L}$ (L underlined denotes a hole in the ligand orbitals), neglecting the Γ dependence on ϵ_Γ and $\epsilon_{d\Gamma}$, i.e. neglecting the ligand field splitting. The charge transfer energy is defined as $\Delta = E(d^{n+1}\underline{L}) - E(d^n) = \sum_\Gamma \epsilon_\Gamma - n\epsilon_d$, considering E the energy of the lowest energy atomic configuration in the charge transfer model. The Hamiltonian can be written in the 2x2 matrix form between the ground state $|3d^n\rangle$ and the CT state $|3d^{n+1}\underline{L}\rangle$ as [33, 35][7]

$$\mathcal{H}_{CT} = \begin{pmatrix} E_0 & V_{eff} \\ V_{eff} & E_0 + \Delta \end{pmatrix} \tag{2.11}$$

In the final state the core-hole potential can be added substituting $\Delta \to \Delta_f \equiv \Delta - U_{dc}$. The effective potential V_{eff} depends on the environment symmetry and, for example for a O_h symmetry, can be written as a combination of $V(E_g)$ and $V(T_{2g})$. The ground state energy term is written as $E_0 = n\epsilon_d + \sum_\Gamma \epsilon_\Gamma$.

[6] Band structure calculations gives $V(E_g) \sim 2V(T_{2g})$ [34].
[7] Neglecting spin-orbit and two electron Coulomb interaction.

2.2 Spectral shape of Kβ and Kα emission lines

The fine structure of the Kβ and Kα emission lines is due to two main interactions:

- The *spin-orbit interaction*, i.e. the interaction of the electron spin with its own orbital moment. This quantum mechanics effect splits the Kα line by $\sim$ 10 eV into a $K\alpha_1$ and $K\alpha_2$ doublet (removing the degeneracy on the orbital momentum) while the Kβ lines are split by less than 1 eV (accordingly, and due to the fact that the exchange interaction is dominant as explained later, one does not observe the $K\beta_1$-$K\beta_3$ splitting [26]). This different value for the splitting can be understood by looking at the spin-orbit Hamiltonian term

$$\mathcal{H}_{so} = \zeta\, \mathbf{S}\cdot\mathbf{L}, \tag{2.12}$$

  where $\zeta = \frac{e^2}{8\pi\epsilon_0 m^2 c^2}\frac{1}{r^3}$. The $\langle\frac{1}{r^3}\rangle$ expectation value can be approximated with the Kramers relation [21] with hydrogen-like radial wavefunctions, obtaining the $1/n^3$ dependence. Thus, as shown in Table 2.3 for a Mn^{2+} ion, the resulting splitting is almost ten times larger for a 2p level.

- The *exchange interaction*, i.e. the electron-electron interaction due to wavefunctions exchange symmetry. For a simple case of two electrons, the exchange interaction term [36] can be written as[8]:

$$\mathcal{H}_{exc} = -2J_{1,2}\,\mathbf{S}_1\cdot\mathbf{S}_2 \tag{2.13}$$

  In our case this is the interaction between the 2p (or 3p) electrons and the valence electrons, which even though indirectly, makes Kα (and Kβ) sensitive to the valence shell. In the framework of the atomic multiplet theory, the magnitude of the exchange interaction is quantified as the values of Slater exchange integrals (Table 2.3). For a 3p hole the Slater integrals are almost 3 times larger than a 2p hole because of the larger 3p-3d orbital wavefunctions overlap.

Table 2.3: *Spin-orbit parameters (ζ) and Slater integrals (G) both in* eV *for a Mn^{2+} ion ($3d^5$) with a given core-hole electron configurations. Values taken from ref. [12].*

Slater integral	Interaction	$2p^5 3d^5$	$3p^5 3d^5$
ζ_d	spin-orbit	0.06	0.05
ζ_p	spin-orbit	6.85	0.80
G^1_{pd}	exchange	5.18	15.40
G^3_{pd}	exchange	2.85	9.30

We can conclude that the shape of the Kβ emission lines is dominated by the 3p-3d exchange interaction, while the Kα lines are mainly shaped by the 2p spin-orbit interaction. In the following section we discuss in more detail and separately first for the Kβ and then for the Kα lines the mechanisms that shape the spectra and make them chemically sensitive.

[8] Dirac pointed out that the critical features of the interaction can be obtained neglecting a first spin-independent term.

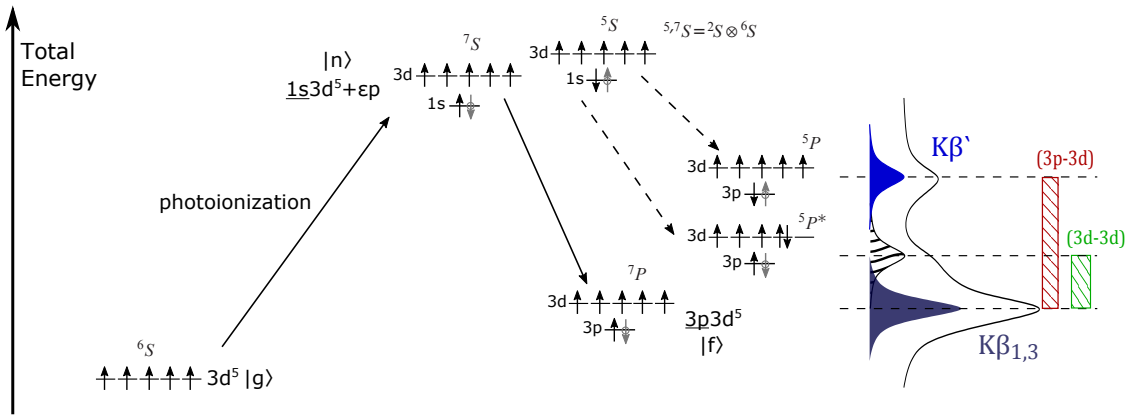

Figure 2.3: *Kβ emission process for the case of a $3d^5$ ion. $|g\rangle$, $|n\rangle$, and $|f\rangle$ denote the ground, intermediate and final states, respectively. Term symbols are indicated. The 3p paired electrons leading zero angular momentum are not displayed, while grey arrows indicate holes. Exchange interactions are indicated with dashed colored boxes.*

2.3 Kβ emission lines

There are two mechanisms that influence the spectral shape of the Kβ emission lines depending on the valence electron configuration [26]: one is (i) the screening of the core-hole potential which depends on the valence charge density. The resulting shift as a function of the formal oxidation state and covalency degree can be very small, but still observable; the second is (ii) the electron-electron interactions between the valence electrons and the open core-shell. The dominant interaction for the Kβ final state with a $3p^5 3d^n$ configuration is the 3p-3d exchange interaction. The Kβ spectrum is composed by a main intense peak, named $K\beta_{1,3}$ and a low energy shoulder, the Kβ'. The satellite peak Kβ' has a complete spin-polarized origin, which can be explained in the framework of the atomic multiplet theory (already introduced in the previous section). To illustrate its origin we consider a $3d^5$ ion. Figure shows the Kβ emission process in a configuration scheme for this particular case. From a $3d^5$ ion (^6S symmetry) one can obtain, by the application of the cross product $^2S \otimes {}^6S$, the intermediate symmetry mixed states ^5S and ^7S (other charge transfer intermediate states are ignored for simplicity, but can be included in a more advanced charge-transfer multiplet theory treatment [37]). The final states are split into "spin-polarized" configurations $\underline{3p}^{\uparrow}3d^{\uparrow}$ and $\underline{3p}^{\downarrow}3d^{\uparrow}$ (underlined denotes a 3p hole), according to the two possible spin orientations of the 3p hole. The only two possible final states admitted by the dipole selection rule are the ^5P and ^7P symmetries, leading to the Kβ' satellite and the $K\beta_{1,3}$ peak. An additional state $^5P^*$ can be reached if the spin of the 3p hole changes together with one spin in the 3d shell. This spin-flip state (which is due to non-diagonal matrix elements [26]) is responsible for the small shoulder at low energies in the main peak $K\beta_{1,3}$ and is related to the different ordering of the 3d electrons with respect to the ground state. We can conclude that the Kβ peaks can be separated into internal spin-up and spin-down transitions (referring to the 3p hole spin in the final state): the main peak $K\beta_{1,3}$ primarily comes from spin-down transition, while the satellite Kβ' arises from almost 100% spin-up transitions. All the term symbols involved in the process are sorted in energy according to the Hund's rules: the lowest in energy are term symbols with (1) maximum

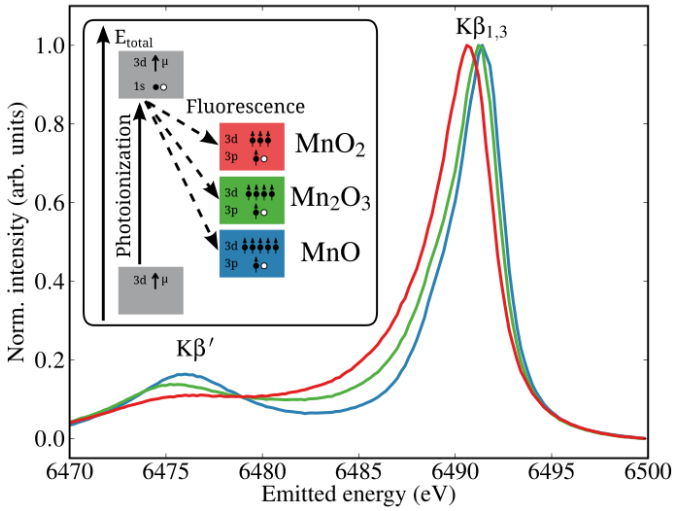

Figure 2.4: *Comparison of the Kβ XES spectra in a series of Mn oxides. The inset shows this evolution in terms of total energy with paired electrons omitted. Figure taken from ref. [27].*

S, (2) maximum L. The ^6S state lies lower in energy because the core-hole is not present.

Different approaches have been proposed to relate the Kβ emission lines features to the nominal spin state of the 3d shell electrons in a quantitative way. K. Tsutsumi [1] [4] as an approximated approach used the spin $\mathbf{S}$ of the incomplete 3d shell and $s = 1/2$ spin of the 3p incomplete shell in the final state resulting from a 3p to 1s transition (assuming a totally quenched orbital angular momentum, which is justified in 3d TMs). The total spin $(\mathbf{S} + \mathbf{s})$ exchange interaction is given by [36]:

$$-\frac{1}{2}J(1 + 4\mathbf{S}\cdot\mathbf{s}), \tag{2.14}$$

where J is the exchange integral between the electrons in the 3p and 3d shells. The magnitude of the energy difference between the exchange interaction for $\mathbf{S} + 1/2$ and $\mathbf{S} - 1/2$ is:

$$\Delta E = J[(\mathbf{S} + 1/2)(\mathbf{S} + 1/2 + 1) - [(\mathbf{S} - 1/2)(\mathbf{S} - 1/2 + 1)] = J(2\mathbf{S} + 1) \tag{2.15}$$

The splitting between the Kβ$_{1,3}$ and Kβ' peaks can be approximated by this expression. K. Tsutsumi also derived the following expression for the intensity ratio of the two peaks which can be estimated from the ratio of the $2S + 1$ spin multiplicity of the two states:

$$\frac{I_{K\beta'}}{I_{K\beta_{1,3}}} = \frac{2(\mathbf{S} - 1/2) + 1}{2(\mathbf{S} + 1/2) + 1} = \frac{\mathbf{S}}{(\mathbf{S} + 1)} \tag{2.16}$$

The Kβ lines are therefore a probe of the local spin magnetic moment in the 3d shell through the intra-atomic 3p-3d exchange interaction, which is particularly interesting for 3d TM compounds. Because Kβ XES is sensitive to the local spin moment of individual ions it does not rely on long-range magnetic order and thus the application of a magnetic field is not required. In addition, since it is a hard x-rays technique it has bulk sensitivity and it is compatible with demanding sample environments [27]. In Figure 2.4 are showed as example the spectra of three Mn-oxides with different nominal spin values. A shift to lower energies of the Kβ$_{1,3}$ peak together with a decrease

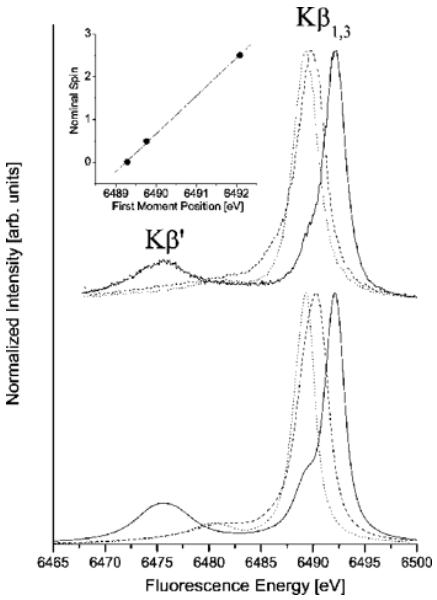

Figure 2.5: *Upper part: experimental Kβ spectra for $^{55}Fe_2O_3$ (solid line), $K_3\,^{55}Fe(CN)_6$ (dashed line), $K_4\,^{55}Fe(CN)_6$ (dotted line) measured after K-capture. Lower part: LFM simulations for the three compounds. Figure taken from ref. [12].*

of the Kβ' feature is observed with decreasing the nominal spin (S, S_{MnO}=2.5 → S_{MnO_2}=2).

About the core-hole screening effects is useful to do some additional considerations. Figure 2.5 shows ligand field multiplet simulations including the charge transfer effects for different compounds compared with experimental K-capture spectra. They measure the same emission lines but recorded after an alternative method of excitation, the radioactive electron capture decay [38]. This nuclear process (close to the β decay) involves the capture of an orbital 1s electron by the nucleus with the decrease of the nuclear charge Z by 1 and the emission of a neutrino: $Z^A + e^- \rightarrow (Z-1)^A + \nu_e$. In the emission after K-capture, when the 1s vacancy is filled by a 3p electron, the effective nuclear charge experienced by the 3d electrons can be assumed to remain unchanged and the core-hole-d-electron Coulomb attraction Q_{cd} is almost completely canceled by the decrease in the atomic number Z. Hence the K-capture spectra should be free from the different Q_{cd} due to the different valence charge density. This is not true for the spectra recorded after photoionization, where Q_{cd} can change the relative order of the different charge transfer configurations [39]. The best agreement with the experiments was achieved assuming the same final state $3p^5 3d^n$ for all of the compounds, meaning that the center-of-gravity of the entire multiplet was set to equal values in all three calculations. This means that the shift of the $K\beta_{1,3}$ peak is not caused by the different screening due to the variation of the valence charge density between different oxidation states (and covalent character), but almost entirely by the 3p-3d exchange splitting. This result will be taken into account in our experimental results analysis where we will perform an alignment of the spectra to have the same center-of-gravity in order to isolate the 3p-3d exchange interaction effects.

2.3.1 Covalency effect

The 3p-3d exchange interaction and the different screening of the core-hole can be also affected by the different covalency degree of the compounds. Even though the Kβ XES spectra results from an intra-atomic interaction, also other factors like degree of covalency of the Fe-ligand bond may influence the spectral shape. This type of spectral differences were already reported by [12, 40–43]. Two different approaches to account for the covalency will be given. (1) Considering charge transfer effects between between the ground and the two main final states of the Kβ emission process in terms of "bonding combinations". Starting from a $3d^5$ ground state we have:

$$\begin{aligned} |g\rangle &= \cos\alpha|3d^5\rangle - \sin\alpha|3d^6\underline{L}\rangle \\ |f\rangle_{bond} &= \cos\beta|3d^5\rangle - \sin\beta|3d^6\underline{L}\rangle \\ |f\rangle_{antibond} &= \cos\beta|3d^5\rangle + \sin\beta|3d^6\underline{L}\rangle. \end{aligned} \tag{2.17}$$

The angle parameters that define the population ratio of the ground and final states depend on the energy difference between $|3d^n\rangle$, $|3d^{n+1}\underline{L}\rangle$ (i.e. Δ) and on the mixing potential V_{eff}. The population degree in the two states can be expressed with "covalency parameters" γ:

$$\begin{aligned} \gamma_g &= \tan\alpha = f(V_{eff}, \Delta) \\ \gamma_f &= \tan\beta = f(V_{eff}, \Delta_f). \end{aligned} \tag{2.18}$$

These quantities represent the strength of the covalency mixing and they can change from 0 (no covalency mixing) to 1 (maximum covalency mixing). The result of accounting charge transfer effects is that the mixture of the states in the ground and final configurations can lead to additional states (which are forbidden if the charge transfer effects are not accounted for) and thus modify the shape of the emission lines. The valence electrons delocalization with the increasing covalency has to be taken into account by changing the charge transfer energy Δ, that we recall is the energy difference between the two configurations $|3d^n\rangle$ and $|3d^{n+1}\underline{L}\rangle$. In a covalent TM compounds the valence electrons are delocalized over the cation and the ligands, making the hop process of the electrons from the ligand to the metal more energetically favourable. This has to be taken into account by reducing Δ. Successful ligand field charge transfer calculations [33], [37] shows the broadening of the Kβ' shoulder and a decreasing of the $K\beta_{1,3}$ intensity. From the multiplet diagram of Figure 2.3, accounting for the charge transfer effects a spin flip event can occur also in the ligand orbital giving an additional triplet final state ^3P.

(2) The covalency can be also described in an electron density picture: increasing the covalency means that the electron cloud is more distributed around the metal ion and the ligands [12]. This spread of the spatial distribution of the electron cloud reflects into a decreasing of the Slater exchange integrals. The type of covalency mentioned is called "central field covalency" and consists in the distortion of the metal d orbital radial wave functions due to the ligand bonding [44]. Pollock et al. [43] approximate the impact of covalency on the Kβ emission lines in a molecular orbital picture by adding the ligand character ($(1-\alpha)$ in (2.19)) to the metal d wavefunctions:

$$\psi_{3d} \sim \alpha\phi_{3d} + (1-\alpha^2)^{1/2}\phi_L, \tag{2.19}$$

where ϕ_{3d} and ϕ_L are the 3d and ligand molecular orbitals, respectively. Knowing that the Kβ mainline features are governed by the 3p-3d exchange integrals, they too should be modulated by the metal-ligand covalency. Replacing the single molecular orbitals with the exchange 3p-3d integrals in the description they obtain:

$$\langle \psi_{3d}\psi_{3p}|\psi_{3d}\psi_{3p}\rangle \sim \alpha^2\langle \phi_{3d}\phi_{3p}|\phi_{3d}\phi_{3p}\rangle = \alpha^2(G^1_{pd} + G^3_{pd}), \tag{2.20}$$

where G^3_{pd} and G^1_{pd} are the Slater exchange integrals between 3p and 3d orbitals. The exchange integrals between ligand orbitals and 3p orbitals are much smaller and can be omitted. (2.20) shows how the exchange integrals can be affected by covalency also starting from a molecular orbital simple description including the metal-ligand covalency degree. The reduced exchange splitting with increasing covalency can be accounted in a reduced α factor in (2.20), which was implemented to successfully reproduce Kβ spectral features [41, 43].

2.3.2 Quantitative analysis

We have computed different parameters to perform a quantitative analysis of the Kβ spectra which are described in the following. Firstly, the integrated absolute difference (IAD) that was first proposed for XES by Vankó et al. [6] and results to be a successful approach to extract the spin evolution from the Kβ emission spectra. The IAD is defined as:

$$IAD_j = \int_{E_i}^{E_f} \left|SP_j - SP_{ref}\right| \, dE, \tag{2.21}$$

where SP_j and SP_{ref} are the spectrum j and a reference spectrum, respectively (both normalized to unity area). This method provides a way to obtain information from the whole spectra (the integral is calculated over the whole energy range recorded, from E_i to E_f), it needs only a simple preparation of the data and it can be performed without using results from theoretical calculations. For these reasons, IAD is a useful tool for the rapid determination of the spin state or its variation from Kβ XES spectra. The disadvantages could be that requires all the set of experimental data to be acquired under similar conditions and the sign of the change of the spin variation is lost. Since differences are compared, it is a relative method and a reference compound has to be choosen[9]. A linear dependence between IAD values and spin is found and a IAD-S calibration is possible if model compounds with well established spin values are measured (see Figure 2.6) which then allows to extrapolate the spin values of samples where the spin is unknown. This approach might seem arbitrary as a first look, but it has been demostrated, for example with spin state transitions [7], that is a true probe of the lineshape variation being very valuable because of its sensitivity to small changes in the spectra. Another parameter is the 1st moment of the K$\beta_{1,3}$ peak. The general definition of the 1st moment is given by:

$$\langle E\rangle \equiv \frac{\sum_j (E_j \cdot I_j)}{\sum_j (I_j)}, \tag{2.22}$$

[9] Usually a LS compound is chosen as reference.

with E_j and I_j being the energy and intensity of the data point j, respectively. Despite that the 1st moment analysis only takes into account the information coming from the main peak, it also shows a linear dependence with the nominal spin value (see Figure 2.6) and even though is less sensitive to weak variations than the IAD it is very useful because it preserves the sign of spectral changes. This type of analysis as an energy indicator has been preferred over the evaluation of the main peak energy, because the latter requires a non-trivial fitting of the Kβ mainlines due to their multiplet structure origin (see section 2.3). A fitting of the Kβ spectra with Voigt functions was reported [42] where however some external empirical constraints had to be applied.

Finally, another relevant parameter relative to the Kβ spectra is the center-of-gravity (COG), which mathematically is calculated in the same way as the 1st moment but using the whole spectrum. The COG determination is motivated by the suggestion made by P. Glatzel [12], [26] where it was proposed that in order to remove the variations due to screening effects all the spectra to be compared should be aligned to have equal COG. This should allow then to observe only the changes due to the 3p-3d exchange interaction variations in the spectra.

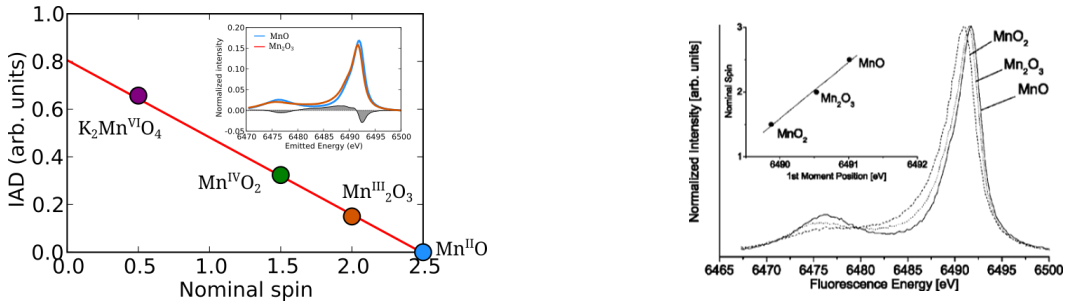

Figure 2.6: *Example of IAD analysis (left) and 1st moment analysis (right) in Mn oxides. Images are taken from ref. [27] and [12], respectively.*

2.4 Kα emission lines

We recall that these lines arise from the 2p to 1s transition and are split into a doublet by the spin-orbit interaction, resulting in the $K\alpha_1$ ($2p_{3/2}\rightarrow 1s$) and $K\alpha_2$ ($2p_{1/2}\rightarrow 1s$) lines. However, the 2p-3d exchange interaction is weaker than the spin-orbit interaction of the 2p level and is not enough to resolve splittings in the single $K\alpha_1$ and $K\alpha_2$ peaks, as occurs in the Kβ lines with the $K\beta_{1,3}$-Kβ' splitting. The spin-polarized nature here is hidden within the single peaks, leading a slight asymmetry [4, 45, 46]. Multiplet theory suggests a similar picture for the final configuration compared to the Kβ mainlines, with the difference that the exchange interaction results in splittings inside $K\alpha_1$ and $K\alpha_2$ features. This is only an approximation, because symmetry mixing are neglected. Different spectral parameters from the Kα spectra, like full-width at half-maximum (FWHM) and intensities of the peaks, can be simply analysed thanks to the easily fitting lineshapes and the higher count rates with respect to the Kβ lines. The exchange splitting can influence the shape of a single peak and arguments similar to the Kβ can be applied considering the exchange interaction between 3d and 2p ($2p_{3/2}$ for the $K\alpha_1$ peak) and the 3d electrons. However, this Coulomb exchange energy depends on the distance between interacting electrons (which influences the overlap exchange integral), which here is different because 2p electrons are considered instead of the 3d electrons. Still, it was reported a roughly linear relation between the FWHM of the more intense peak $K\alpha_1$ and nominal spin value given by the 3d electrons [6, 47–49].

CHAPTER 3

X-ray emission spectroscopy in synchrotron facilities

This chapter concerns the basic physical principles behind the generation of the synchrotron radiation, where we focus on the European Synchrotron (ESRF) and the high-brilliance x-ray spectroscopy beamline ID26, where our experiments was carried out.

3.1 Synchrotron facilities

Synchrotron radiation is the name given to the electromagnetic radiation when is generated by charged particles travelling at relativistic speed that are forced to curve their trajectory with an applied magnetic field. Since its first observation in 1947 at General Electric research group in New York, it was realized by the scientific community that it was an extremely powerful and versatile source of x-rays. After this discovery, the development of the 1st generation synchrotron radiation facilities began. The first synchrotron experiment was carried out in 1956 by Tomboulian and Hartman with a 320 MeV in Cornell University (Ithaca, United States). These first facilities were also called "parasitic", because the accelerators were built and usually operated primarily for high-energy or nuclear physics. A trend towards higher energy began and culminate with the DESY synchrotron in Hamburg (Germany), operating at 6 GeV and not only dedicated to high-energy physics but also to synchrotron radiation in 1964. High-energy physics required the storage rings to be operated to provide the highest possible collision rates without blowing up the beam and this generally meant low beam currents, a severely limited output of synchrotron radiation. The Synchrotron Radiation Source (SRS) at the Daresbury Laboratory (United Kingdom) was the first storage ring dedicated only to synchrotron radiation studies with a dedicated beamline from the 5 GeV electron accelerator. After the SRS, many facilities, called 2nd generation sources, like NSLS (Upton, United States), KEK (Tsukuba, Japan), BESSY (Berlin, Germany) and LURE

(Paris, France) began to appear. This history culminated with the current 3rd generation sources. Among them, the ESRF with a 6 GeV storage ring was the first to operate in 1994 followed by the APS (Argonne, United States) and SPring-8 (Hyogo prefecture, Japan). This 3rd generation sources are physically large (850 to 1440 m of circumference, see picture of ESRF in Figure 3.1) with a capability of 30 or more insertion devices and bending magnets as a source of synchrotron radiation. These facilities have many orders of magnitude higher brilliance and coherence with respect to the early lab sources and provide a highly collimated beam in a continuum spectral range, from infra-red ($\sim$ 1 eV) to hard x-rays ($\sim$ 100 keV).

Figure 3.1: *View of the European Synchrotron Radiation Facility. Figure taken from ref. [50].*

3.2 ESRF synchrotron

To explain the main features and components of a 3rd generation synchrotron we will focus on the ESRF as a representative example. The electrons are produced by an electron gun (a thermoionic electrostatic triode) and first accelerated by a DC electric field up to 90 keV and then up to 170 MeV by a linear accelerator (LINAC). After that they are injected in the 300 m long booster ring, where they are finally accelerated to reach the energy of 6 GeV. At this energy the electrons are ready to produce light and they enter in the storage ring, a 844 m-long circular tube, where they circulate at a frequency of 355 kHz. A schematic 3D representation of the ESRF is shown in Figure 3.2. To allow electrons to circulate the ring is kept in an ultra high vacuum (UHV) level (up to 10^{-11} mbar). This way they can have an average lifetime in the ring up to 60 h during which they can emit synchrotron radiation. The acceleration is done in these last stages by conductive metal structures (cavities) which reshape the modes of oscillation of the electromagnetic field to have a component parallel to the electrons motion. The radio frequency (RF) system sets the oscillation frequency of the cavities, which has to be chosen carefully to avoid electron deceleration. RF electric fields are set at 3 GHz (35 MW power) for the booster ring and at 352 MHz (9 MW power) for the storage ring. The RF also determines the *filling mode* of the ring. The storage ring is never completely filled, but the electrons are grouped in

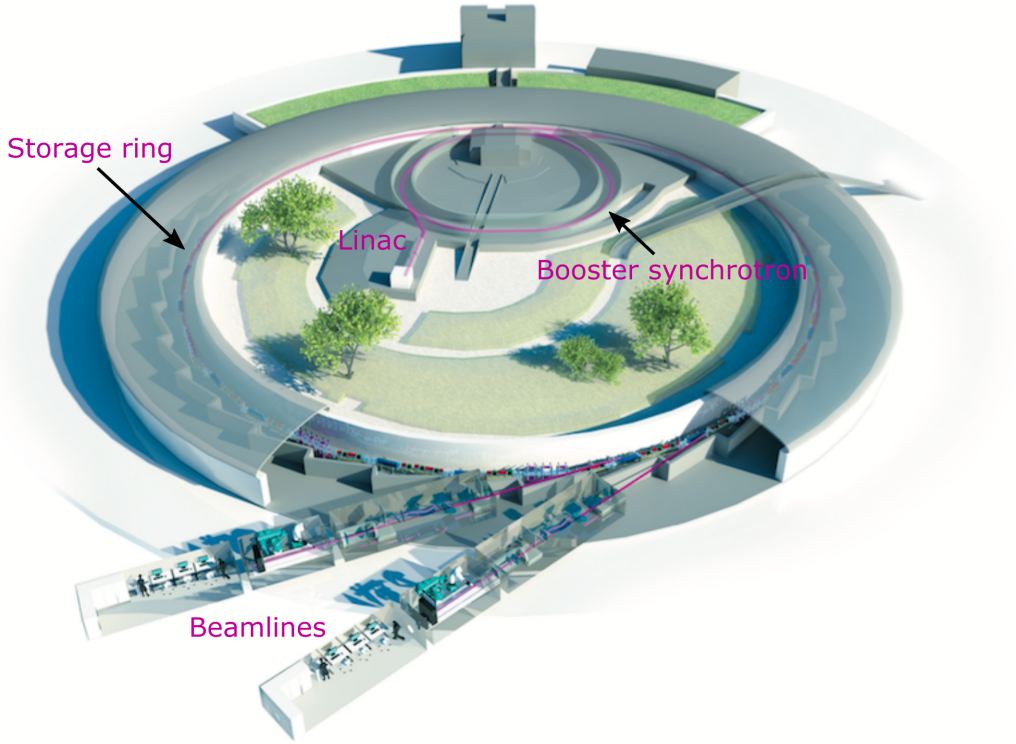

Figure 3.2: *Schematic 3D representation of the ESRF. Figure taken from ref. [50].*

packages, called *bunches*, which may contain a different number of them depending on the filling mode. The maximum number of bunches in the ring is given by the length of the ring divided by the RF frequency, and is achieved with the uniform filling mode. The other modes of operation use less bunches but have higher current for each bunch, resulting in an increased power of each bunch. The electrons are forced to circulate in the ring by magnetic forces provided by a complex magnetic lattice all around the storage ring. Inside it different types of magnet are present: among them there are the quadrupole and sextupole magnets which are usually placed in the straight sections of the ring. The firsts are used to focus the beam and keep it to maintain the circular trajectory. The second are used to correct the chromatic aberrations due to the failure of focus the electrons with slightly different energies in the same way.

Then, along the storage ring, the electrons provide the radiation to the different beamlines when their trajectory is curved. There are two different types of synchrotron radiation sources: *bending magnets* (BMs) and *insertion devices* (IDs). BMs are placed to close the path of the electrons after the straight sections. However, as the electrons are deflected from their straight path when passing through these magnets, they emit x-rays tangentially to the plane of the electron beam (Figure 3.3). The synchrotron light from a BM covers a wide and continuous spectrum. The IDs are placed in the straight sections between BMs. The IDs consist in an array of N alternating poles magnets of length $L = N\lambda_u$ (λ_u is the spatial period) producing a field that alternates from up to down (Figure 3.4). As the electrons pass through, they are forced to oscillate in the horizontal plane. An important parameter to describe the electron motion inside

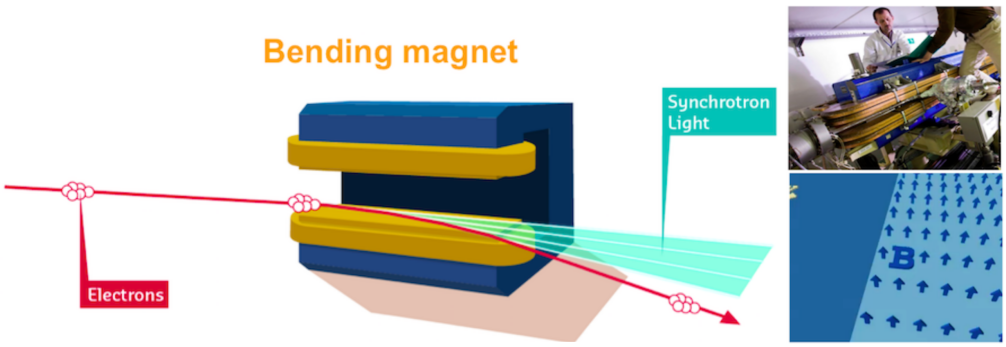

Figure 3.3: *Bending magnet at the ESRF. Figure taken from ref. [50].*

an ID is the deflection parameter K, given by:

$$K = \frac{eB_0\lambda_u}{2\pi mc} = 0.934\lambda_u[\text{cm}]B_0[\text{T}] \tag{3.1}$$

The angular deflection in terms of K is $\theta_{max} \sim K/\lambda$. We can have two types of ID depending on the K parameter: if $K \gg 20$ we have a *wiggler*, if $K \ll 1$ we have an *undulator*. In an undulator the radiation emitted is compressed by a factor of $1/\sqrt{N}$ with respect to the natural opening angle of a SR radiation $1/\lambda$. For an undulator we have that a given electron at one oscillation is in phase with the radiation of the following oscillations, because the angular deflection is lies within the nominal $1/\lambda$ emitted radiation cone of the SR [51]. The resulting radiation results in the so-called undulator equation:

$$\lambda[\text{nm}] = \frac{1.306\lambda_u[\text{cm}](1 + \frac{K^2}{2} + \gamma^2\theta^2)}{E_e^2[\text{GeV}]} \tag{3.2}$$

where E_e is the electron energy, $\gamma^2\theta^2$ are the off-axis wavelength variations. In addition to the fundamental wavelength, the effect of transverse oscillations introduces higher harmonics in the radiation. The even harmonics radiate off-axis, and they have less intensity than the in-axis odd harmonics. One should note that in the (3.2) the K parameter appears. This means that the the fundamental wavelength can be shifted varying the magnetic field (by changing the gap between between magnetic poles) of the undulator. To summarize, the important characteristics of the undulator radiation are:

- The high flux of x-rays coming out (due to the in-phase oscillation mentioned before) resulting in an intrinsic high brilliance (only affected by the source area and the angular divergence).
- Intrinsic angular divergence of the x-ray beam, smaller compared to the BMs.
- A fully tunable source of x-rays over an extended spectral range, concentrated into the odd harmonics (1st or fundamental, 3rd harmonic, 5th harmonic...)
- Linear polarization of the radiation.

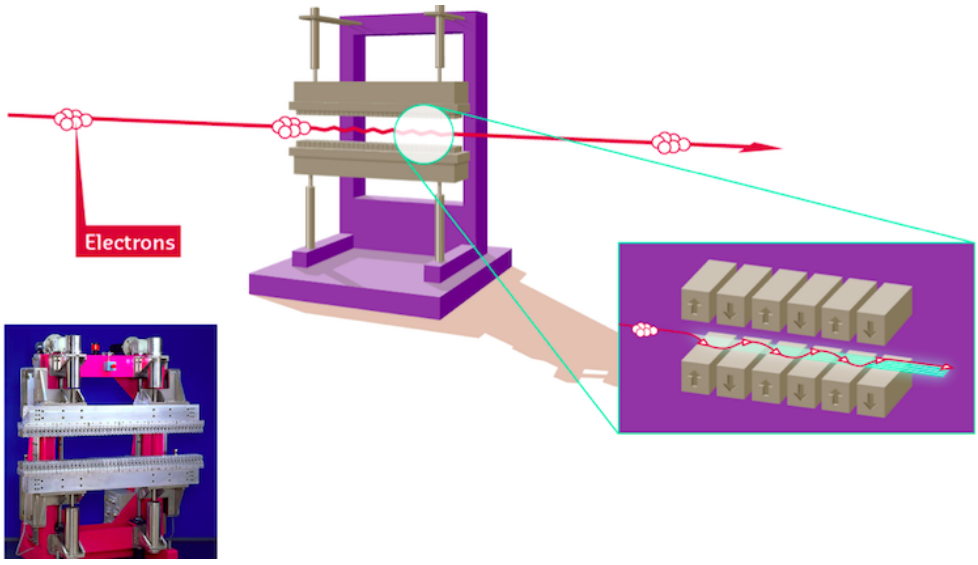

Figure 3.4: *Insertion device at the ESRF. Figure taken from ref. [50].*

3.3 ID26 beamline

3.3.1 Beamline layout and key components

In the following the layout and the key components as well as the x-ray emission spectrometer, the main feature of ID26 beamline, will be described. All the x-ray emission measurements presented in this work have been carried out at ID26. This beamline is fully dedicated to x-ray spectroscopy, both in absorption and emission. For the absorption is it possible to perform X-ray Absorption Fine Structure (EXAFS) and X-ray Absorption Near Edge Structure (XANES). For emission it is possible to perform X-ray Emission Spectroscopy (XES) and Resonant Inelastic X-ray Scattering (RIXS).

ID26 is an insertion device beamline, composed of three mechanically independent undulators providing a beam with very high photon flux and high brilliance, allowing measurements on very diluted samples. The minimum energy of the fundamental undulator harmonics at ID26 is 2.4 keV and define the lowest achievable energy for the experimental measurements. Higher energies can be reached with higher harmonics, going up to 27 keV. A schematic layout of ID26 is shown in Figure 3.5. The first component after the undulators is a set of vertical and horizontal slits used to define the undulator emission axes (primary slit) and to reduce the power of the white beam (secondary slit) received by the Horizontal Deflecting Mirror (HDM1). HDM1 is a water-cooled 620 mm long flat mirror used to deflect away the white beam coming from the undulators from the storage ring emission radiation and protecting all the following optical components from the heat load. To select the required wavelength a cryogenically-cooled double-crystal monochromator is used. ID26 features by two sets of crystals: Si[111] and Si[311] pairs. The intrinsic resolutions (dE/E) of the crystals are 1.4×10^{-4} with the Si[111] and 0.3×10^{-4} with the Si[311]. Beam focusing is achieved independently in horizontal and vertical with two elliptical shaped mirrors (HFM2, VFM2) in a Kirkpatrick-Baez configuration. A typical spot size of 500 µm (horizontal) × 100 µm

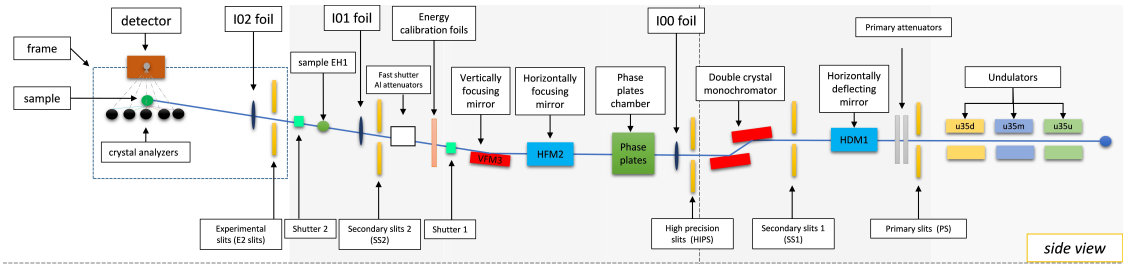

Figure 3.5: *ID26 detailed scheme. The x-ray beam is coming from right side. Source: wiki of ID26.*

(vertical) is achieved by bending the mirrors with high voltages. Each mirror of the beamline has three different coatings (Pt, Si and Pd) for efficient harmonics rejection. The incident energy calibration is performed using thin metallic foils stored along the beampath by measuring the absorption spectrum in transmission. The incoming flux of photons is monitored in various positions along the beamline (I00, I01, I02) through the scattering of Kapton foils (I00, I01 and I02 foils). Finally a fast shutter, Al attenuators and other slits just before the sample (E2 slit) are placed to regulate the incoming power. ID26 has two experimental hutches, EH1 and EH2. Most of the experiments are carried out in the latter where it is located the x-ray emission spectrometer.

3.3.2 The x-ray emission spectrometer

The ID26 x-ray spectrometer is a point-to-point scanning instrument working in vertical Rowland geometry. In this configuration a bent Bragg crystal is arranged with the sample and the detector in a circle, known as the Rowland circle. The well-known physical principle behind the spectrometer is x-ray diffraction. Once x-rays have been scattered by the sample the wavelength λ of the reflected radiation is selected by the crystals through the Bragg's law [52]:

$$2d \sin\theta_B = n\lambda, \tag{3.3}$$

where θ_B is the Bragg angle and n is an integer number. The lattice spacing is $d = a/\sqrt{(h^2+k^2+l^2)}$ where a is the lattice parameter and h, k, l are the Miller indices. λ is the x-ray wavelength. (3.3) connects each Bragg angle to a specific incident energy, through:

$$\theta_B = \arcsin\left(\frac{hc}{2dE_i}\right) \tag{3.4}$$

Bragg's law assumes a unity index of refraction an thus is only an approximation. A more accurate treatment can be made with the dynamical diffraction theory, which gives an intrinsic width $\Delta\theta_B$ (called Darwin width) for each Bragg angle [53]. The Rowland geometry ensures that the Bragg angle remains the same from any point on the circle. Therefore changing the energy is simply done by changing the angle formed by the normal to the crystal surface and the sample. There are two types of analytical geometry currently in use for the crystal analysers. The first type, the Johann geometry, is constructed by bending the crystal to a radius of 2R, where R is the radius of the

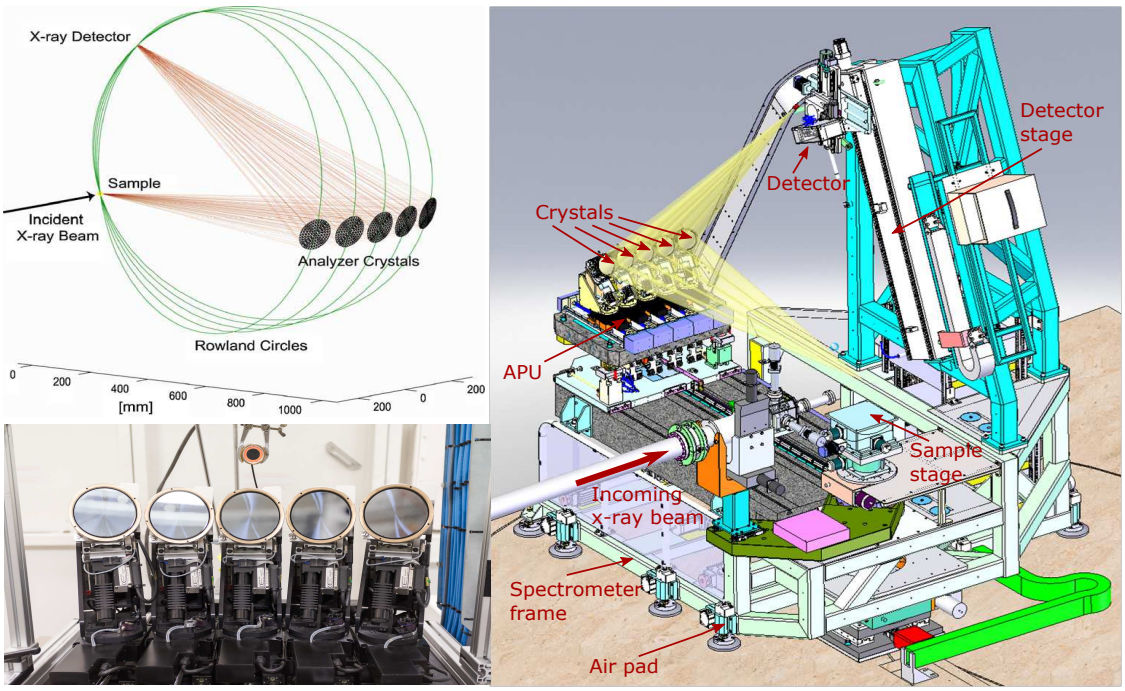

Figure 3.6: *Left: sketch of a multiple crystal Rowland geometry (taken from ref. [54]) and a detail on the Bragg crystals mounted on the APU. Right: scheme of the high resolution spectrometer at ID26 with some main components. Image taken from ref. [55].*

Rowland circle. The bending is done in such a way the crystal planes are parallel to the crystal surface (see Figure 3.7). The mismatch between the latter and the Rowland circle trace (in fact, only the central point of the crystal is one the exact Rowland circle position) leads to the Johann aberration. The aberrations become negligible as long as the crystal's surface is not very extended and the Bragg angle approaches the backscattering geometry (that is θ_B=90°). Moreover the fact that the crystal is bent combines the increase the effective crystal area that fulfils the same diffraction condition and a re-focalizing effect typical of curved mirrors. The second type is the Johansson geometry, which is a better implementation of the Johann geometry. It was proposed in 1933 by Johansson and consists in a crystal bent to a radius 2R and then ground to radius R, so the Bragg planes are no longer parallel to the crystal's surface and the entire analyser's surface is now on the exact Rowland circle trace (see Figure 3.7). In this way the gradual variation of the incident angles across the crystal of a Johann-type spectrometer is solved and the collection efficiency together with the final energy broadening are optimized. In the ID26 setup a set of five spherically bent analyser crystals (in Johann geometry) on overlapping Rowland circles are used to improve the efficiency and capturing angle. Figure 3.6 shows a sketch of this multiple crystal geometry and also a scheme of the spectrometer. The sample, the analysers crystal and the detector specifications allows large movements: the scattering angle can be varied from 0° to 180° while the Bragg angle from 65° to 90°. The core component of the spectrometer is the analyser position unit (APU), consisting of five motorized modules allowing a four axes rotation which enable the position of each crystal with exact Rowland tracking. To achieve the required high stability all the spectrometer frame is supported by 12 airpads on a polished marble floor.

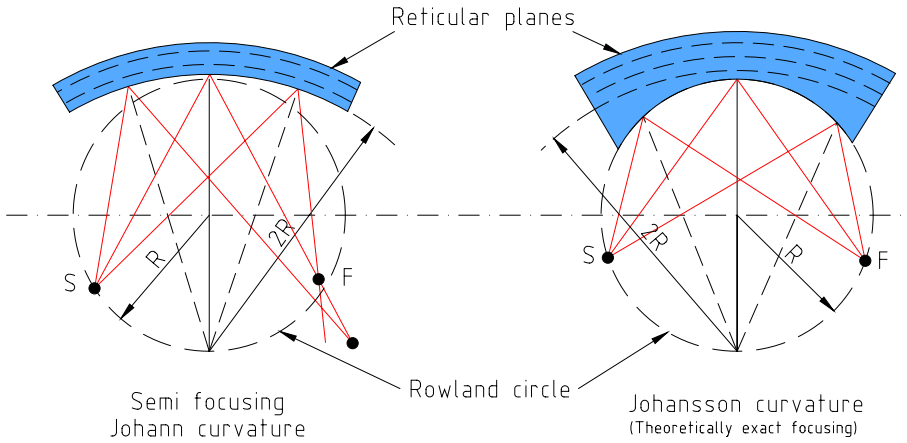

Figure 3.7: *Johann (left) and Johansson (right) geometries for the Rowland circle. Figure taken from ref. [18].*

Special foot holders for them were developed to provide the right support during the moving and to increase stiffness [55]. The x-ray spectrometer can be then used to perform x-ray emission spectroscopy (XES) both resonant (incident energy close to the absorption edge) and non-resonant (incident energy about 100 eV above the absorption edge) by scanning the emitted fluorescence photon energy. This is done by scanning the crystals Bragg's angle and the detector over the Rowland circle. We note that XES also includes resonant inelastic x-ray scattering (RIXS) and the so-called absorption spectroscopy (XAS). Since we are not using either of these two techniques in our study, the interested reader can refer to ref. [12, 56] for more informations.

CHAPTER 4

Experimental results

4.1 Experiment details

4.1.1 Beamline details

Concerning the beamline configuration, the Fe Kβ (and Kα) emission measurements were performed using using the undulator fundamental monochromatized by a pair of Si crystals in <111> reflection (<311> reflection for the Kα). Rejection of higher harmonics was achieved by three Si mirrors working under total reflection (2.5 mrad). The incident beam energy calibration was performed using a reference metallic Fe foil by setting the first inflection point of the Fe K edge at 7112 eV. Five spherically bent (R=1 m) Ge crystal analysers in <620> reflection were chosen suitable for the detection of the Kβ emission line of Fe. For the Kα detection four Ge crystal analysers in <440> reflection were used. The total resolution of the setup, determined as full width at half maximum of the elastic profiles, was $\sim$ 1.4 eV and $\sim$ 0.7 eV for the Kβ and Kα, respectively. All the measurements were performed at room temperature (RT). Sample, analyser crystal and an avalance photo diode (APD) were arranged in a vertical Rowland geometry to ensure the focus of the x-ray beam on the sample during the experiment.

4.1.2 Sample details

Most of the samples were provided by J. Blasco from the ICMA institute of the University of Zaragoza (Spain). D. Baster from the AGH University in Kracow (Poland) was provided us $LiFePO_4$, $Sr_2Fe_{1.5}W_{0.5}O_6$, $NaFeO_2$ and $Na_{0.7}Mn_{0.5}Fe_{0.5}O_2$. We purchased from Sigma Aldrich FeS, FeS_2, FeF_2, FeF_3, $K_4Fe(CN)_6 \cdot 3\,H_2O$, $K_3Fe(CN)_6$, $Fe_4[Fe(CN)_6]_3$. All the samples were checked by the providers by x-ray diffraction to ensure their good state. We were unable to do

diffraction experiments on the commercial samples. For them a comparison of XAS, XES spectra with the literature has been performed to check the good quality. All the sample used together with the different sample providers are displayed in Table 4.1. The solid samples were all in a polycrystalline form, thus the crystal field effects are averaged over the all crystallographic directions[1]. We additionally prepared two Fe liquid solutions with the following recipes: a 0.1 M Fe^{2+} solution was obtained by dissolving 1.39 g of $FeSO_4 \cdot 7\,H_2O$ solid salt with 50 mL of distilled water. A 0.1 M Fe^{3+} solution was prepared with the same method, by dissolving 2.02 g of $Fe(NO_3)_3 \cdot 9\,H_2O$ solid salt with 50 mL of distilled water. For the latter, to prevent Fe reduction, N_2 was bubbled during the preparation. Both solution have been homogenized with a magnetic stirrer. The resulting pH of the solutions was ~ 1. No evidences of radiation damage were observed in any of the samples except for the cyanides ($K_4Fe(CN)_6 \cdot 3\,H_2O$, $K_3Fe(CN)_6$, $Fe_4[Fe(CN)_6]_3$) and Fe water solutions. In order to obtain a reliable spectra without damage effects, we performed also HERFD scans in different spots with and without Al attenuators to determine the maximum exposure time which then was taken into account in the XES spectra.

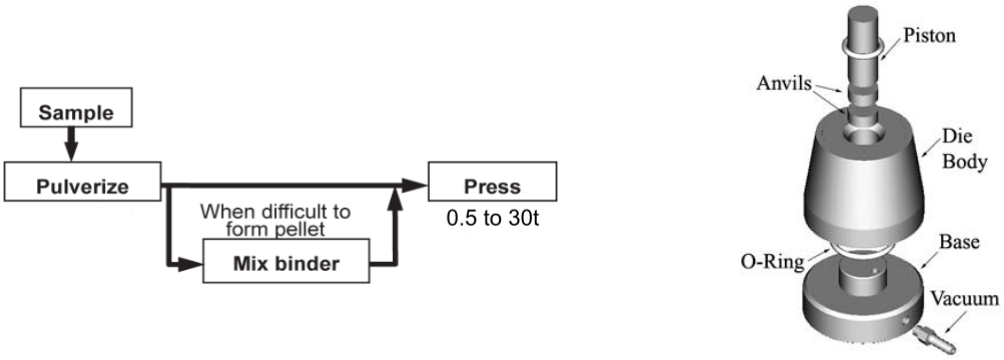

Figure 4.1: *Process for making pellets (left) and a scheme of a commercial die (right). The pressure is applied from the top of the piston.*

All the solid samples (unless otherwise stated) were prepared in the form of pellets with an high concentration (90% wt) in order to improve the countrates. Figure 4.1 shows the procedure of making pellets together with a sketch of the die used to press them. We used cellulose as a binder to ensure a good stiffness of the pellet. The pressure applied was less than 1 t because of the small size of the prepared pellets (5 mm). We used a different method of preparation for those samples that are air sensitive (FeS, FeS_2, FeF_2, FeF_3) using a controlled atmosphere. They were prepared in a gloovebag in a Nitrogen atmosphere by filling with the powder glass capillaries of 1 mm diameter. After that they were sealed with wax.

We used a liquid jet set-up to measure the Fe water solutions, showed in Figure 4.5a. 50 mL of aqueous solution were placed in a open beaker (used as a reservoir) and are sucked by a centrifugal pump, which keep a continuous flow. The cross section of the jet is determined by the nozzle's dimensions (a conventional glass capillary of diameter = 1 mm). The incident x-ray beam interacts with the solutions in the free fall region (just after the nozzle).

[1]Energy shifts in Kβ spectra have been found recording the K-emission lines at different angles in single crystal samples [57].

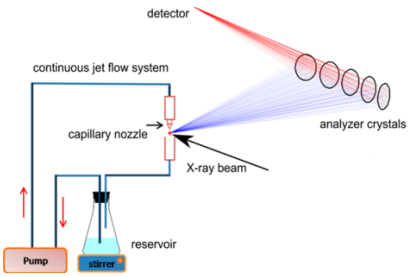

Figure 4.2: *Liquid-jet setup scheme. Figure taken from ref. [58].*

Table 4.1: *Compound chemical formulas, Fe formal valence, nominal spin value. Last column indicate the sample providers: SA = Sigma Aldrich, JB = J. Blasco (Zaragoza, Spain), DB = D. Baster (Kracow, Poland), C = ID26 chemical laboratory.*

Compound	**Formal valence**	**Nominal Spin**	**Provider**
Fe	0	1	C
FeS_2	+2	0	SA
$K_4Fe(CN)_6 \cdot 3H_2O$	+2	0	SA
FeS	+2	2	SA
FeF_2	+2	2	SA
FeO	+2	2	C
$FeTiO_3$	+2	2	C
$BaFe_2As_2$	+2	2	JB
Fe^{2+} water solution	+2	2	C
$Fe_4[Fe(CN)_6]_3$	+2.57	1.43	SA
$LiFePO_4$	+2.2	2.1	DB
Co_2FeO_4	+2.4	2.2	JB
$YbFe_2O_4$	+2.5	2.25	JB
YFe_2O_4	+2.5	2.25	JB
$LuFe_2O_4$	+2.5	2.25	JB
$CrFe_2O_4$	+2.5	2.25	JB
$Sr_2Fe_{1.5}W_{0.5}O_6$	+2.5	2.25	DB
Fe_3O_4	+2.67	2.3	JB
Ba_2FeReO_6	+2.75	2.35	JB
Sr_2FeReO_6	+2.7	2.33	JB
$K_3Fe(CN)_6$	+3	0.5	SA
$NaFeO_2$	+3	2.5	DB
$LuFeCoO_4$	+3	2.5	JB
α-Fe_2O_3	+3	2.5	JB
γ-Fe_2O_3	+3	2.5	C
Ca_2FeReO_6	+3	2.5	JB
$SmFeO_3$	+3	2.5	JB
$LaFeO_3$	+3	2.5	JB
$MnFe_2O_4$	+3	2.5	JB
$LaFe_{0.5}Ga_{0.5}O_3$	+3	2.5	JB
$Na_{0.7}Mn_{0.5}Fe_{0.5}O_2$	+3	2.5	DB
FeF_3	+3	2.5	SA
Fe^{3+} water solution	+3	2.5	C
$La_{0.33}Sr_{0.67}FeO_3$	+3.65	2.18	JB
$Pr_{0.33}Sr_{0.67}FeO_3$	+3.65	2.18	JB
$SrFeO_3$	+4	2	JB

4.2 Data treatment

4.2.1 Fe Kβ XES data

First of all a normalization to unit area in the range 7020-7085 eV has been done for all the Kβ spectra to allow the comparisons. Both of the data reduction techniques discussed in the previous chapter (IAD and 1st moments) have been used to treat the Kβ data. The IADs have been computed using the whole energy range recorded, from 7020 to 7085 eV (Figure 4.3). The compound chosen as a reference (with resulting zero IAD value) was FeS_2. The errors have been evaluated taking the difference signal between two consecutive equivalent spectra and integrating over the whole energy range. They are not displayed because they result to be, on average, less than 10% of the IAD values themselves. For the 1st moments an energy range from 7053 to 7065 eV was used to include all the shape of the $K\beta_{1,3}$ line. The 1st moments can be calculated choosing the energies at 100 % of the peak, but also different choices can be made, taking the energies at less % of the peak [33]. We have computed them also including 80 % and 50 % of the peak and the values seems to spread more within the same nominal spin value. For this reason we finally chose the energies for the 100 % of the peak aiming to extract as more information as possible. The center-of-gravities (COGs) have been computed in the same way of the 1st moments, but using the whole spectral range (7020-7085 eV).

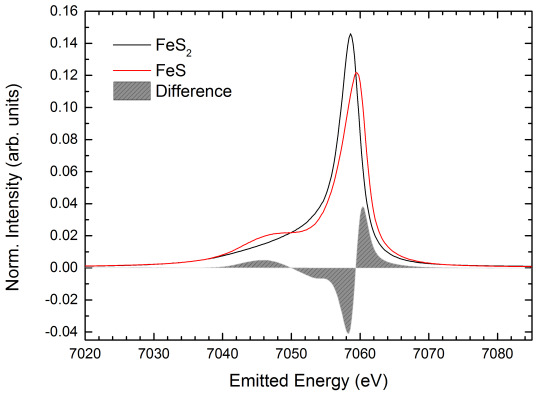

Figure 4.3: *Example of a difference spectrum. IAD is computed as the integral of the absolute value of the dashed area.*

4.2.2 Fe Kα XES data

The normalization to unit area has been done also for all the Kα spectra with the range 6385-6410 eV. To extract information from the Kα we performed a Lorentzian fitting of the two peaks (based on [59]), which works well for evaluating the FWHMs and intensities (Figure 4.4). The peak energy position is slightly understimated and has not been used in our analysis. The errors on the FWHMs coming from the fitting are, on average, less than 4 % and are not displayed. To check if the values obtained are consistent, we extract the values of the FWHMs with a spline

of ΔE_s=2.5 meV in order to have 10^4 data points. The total number of data points is given by the full energy range collected $\Delta E_{full} = 6410 - 6385$ =25 eV divided by a step size of 0.2 eV, giving 125 data points each Kα spectrum. To have 10^4 data points the spline has to be 2.5 meV. The FWHMs obtained with this method differ less than 10 % from the Lorentzian fit.

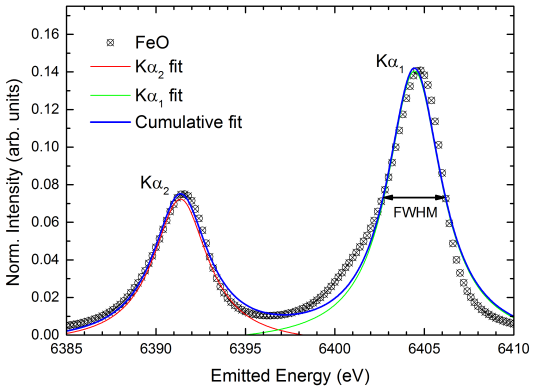

Figure 4.4: *Example of Ka spectra with fitted with two Lorentzian functions, one for each peak.*

4.3 Results

4.3.1 Fe Kβ XES

The data will be presented as follows: first we compare the compounds with the same formal valence, divided into high-spin (HS) and low-spin (LS). Then we will discuss how the different degree of covalency influences the spectra. Also we will examine the more metallic compounds separately and compare them to the results in pure Fe metal to evaluate how the metallic/insulating character affects the spectral features. Besides we will pay attention to the effect of the Fe environment symmetry in the spectra. Finally we will show the results of the IAD analysis and 1st moment positions of the $K\beta_{1,3}$ peak for all the compounds as a function of the nominal spin value of the Fe 3d shell.

Figure 4.5a and 4.5b show the spectra of the Fe^{3+} HS and LS compounds, respectively. All spectra of HS ferric compounds are characterized by a $K\beta_{1,3}$ 1st moment of ∼ 7059 eV (Table 4.3) and a pronounced Kβ' feature at ∼ 7045 eV. The same comparison among the Fe(II) compounds has been done. The spectra of ferrous HS compounds (Figure 4.6a) have a $K\beta_{1,3}$ 1st moment of ∼ 7058 eV reflecting the decrease of the spin state. We note that the Fe^{3+} HS has nominal spin S=2.5 while Fe^{2+} HS has nominal spin S=2. We know that generally the Kβ lines are said to be much more sensitive to the metal spin state than the Kα ones, especially in the Kβ' satellite [39], [18]. Here the spin-up character is almost pure or dominant and makes possible a spin state "labelling": the exchange interaction between the 3p and the 3d electrons of the metal is dramatically reduced due to the weak 3d spin moment in the LS compounds. This results in a reduced energy splitting between the satellite Kβ' and the main peak. We clearly see this effect when looking at the LS ferric compounds, where the Kβ' feature pratically disappears because is "incorporated" into the

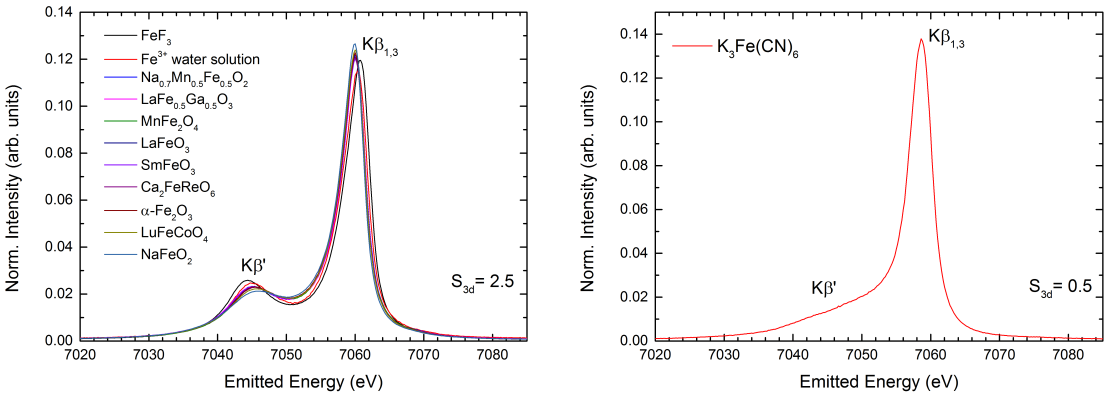

(a) *HS Fe(III) compounds* (b) *LS Fe(III) compound*

Figure 4.5: *Fe Kβ spectra of the Fe(III) compounds. The spectra have been normalized to unit area in the range 7020-7085* eV*. The spectral shape of FeF_3 is in agreement with [43].*

main peak. In general a shift towards low energies with decreasing spin state is detected in the $K\beta_{1,3}$ 1st moment when keeping the same oxidation state. In particular we detect a shift of ~ 1 eV between HS and LS compounds, both ferric and ferrous samples, according to the same nominal 3d spin moment variation ΔS_{3d}=2 for both oxidation states going from HS to LS compounds (Fe^{3+} LS has nominal spin S=0.5 while Fe^{2+} LS has nominal spin S=0). Additionally, if we look more carefully at the spectra of Figure 4.5a and 4.5b, we note a slightly different Kβ' shoulder for the two sulfides with respect to the other compounds. This can be an index of a more metallic character of these compounds and will be analysed later.

Looking at the spectra in Figures 4.5a and at the 1st moments of the $K\beta_{1,3}$ peak (Table 4.3), it is remarkable that FeF_3 shows a shift towards high energies of ~ 0.5 eV, despite that the formal oxidation and spin state is the same as in the other compounds. This effect was also reported by Pollock et al. [43] between FeF_3 and other Fe^{3+} HS compounds like $FeCl_3$ or $FeBr_3$ and was assigned to the differences in covalency. We will analyse later more in details the covalency effects, together with other two effects that we have found modify the Kβ spectral shape: the metallicity and the local symmetry.

In Figure 4.7a we report the spectra of all mixed valence HS compounds. All the spectra are very similar among them with the same features discussed previously. The similarities between the spectra can be expected as there are no significant spin variations among the compounds (see table Table 4.3) because they differ only in a small fractions of the Fe^{3+}/Fe^{2+} states. Figure 4.7b shows the spectra of $Fe_4[Fe(CN)_6]_3$ (Prussian Blue), which in addition has a mixed spin character [60]. Its spectral shape is in agreement with [60].

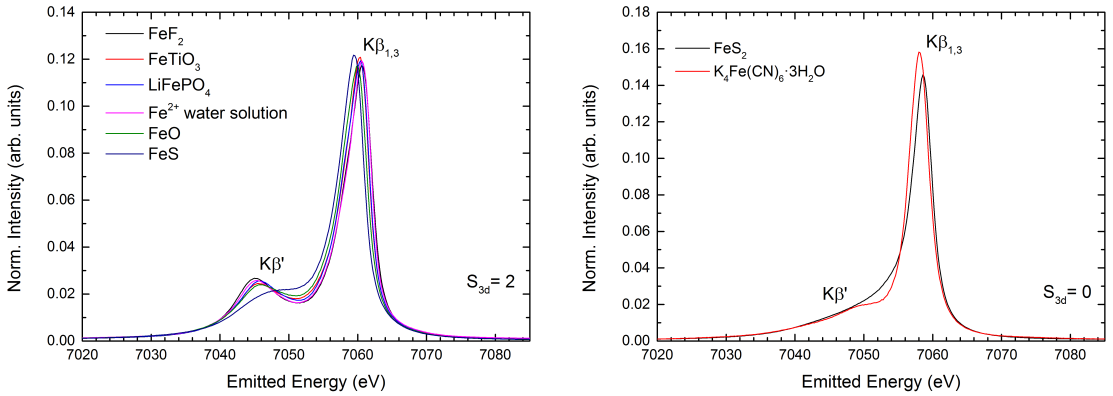

(a) *HS Fe(II) compounds* (b) *LS Fe(II) compounds*

Figure 4.6: *Fe Kβ spectra of the Fe(II) compounds. The spectra have been normalized to unit area in the range 7020-7085* eV.

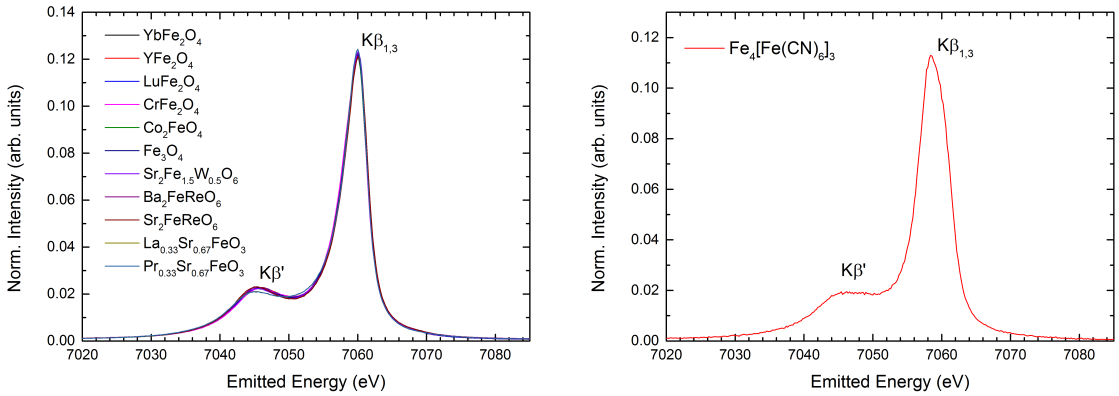

(a) *HS Fe mixed-valence compounds* (b) *HS-LS Fe mixed-valence compound*

Figure 4.7: *Fe Kβ spectra of the mixed Fe valence compounds. The spectra have been normalized to unit area in the range 7020-7085* eV

.

Covalency Different degree of covalency means a different value of the charge transfer energy (CT) parameter Δ, which is defined as energy required by an electron to hop from the ligand to the Fe ion [12]. The covalency of a compound is also determied by the ligand electronegativity, the chemical property that describes the tendency of an atom to attract electron density towards itself. In Figure 4.8 we have selected some Fe^{2+} compounds for which we could find electronegativity values and we have plotted the 1st moment of the $K\beta_{1,3}$ peak as a function of this parameter to see if there is any correlation. Going from the more covalent character of the sulfide to the more ionic character of the fluoride the electronegativity of the ligand increases resulting in an increase of the $K\beta_{1,3}$ 1st moment, which reach the higher value for the more ionic FeF_2. Bocquet et al. [61] show that, for a given cation, changing the ligand results in a change of Δ: from the less

electronegative S^- to the highly electronegative O^{2-}, the charge transfer energy increases. This is because the more electronegative is the ligand, the more its bands are lowered with respect to the metal 3d bands and more difficult is for an electron to hop to the metal ion. A similar peak shift with increasing ionic character was also found by Tyson et al. [41] for Mn compounds. The reduced Kβ' shoulder is a consequence of the reduced splitting between the two lines: for more covalent compounds it starts to be more incorporated into the $K\beta_{1,3}$ main peak [42].

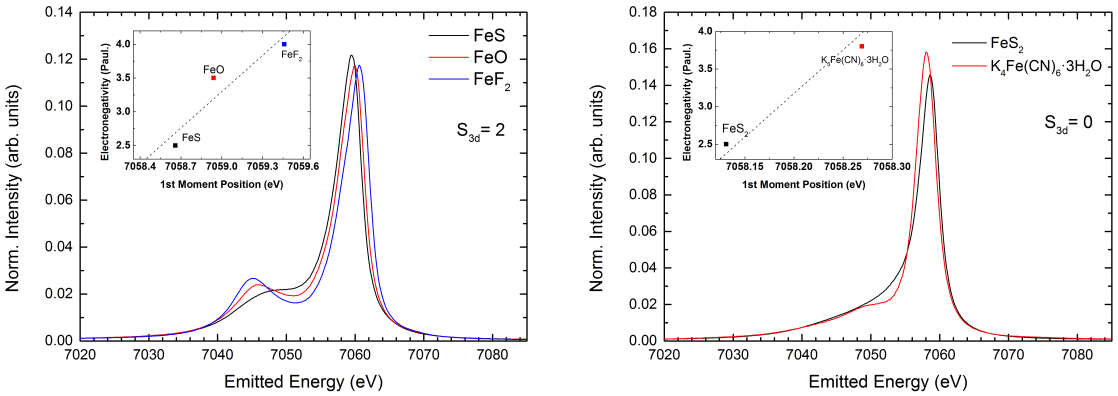

(a) *HS Fe(II) selected compounds*

(b) *LS Fe(II) selected compounds*

Figure 4.8: *Fe Kβ spectra of ferrous compounds with different ligands, divided into HS and LS to avoid the effect of the different spin states. The spectra have been normalized to unity in the range 7020-7085* eV*. Inset shows ligand electronegativity vs. 1st moment plot. The electronegativity values are taken from ref. [62]. Dashed line are guidelines for the eyes.*

In Figure 4.9 we show the spectra of the compounds with the same ligands. There is a total of 4 families: cyanides, sulfides, fluorides and oxides. In this comparison the differences due to large ligand electronegativity variations should be almost eliminated. For this reason we try to relate the shift in the $K\beta_{1,3}$ 1st moment (which is related to the splitting $\Delta E_{K\beta_{1,3}-K\beta'}$) to the nominal spin variation ΔS_{3d}. For the cyanides (Figure 4.9a) the shift from the ferrous LS $K_4Fe(CN)_6 \cdot 3\,H_2O$ to the mixed spin $Fe_4[Fe(CN)_6]_3$ is $\sim$ 0.4 eV for a total ΔS_{3d}=1.4. The ferric LS $K_3Fe(CN)_6$ results to have an intermediate $K\beta_{1,3}$ 1st moment because of its intermediate spin value between the two others. If we now look at the sulfides in Figure 4.9b, the shift results to be $\sim$ 0.5 eV. This larger value is due to the different spin state of the two sulfides (Fe(II)S is HS and Fe(II)S_2 is LS) which results in a ΔS_{3d}=2. Finally, we noticed that in compounds with the same spin state (as the fluorides in Figure 4.9c) the $K\beta_{1,3}$ 1st moment shift is less pronounced: between Fe(III)F_3 and Fe(II)F_2 (both HS compounds) is $\sim$ 0.12 eV, which is related to ΔS_{3d}=0.5. The same is true for the oxides: the shift of the $K\beta_{1,3}$ 1st moment from Fe(II)O to α-$Fe(III)_2O_3$ is $\sim$ 0.13 eV, also related to the same ΔS_{3d}=0.5. In this comparison we can conclude that a 1st moment linear dependence to the spin value is achieved among the compounds with the same ligands.

Metallicity In Figure 4.10 Fe Kβ spectra of the compounds with more metallic behaviour are showed. Based on the spectral shape of the pure Fe metal, characterized by a very smooth Kβ' shoulder, we have included compounds showing a similar lineshape: FeS, FeS_2, $BaFe_2As_2$. We

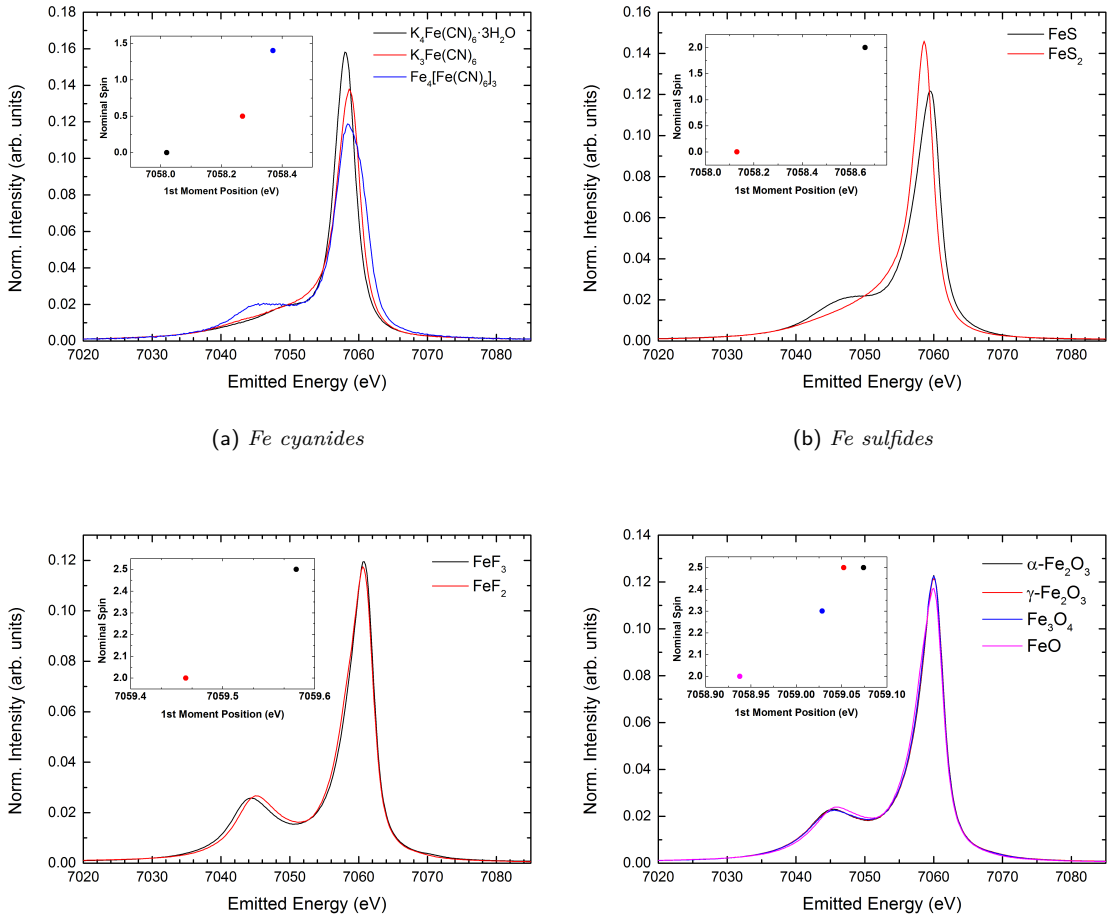

(a) *Fe cyanides* (b) *Fe sulfides*

(c) *Fe fluorides* (d) *Fe oxides*

Figure 4.9: *Fe Kβ spectra of the compounds belonging to different families, with the same ligands. The spectra have been normalized to unit area in the range 7020-7085* eV*. The spectral shapes of the sulfides are in agreement with [63]. Insets: nominal spin vs 1st moment position plot.*

have also added the spectra of the double perovskites Ba_2FeReO_6 and Sr_2FeReO_6 which undergo a metal to insulator transition at low T and should be metallic at room temperature [65]. The resistivity values at RT for these compounds are showed in Table 4.2. If we compare the resistivity of metal Fe, $BaFe_2As_2$ and FeS_2 with the resistivity of the two perovskites, we notice that the former values are lower, which seems correlated to the presence of a sharper Kβ' feature in the latter samples. An intermediate resistivity value is found for FeS, along with the presence of a slightly more pronounced Kβ' feature compared to the lower resistivity samples. Apart form the intensity evolution of the Kβ' feature, we have plotted the resistivity values versus the 1st moment position of the $K\beta_{1,3}$ peak to check whether there is a correlation (see inset of Figure 4.10). Qualitatively, a trend can be observed of increasing the 1st moment position with increasing resistivity. Remarkably, Fe metal falls off this trend. From this comparison we can conclude that: the double perovskites, which exhibit an higher energy main peak and a more pronounced Kβ' feature, have a relatively poor metallic character. The $K\beta_{1,3}$ 1st moment position and the shoulder

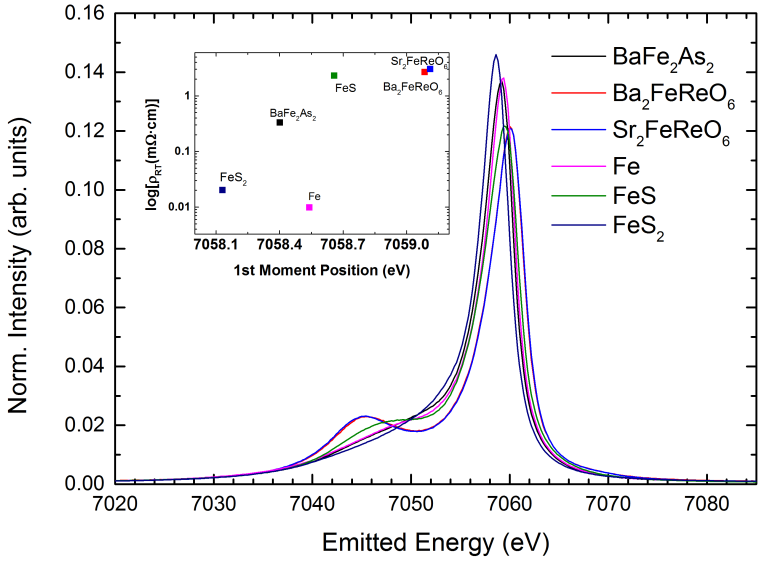

Figure 4.10: *Fe Kβ spectra of metallic compounds. The spectra have been normalized to unit area in the range 7025-7080* eV*. The spectrum of pure Fe metal agrees with previously reported one [64]. Inset: the resistivity values at RT (ρ_{RT}) showed in a log scale as a function of the Kβ$_{1,3}$ 1st moment position.*

intensity for FeS agree with the intermediate resistivity value. For the FeS_2 and $BaFe_2As_2$, which have the lower resistivity values, the shoulder and the Kβ$_{1,3}$ 1st moment position are comparable to the pure Fe. The metallic character can be viewed as an "extreme covalency" situation: the high delocalization of the valence electrons results in a reduced 3d-3p exchange interaction [66]. Therefore, in metallic compounds the Kβ' shoulder is much less pronounced in similarity with the spectral shape typically shown by LS compounds. We note that this implies that caution should be taken when assigning the presence of a weak Kβ' to a LS state. Theoretical calculations accounting for the degree of metallicity could perhaps shed more light on this part.

Table 4.2: *Resistivity values at RT for compounds of Figure 4.10.*

Compound	$\rho_{RT}[m\Omega \cdot cm]$	Ref.
Fe	9.71×10^{-3}	[67]
FeS_2	0.02	[68]
$BaFe_2As_2$	0.33	[69]
FeS	2.3	[70]
Ba_2FeReO_6	2.65	[71]
Sr_2FeReO_6	3	[72]

Local symmetry In Figure 4.12 we compare the spectra of $NaFeO_2$ and $Na_{0.7}Mn_{0.5}Fe_{0.5}O_2$ compounds, both Fe^{3+} HS but with O_h and T_d local symmetry of the Fe ion, respectively. The tetrahedral $NaFeO_2$ [73] compounds shows a less pronounced shoulder and a shift towards high energies of the main peak with respect to the O_h-$Na_{0.7}Mn_{0.5}Fe_{0.5}O_2$ [74]. The $K\beta_{1,3}$ 1st moment shift of ~ 0.2 eV between $NaFeO_2$ and $Na_{0.7}Mn_{0.5}Fe_{0.5}O_2$ is in agreement with the shifts found between ionic and covalent compounds. Figure 4.11 shows the electron configuration for $NaFeO_2$ and $Na_{0.7}Mn_{0.5}Fe_{0.5}O_2$ including the crystal field symmetry splitting. We can observe that in the tetrahedral case more electrons are in the least tightly bound t_2 orbital. These electrons heavily mixed with ligands electrons and give the compound more covalent character. This explanation is still valid for other metals which has one more unpaired electron in the less bound orbitals t_2, compared to the O_h case. Another argument supporting the more covalent character of tetrahedral compounds in general comes from a simply consideration about symmetry: looking at the branching rules from a spherical to a T_d symmetry (Table 2.1, Chapter 1) we note that the symmetry class of the p orbitals is the same of the d orbitals, both fall in the T_2 class. This means a stronger p-d mixing between ligand and metal orbitals with respect to the O_h case. We can conclude that the different crystal environments which surround the metal ion change lead spectral modification through the different covalency degree of the metal-ligand bond. Gamblin et al. [42] found a similar evolution in Co^{2+} ($3d^7$ configuration) between O_h and T_d coordinations.

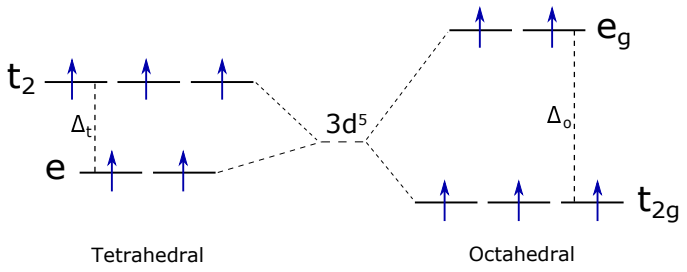

Figure 4.11: *$3d^5$ electronic configuration in tetrahedral and octahedral environments.*

After discussing the effects of covalency, metallicity and local symmetry in the Kβ spectra we now perform a general IAD and $K\beta_{1,3}$ 1st moment analysis including the data of all the compounds that were measured. The results are collected in Table 4.3. In Figure 4.13a, the IAD values from

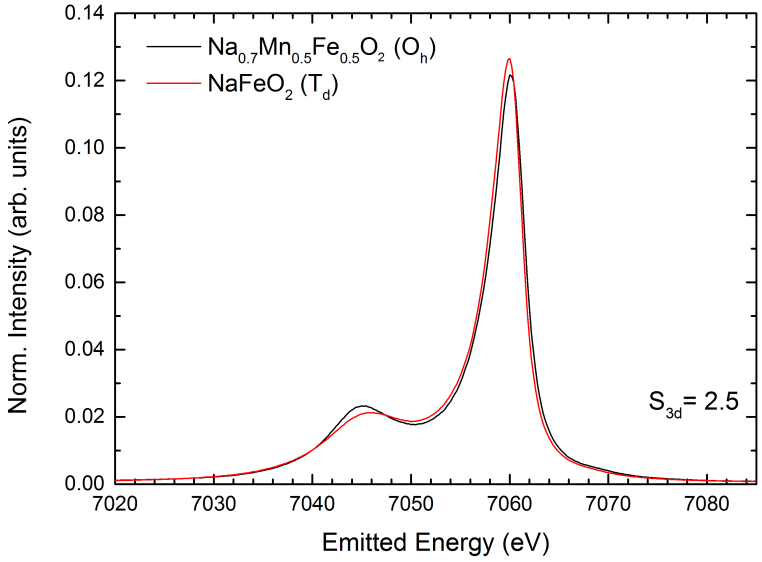

Figure 4.12: *Fe Kβ spectra of two compounds with similar chemical composition, same Fe oxidation state (+3) and spin state (HS), but different coordination. The spectra have been normalized to unit area in the range 7020-7085* eV.

this analysis are plotted as a function of the nominal 3d shell spin (S_{3d}), where the compounds appeared grouped into families for a first inspection. In Figure 4.13b are plotted the $K\beta_{1,3}$ 1st moments in a similar way. A preliminary conclusion is that both parameters show a very close behaviour both increasing when going from low to high values of S_{3d}, as expected [12, 75]. In addition, looking at fixed S_{3d} values one can identify a spread in the IAD and 1st moment values, in particular for the S_{3d}=2 and S_{3d}=2.5 compounds. In order to clarify this point, we have divided the previous figures into two plots where the x-axis has been separated into low S_{3d} (0-1.5) and high S_{3d} (2-2.5) regions as shown in Figure 4.14. In this case, each data point has been labelled with the corresponding compound. Looking at S_{3d}=2, from the labels we can see that FeS and $BaFe_2As_2$ have lower IAD values, according to their smoother Kβ' feature (typical of compounds with metallic behaviour, as seen before). For $FeTiO_3$ we can connect the slightly higher IAD with the possible presence of a small Fe^{3+} fraction [76]. Lastly for the Fe^{2+} water solutions and FeF_2 we can relate the higher IAD to their pronounced ionic character. Higher IAD values are also obtained for the ferric Fe^{3+} water solution and FeF_3 at S_{3d}=2.5, for the same reason. Regarding the $K\beta_{1,3}$ 1st moments the same can be concluded for the high S_{3d} region, while a smaller variation is seen in the low S_{3d} region between FeS_2 and $K_4Fe(CN)_6 \cdot 3\,H_2O$ compared to the IAD case. This can be understand looking at Figure 4.8 back in the text, where we can see that despite the tow compounds have a nominal S_{3d}=0, they show marked differences in the whole spectral area which manifests more in the IAD value, compared to the $K\beta_{1,3}$ 1st moment.

Table 4.3: *Compound chemical formulas, Fe formal valence, nominal spin value, relevant references, $K\beta_{1,3}$ 1st moment and IAD values using the FeS_2 as the reference. Also included are center-of-gravity (COG) and its energy shift with respect to FeS_2.*

Compound	Formal valence	Nominal Spin	Ref.	Kβ$_{1,3}$ 1st Moment (eV)	IAD	Kβ-Center of Gravity (eV)	COG shift (eV)
Fe	0	1	[64]	7058.54	0.182	7055.22	0.025
FeS_2	+2	0	-	7058.13	0	7055.20	0
$K_4Fe(CN)_6 \cdot 3\,H_2O$	+2	0	[77]	7058.02	0.148	7055.29	0.089
FeS	+2	2	[63]	7058.66	0.238	7055.23	0.037
FeF_2	+2	2	-	7059.46	0.517	7055.45	0.255
FeO	+2	2	[78], [79]	7058.94	0.354	7055.23	0.032
$FeTiO_3$	+2	2	[76]	7059.17	0.429	7055.39	0.197
$BaFe_2As_2$	+2	2	-	7058.4	0.121	7055.25	0.051
Fe^{2+} water solution	+2	2	[80]	7059.41	0.509	7055.52	0.325
$Fe_4[Fe(CN)_6]_3$	+2.57	1.43	[60], [81]	7058.37	0.326	7055.33	0.140
$LiFePO_4$	+2.2	2.1	[82]	7059.2	0.439	7055.38	0.185
Co_2FeO_4	+2.4	2.2	[83]	7059.04	0.387	7055.28	0.085
$YbFe_2O_4$	+2.5	2.25	[84]	7059.05	0.385	7055.29	0.094
YFe_2O_4	+2.5	2.25	-	7059.05	0.385	7055.29	0.095
$LuFe_2O_4$	+2.5	2.25	[84]	7059.06	0.389	7055.29	0.090
$CrFe_2O_4$	+2.5	2.25	-	7058.98	0.364	7055.29	0.093
$Sr_2Fe_{1.5}W_{0.5}O_6$	+2.5	2.25	-	7059.08	0.403	7055.25	0.054
Fe_3O_4	+2.67	2.3	[79]	7059.03	0.386	7055.23	0.032
Ba_2FeReO_6	+2.75	2.35	[85]	7059.09	0.407	7055.29	0.094
Sr_2FeReO_6	+2.7	2.33	[86]	7059.11	0.415	7055.28	0.083
$K_3Fe(CN)_6$	+3	0.5	[77]	7058.27	0.063	7055.28	0.083
$NaFeO_2$	+3	2.5	[73]	7058.97	0.368	7055.20	0.002
$LuFeCoO_4$	+3	2.5	[87]	7059.08	0.399	7055.29	0.092
α-Fe_2O_3	+3	2.5	[79]	7059.07	0.404	7055.16	-0.040
γ-Fe_2O_3	+3	2.5	[79]	7059.05	0.396	7055.23	0.038
Ca_2FeReO_6	+3	2.5	[86]	7059.07	0.399	7055.24	0.048
$SmFeO_3$	+3	2.5	-	7050.11	0.418	7055.20	0.004
$LaFeO_3$	+3	2.5	[88]	7059.1	0.411	7055.22	0.022
$MnFe_2O_4$	+3	2.5	[89]	7059.08	0.403	7055.33	0.130
$LaFe_{0.5}Ga_{0.5}O_3$	+3	2.5	[90]	7059.14	0.430	7055.21	0.010
$Na_{0.7}Mn_{0.5}Fe_{0.5}O_2$	+3	2.5	[74]	7059.15	0.430	7055.31	0.113
FeF_3	+3	2.5	[43]	7059.58	0.563	7055.44	0.244
Fe^{3+} water solution	+3	2.5	[80]	7059.33	0.493	7055.40	0.208
$La_{0.33}Sr_{0.67}FeO_3$	+3.65	2.18	[91], [92]	7059	0.379	7055.18	-0.022
$Pr_{0.33}Sr_{0.67}FeO_3$	+3.65	2.18	[91]	7059	0.378	7055.18	-0.014
$SrFeO_3$	+4	2	-	7058.98	0.366	7055.20	0.003

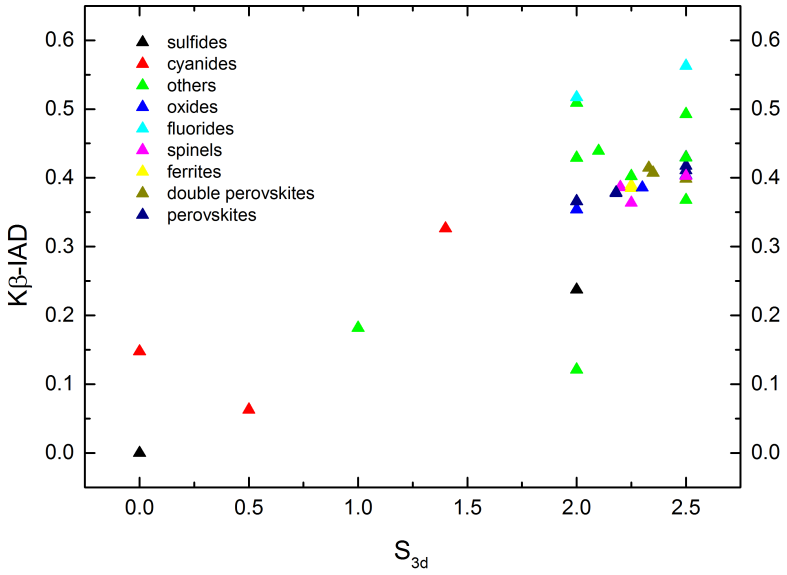

(a)

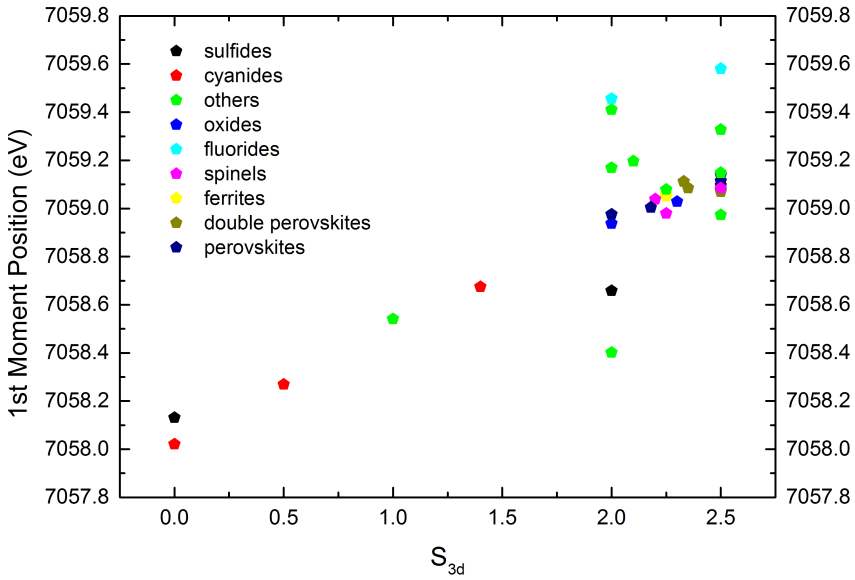

(b)

Figure 4.13: *(a) IAD values and (b) 1st moment values plotted against the nominal 3d spin moment of the Fe ion (S_{3d}). FeS_2 has been taken as a reference for IADs.*

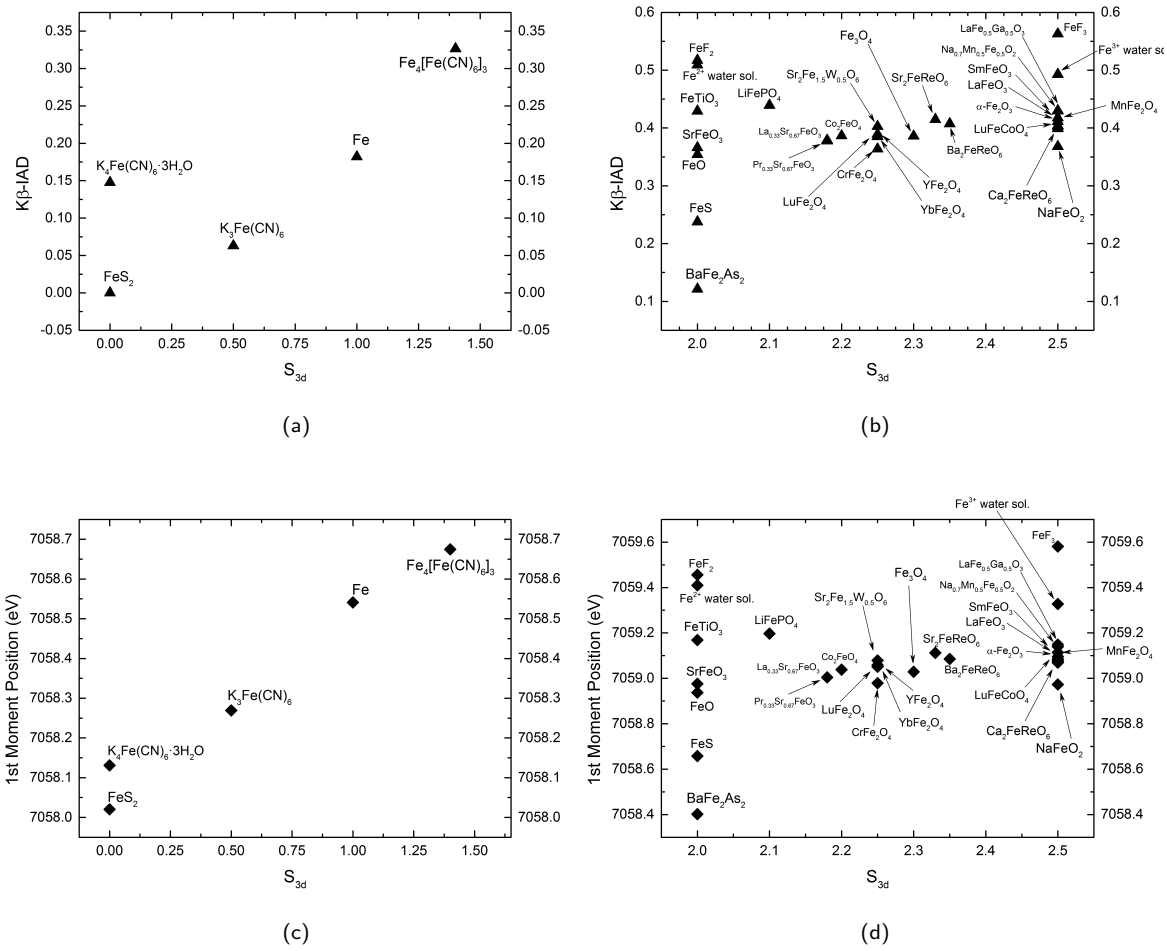

Figure 4.14: *(a), (b) IAD values and (c), (d) $K\beta_{1,3}$ 1st moment of all the measured compounds grouped into families Figure 4.13 in 2 separate plots, where we have divided for the sake of clarity the S_{3d} values into two regions: 0-1.5 and 2-2.5.*

In the last evaluation, as suggested by Glatzel et al. [12], we have also performed the IAD analysis after aligning the spectra to have the same center-of-gravity (COG) in order to get rid of the energy shift due to the screening of the core-hole potential, which depends on the valence charge density (see Chapter 2). For the more covalent compounds the electron cloud is more delocalized, meaning that the probability of find electrons near the nucleus is bigger. This results in a more effective effective screening of the 1s core-hole [93]. From the COG values (Figure 4.15) we can agree with this picture and say that the higher values are found for the more ionic compounds, were the core-hole is less screened. To have all the spectra with the same COG we have shifted all the spectra to have the same COG of the FeS_2. After that, we have again performed the IAD analysis, where the new IAD values are expected to be influenced only by the changes in the 3p-3d exchange splitting due to the different spin moment of the Fe 3d shell. The resulting IAD values are showed in Figure 4.16. The values are overall a bit smaller compared to the analysis without COG alignment and a similar trend for S_{3d} values is appreciated. The largest reduction in IAD take place for the more ionic compounds (for example the fluorides, cyan triangles in Figure 4.16) because of the less effective screening of the core-hole. In Figure 4.17 we illustrate the difference signals between FeO and FeF_2 and the reference FeS_2 with and without align to the COG. Very small differences are found and the IAD is more reduced for FeF_2 compared to FeO in line with the ionic character.

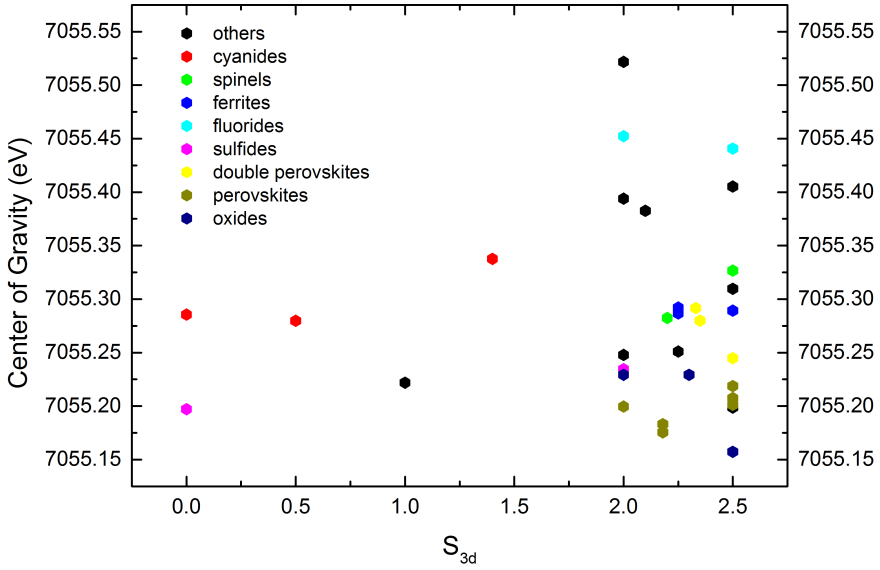

Figure 4.15: *COG position of all the compounds vs the nominal spin of the 3d shell.*

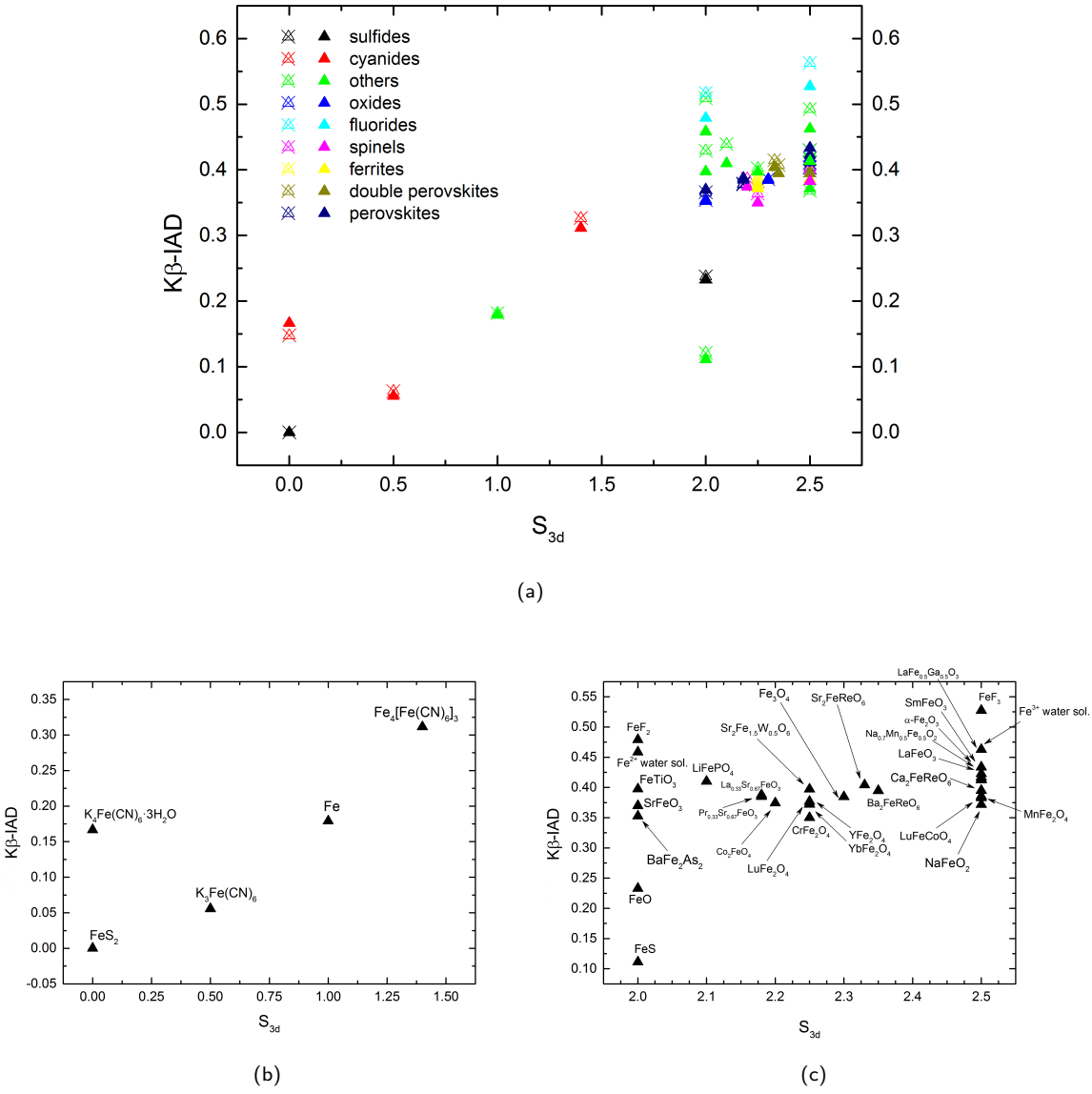

Figure 4.16: *IAD values after COG alignment as described in the text. In panel (a) both IAD with (filled triangles) and without (empty triangles) COG alignment are compared. (b) and (c) show the same data plot of (a) divided in 2 separate plots, where we have divided for the sake of clarity the S_{3d} values into two regions: 0-1.5 and 2-2.5.*

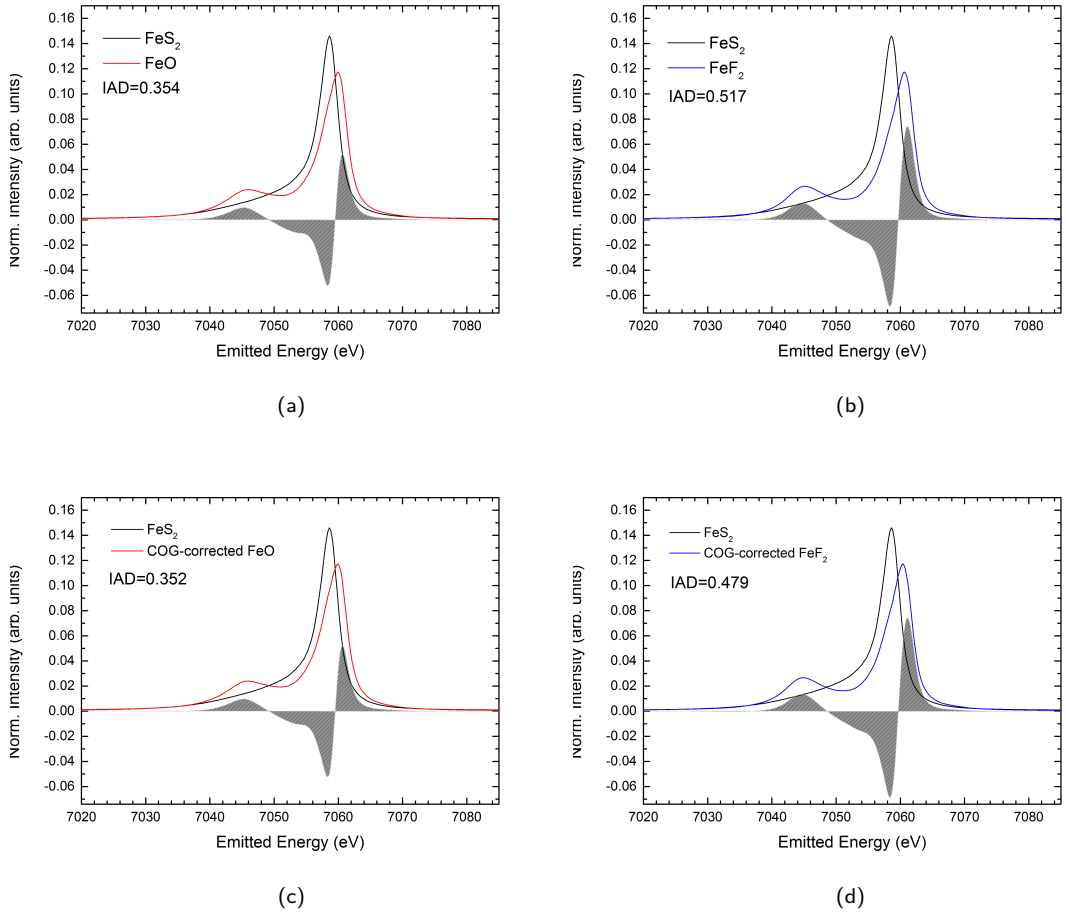

Figure 4.17: *Difference spectra (grey dashed area) between FeO and FeF_2 and the reference FeS_2 before (top) and after (down) the COG alignment. The resulting IAD values are indicated in the figures.*

4.3.2 Fe Kα XES

We present the Kα XES data in the same way done for the Kβ part. Figure 4.18, 4.19 and 4.20 show the spectra separated into Fe^{3+}, Fe^{2+} and mixed-valence compounds.

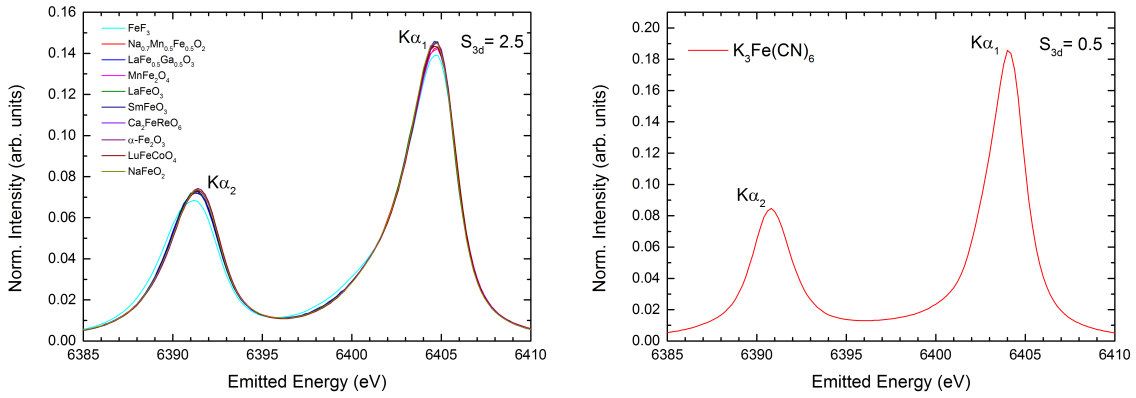

(a) *HS Fe(III) compounds* (b) *LS Fe(III) compound*

Figure 4.18: *Fe Ka spectra of the Fe(III) compounds. The spectra have been normalized to unit area in the range 6385-6410* eV.

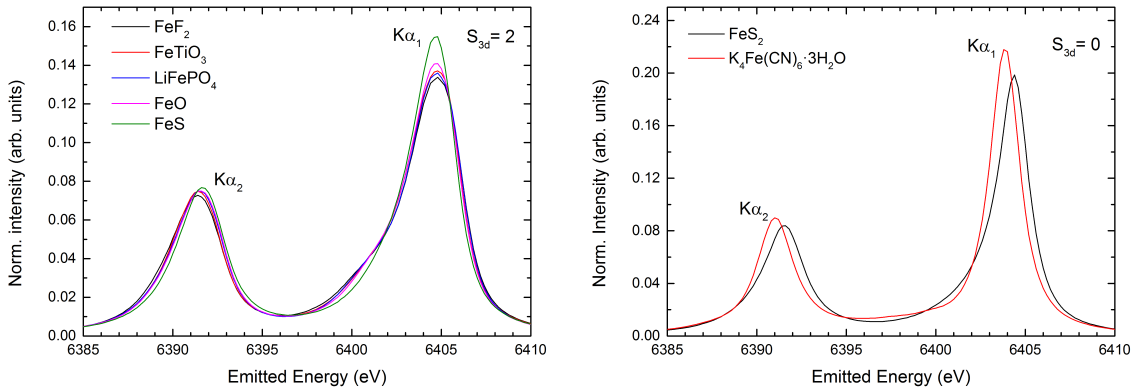

(a) *HS Fe(II) compounds* (b) *LS Fe(II) compounds*

Figure 4.19: *Fe Ka spectra of the Fe(II) compounds. The spectra have been normalized to unit area in the range 6385-6410* eV.

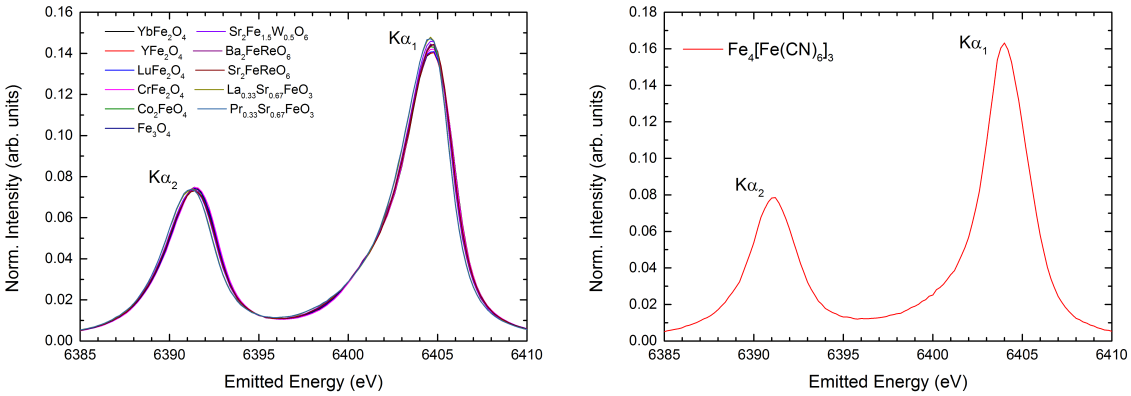

(a) *HS Fe mixed-valence compounds* (b) *HS-LS Fe mixed-valence compound*

Figure 4.20: *Fe Ka spectra of the mixed-valence compounds. The spectra have been normalized to unit area in the range 6385-6410* eV.

The $K\alpha_1$ peak appears centered at $\sim$ 6404 eV and the $K\alpha_2$ peak at $\sim$ 6392 eV in all the samples. In Figure 4.18a FeF_3 appears the more different with respect to the others, showing lower intensities in the $K\alpha_1$ and $K\alpha_2$ and a visible shift of the $K\alpha_2$ to lower energies. In Figure 4.19 FeS is remarkably different in the Fe^{2+} HS set, showing higher intensity in the $K\alpha_1$ peak and small shift towards high energies of the $K\alpha_2$ peak. Also, very different spectral changes are visible between the two Fe^{2+} LS compounds (Figure 4.19b). We do not note any significant differences for the mixed-valence compounds (Figure 4.20a).

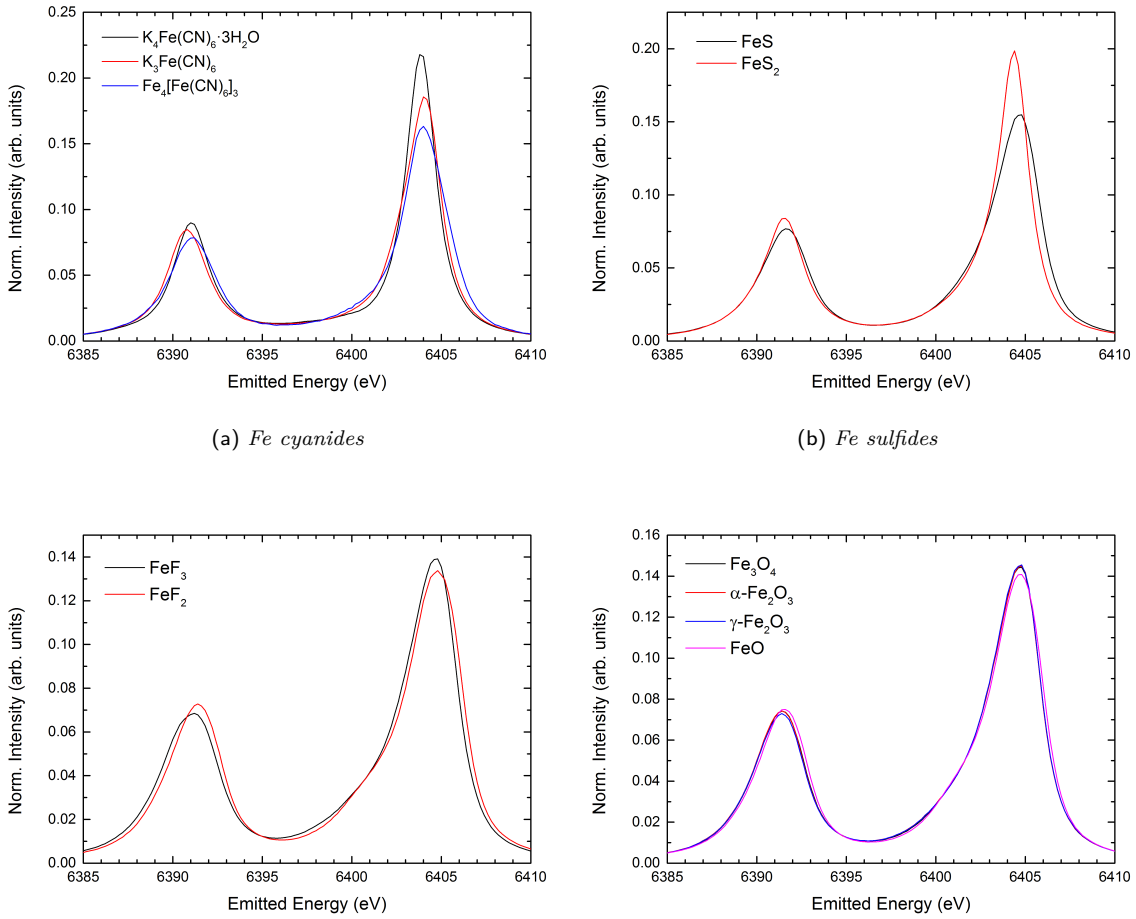

(a) *Fe cyanides* (b) *Fe sulfides*

(c) *Fe fluorides* (d) *Fe oxides*

Figure 4.21: *Fe Ka spectra of the compounds belonging to different families, with the same ligands. The spectra have been normalized to unit area in the range 6385-6410* eV.

Before moving to the quantitative analysis, we compare in Figure 4.21 compounds with the same ligands, as we for the Kβ. Also here there are visible spectral changes as a function of the nominal spin. Changes in the intensities and linewidths can be found when the spin value changes: for the cyanides (Figure 4.21a) the increasing of the nominal spin value from S_{3d}=0 for $K_3Fe(CN)_6$ to the S_{3d}=1.4 for the $Fe_4[Fe(CN)_6]_3$ goes together with the increasing intensities and a linewidth variation for both Kα$_1$ and Kα$_2$ peaks. Also remarkably changes can be visible for the sulfides (Figure 4.21b), coherent with the variation of the spin of ΔS_{3d}= 2. Lastly, the fluorides and the oxides (Figure 4.21c, 4.21d) show less pronounced changes because of the smaller variation of the spin value (ΔS_{3d} = 0.5). Finally we have extracted the following quantitative informations from the spectra: the full-width-at-half-maximum (FWHM) of the Kα$_1$ line and the IAD values following the same procedure performed for the Kβ spectra. The results of this analysis are collected in Table 4.4. Figure 4.22a and 4.22b show the Kα$_1$ FWHMs and IAD data respectively as a function of the nominal spin value. Similar trends as found in the Kβ analysis are found for FWHMs and IADs. The latter result to be overall smaller than the Kβ-IADs. Also

the outliners with S_{3d}=2 and S_{3d}=2.5 are the same discussed for IAD.

Table 4.4: *Compound chemical formulas, Fe formal valence, nominal spin value, relevant references, Ka-IAD and Ka_1 FWHMs.*

Compound	Formal valence	Nominal Spin	Ref.	Kα-IAD	$Kα_1$ FWHM (eV)
Fe	0	1	[64]	0.069	2.78
FeS_2	+2	0	-	0	2.30
$K_4Fe(CN)_6 \cdot {}_3H_2O$	+2	0	[77]	0.228	1.96
FeS	+2	2	[63]	0.128	3.26
FeF_2	+2	2	-	0.221	3.89
FeO	+2	2	[78], [79]	0.172	3.69
$FeTiO_3$	+2	2	[76]	0.192	3.79
$BaFe_2As_2$	+2	2	-	0.079	2.75
$Fe_4[Fe(CN)_6]_3$	+2.57	1.43	[60], [81]	0.141	2.95
$LiFePO_4$	+2.2	2.1	[82]	0.196	3.80
Co_2FeO_4	+2.4	2.2	[83]	0.168	3.58
$YbFe_2O_4$	+2.5	2.25	[84]	0.174	3.67
YFe_2O_4	+2.5	2.25	-	0.173	3.67
$LuFe_2O_4$	+2.5	2.25	[84]	0.173	3.66
$CrFe_2O_4$	+2.5	2.25	-	0.164	3.63
$Sr_2Fe_{1.5}W_{0.5}O_6$	+2.5	2.25	-	0.167	3.50
Fe_3O_4	+2.67	2.3	[79]	0.164	3.55
Ba_2FeReO_6	+2.75	2.35	[85]	0.170	3.58
Sr_2FeReO_6	+2.7	2.33	[86]	0.174	3.58
$K_3Fe(CN)_6$	+3	0.5	[77]	0.198	2.51
$NaFeO_2$	+3	2.5	[73]	0.164	3.50
$LuFeCoO_4$	+3	2.5	[87]	0.169	3.58
α-Fe_2O_3	+3	2.5	[79]	0.168	3.53
γ-Fe_2O_3	+3	2.5	[79]	0.169	3.54
Ca_2FeReO_6	+3	2.5	[86]	0.167	3.55
$SmFeO_3$	+3	2.5	-	0.173	3.53
$LaFeO_3$	+3	2.5	[88]	0.171	3.53
$MnFe_2O_4$	+3	2.5	[89]	0.174	3.63
$LaFe_{0.5}Ga_{0.5}O_3$	+3	2.5	[90]	0.178	3.56
$Na_{0.7}Mn_{0.5}Fe_{0.5}O_2$	+3	2.5	[74]	0.181	3.62
FeF_3	+3	2.5	[43]	0.219	3.71
$La_{0.33}Sr_{0.67}FeO_3$	+3.65	2.18	[91], [92]	0.167	3.44
$Pr_{0.33}Sr_{0.67}FeO_3$	+3.65	2.18	[91]	0.168	3.45
$SrFeO_3$	+4	2	-	0.159	3.35

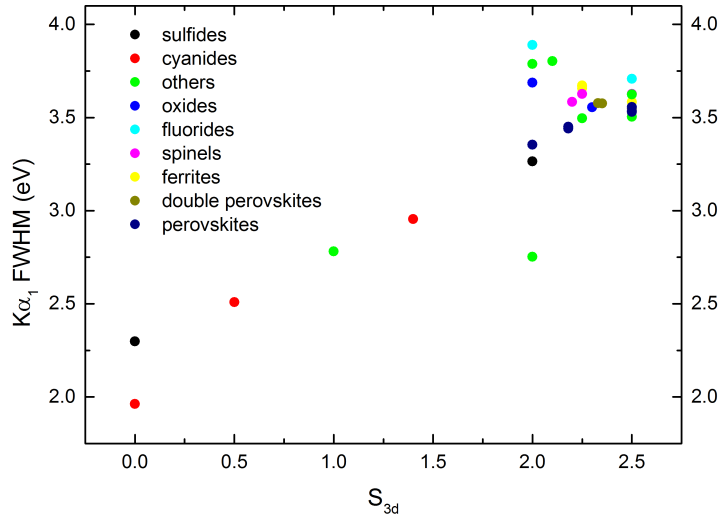

(a)

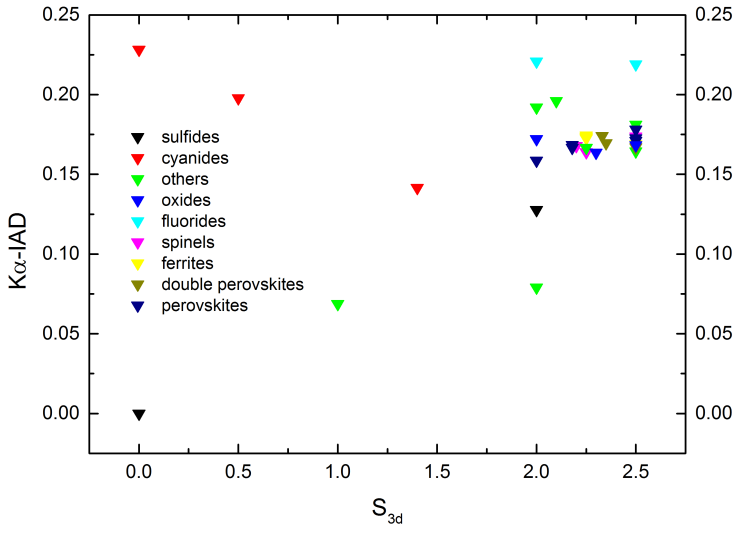

(b)

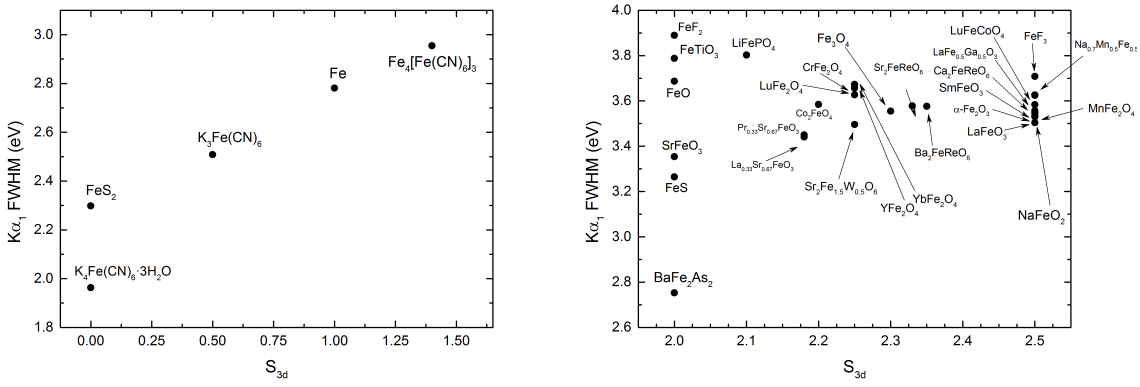

Figure 4.22: *(a) IAD values for the Ka. (b) Ka FWHM values including the splitting of the S_{3d} values into the two regions, 0-1.5 and 2-2.5.*

4.3.3 Comparison between Kβ and Kα

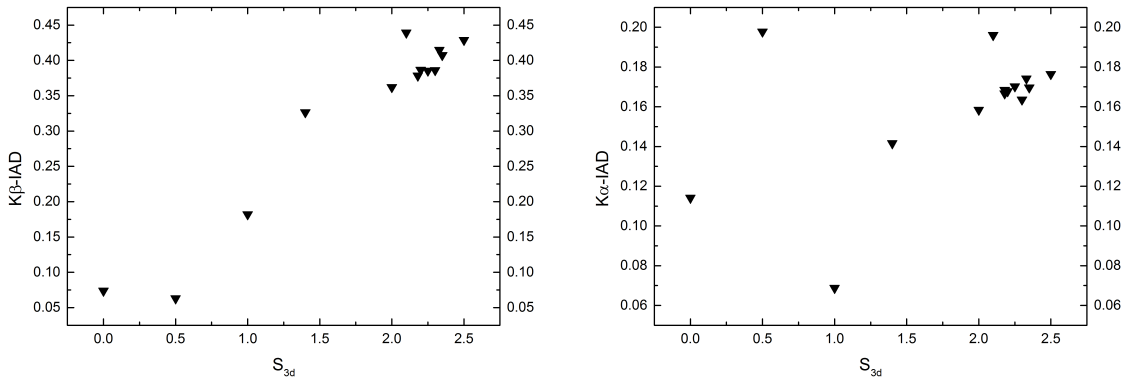

(a) *Kβ-IAD values* (b) *Ka-IAD values*

Figure 4.23: *IAD plot averaging the IAD values of the compounds with the same nominal spin.*

In this last section we compare the results obtained from the Kβ and Kα spectra in order to draw some general conclusions about the way the two types of emission lines are sensitive to the 3d metal spin. For that, we will focus on the comparison between the IAD analysis performed for both types of emission lines. Figure 4.23 shows the IAD results as a function of the nominal spin with the particularity that a mean IAD value is shown for each S_{3d} for the sake of simplicity. A first result relates to the magnitude of the IADs, the Kα-IAD values are approximately a factor of two smaller than the Kβ-IAD values. This smaller sensitivity of the Kα lines compared to Kβ can be expected because the 2p-3d interaction is weaker than the 3p-3d. Still, because the Kα lines are about a factor 10 more intense than Kβ, if both lines provide the same spin-state evolution it would be preferable to perform Kα experiments over Kβ in spin-state studies. Indeed a recent combined Kα-Kβ study [47] in Fe metal, $FeTiO_3$, Fe_2O_3 and FeS_2 found the same behaviour in the spin evolution obtained from both emission lines spectra and claimed the same spin-sensitivity in both Kα and Kβ. However as follows from our results shown in Figure 4.23, this does not seem to be strictly the case. While the Kβ-IAD values follow a monotonic increase with the nominal spin, the Kα-IAD values show a less clear trend. Detailed analysis of the latter is still on-going.

Finally we notice that, despite the sensitivity of the Kα lines to the 3d shell via exchange interaction is known to be smaller with respect to the Kβ, the same increasing trend with the nominal S_{3d} is found in the $K\alpha_1$ FWHMs. But looking at the Kα-IAD values (and before that at the Kα spectra), on the other hand, we have noticed that they are at least a factor of two smaller than the Kβ-IAD values, as already said. The FWHM seems to be a key factor for the Kα analysis and therefore has to be more carefully analysed because can bring additional information about the spin value and, more in general, about the exchange interaction dependence of the K-emission lines.

Conclusions and outlook

This work aimed at a deeper understanding of the K-emission line spectra of 3d transition metal compounds. The Kβ and Kα emission lines are very useful to extract local spin moment information in 3d transition metal compounds as they are shaped by the 3p-3d and 2p-3d exchange interactions, respectively, which confer them an indirect sensitivity to the net 3d shell spin. In particular, due to the fact that the 3p-3d interaction is stronger than the 2p-3d, traditionally Kβ spectroscopy has been preferred. Our approach was to perform Kβ and Kα x-ray emission measurements on a large variety of iron compounds to study the dependence of the spectral lineshape on other factors than the spin state namely the covalency, metallicity or the metal local symmetry. A few similar studies were done before [42, 43, 47, 77] but they lack of the generality required for a comprehensive understanding. They either measured only a few compounds or performed only Kβ measurements. We have measured a substantial number of iron compounds (more than 30) with different oxidation (+2, +3, +4 and mixed-valence), spin state (high spin/low spin and mixed spin), ligands (fluorides, sulfides, oxides, etc.), local coordination (octahedral, tetrahedral) and different covalent and metallic degrees. This general characterization has allowed us finding that, in addition to the spin state, all the mentioned factors also influence significantly the lineshape. We have quantitatively analysed the spectral changes in terms of different parameters commonly used in the analysis like the integrated absolute difference (IAD) or the 1st moment of the $K\beta_{1,3}$ peak. From these parameters a linear relationship between them and the nominal spin is commonly obtained from model compounds to then extrapolate and determine the spin state on real samples. Our general study has allowed us to obtain a global picture of the dependence of these parameters with the nominal spin state. A first result in the case of Kβ XES is that both IAD and the first moment show a similar behaviour. We note that both parameters reflect the changes in the splitting between the $K\beta_{1,3}$ and Kβ', which can be approximated by $J(2S+1)$, where J is the exchange integral between the 3p and 3d electrons and S is the 3d shell spin. A second important point is that different values of the IAD and $K\beta_{1,3}$ 1st moment are obtained for compounds with the same spin state. By comparing data of compounds with different electronegativity, metallic behaviour and also local coordination we have found out that in those cases where the 3d states have a more delocalized behaviour, the IADs and $K\beta_{1,3}$ 1st moments appear systematically reduced. This can be understood as due to the smaller 3p-3d exchange interaction due to the weaker overlap between the 3p and 3d wavefunctions. In this way, our general characterization can help the scientific

community interested in the spin-state determination by means of XES spectroscopy. Importantly, one should measure appropriate references together with the compounds under study for a reliable analysis and the correct determination of the spin. Another aspect that we have evaluated is the influence of the screening effects in the Kβ XES by aligning the spectra to have the same center-of-gravity and then performing the IAD analysis. No significant changes were found in the IAD values with and without aligning previously the spectra so it can be concluded that the screening effects are very small and the spectra are mainly dominated by the 3p-3d exchange interaction. Finally, the quantitative analysis on the Kα spectra suggests that the FWHM of the $K\alpha_1$ peak shows a similar evolution compared to the Kβ-IAD and $K\beta_{1,3}$ 1st moment. We also performed an IAD analysis of the Kα spectra and obtained IAD values about a factor 2 smaller than the Kβ-IADs, which can be expected from the weaker 2p-3d interaction compared to 3p-3d. The Kα lines are almost 10 times more intense than Kβ and thus it would still make sense to measure the Kα lines instead of the Kβ lines. However, our preliminary analysis shows a different trend with the nominal spin-state between Kα-IADs and Kβ-IADs.

Plenty of possibilities have been opened by this study. Selected samples can be added to our work to confirm our picture and the Kα lines still deserve more accurate and detailed analysis as they have been found to be also quite sensitive to the valence 3d electrons configuration. Also another interesting point is to look at shape of the difference spectra in order to identify characteristic features. We note that XES is widely used nowadays in pump and probe experiments even at XFELs so understanding the difference signal lineshape is of great interest and importance.

Finally, ideally our study could be further supported by theoretical calculations. For example by means of density functional ab initio calculations to obtain the charge density on the Fe 3d states via a population analysis in order to deduce theoretical spin values to compare with our experimental results [27].

Acknowledgements

The work done for this thesis could not have been possible without the support and the help of many people, who assisted me all over my traineeship at the ESRF. First of all my gratitude goes to Prof. Giacomo Ghiringhelli, who gave me the opportunity to spend a period abroad studying and working in one of the best scientific environment of the world. Without him this experience would not be possible at all. I want to extend my gratitude to ID26 boss Pieter Glatzel, who accept me to work in his team and give me some precious advices and hints. Then, but not less important, very special thanks go to Sara Lafuerza, who always assisted me with patience and method, teaching me how to deal with passion and dedication to the experiments and supervised the realisation of this thesis. Also, my thanks go to all the staff of ID26, in particular Rafał Baran, Lucia Amidani, Marius Retegan, Blanka Detlefs, Anurag Kawde and Mauro Rovezzi. Every day spent with them has been a great pleasure for me and I wish everyone to find such a wonderful team to work with. I would also like to thank the sample providers J. Blasco and D. Baster, who made possible this experiment. A special mention goes to my girlfriend, Martina: we spent all these years of study together facing difficult moments, but always supporting each other. She also experienced how stressful can be a boyfriend abroad during this thesis but never stops to love and support him. Thanks to my family which provide me all the necessary to face with these years spent at the university and never stops to believe in me. Thanks to my roomates Manuel and Edoardo, and to all people I met in Grenoble, who made special this period of my life.

Last, but definitely not least, thanks to all my travel companions during this 5 years of study: from the friends of Unipv, Giacomino, Ferri, Ciuffi, La Rossa, Mate, Ari, Brasa, to the ones of Polimi, Gaggio, Lorè, Mike (formerly known as "I Blalli"), Beppe, Giorgio, Tommy, Alberto, Fra, Sele, Chiara, Mario, Aurè, Giuggio, Carlo, James, Stella, Cesare...Thanks for everything.

Figure A1: *ID26 beamline staff. From the right: Pieter Glatzel, Blanka Detlefs, Mauro Rovezzi, Rafał Baran, Sara Lafuerza, Marius Retegan, Magdalena Piskorz, Anurag Kawde, Lucia Amidani and myself.*

Bibliography

[1] K. Tsutsumi. "The X-ray Non-diagram Lines Kβ' of Some Compounds of the iron Group". In: *Journal of the Physical Society of Japan* 14.12 (1959), pp. 1696–1706.

[2] J. Finster, G. Leonhardt, and A. Meisel. "On The Shape And Width Of The Main Lines Of X-ray K-Emission Of The 3d And 4d Elements". In: *Le Journal de Physique Colloques* 32.C4 (1971), pp. C4–218.

[3] C. Chantler, A. Hayward, and I. Grant. "Theoretical Determination of Characteristic X-Ray Lines and the Copper Kα Spectrum". In: *Physical review letters* 103.12 (2009), p. 123002.

[4] K. Tsutsumi and H. Nakamori. "X-ray K emission spectra of chromium in various chromium compounds". In: *Journal of the Physical Society of Japan* 25.5 (1968), pp. 1418–1423.

[5] K. Tsutsumi and H. Nakamori. "X-Ray Spectra and Electronic Structure of Matter". In: (1973).

[6] G. Vankó et al. "Probing the 3d spin momentum with X-ray emission spectroscopy: The case of molecular-spin transitions". In: *The Journal of Physical Chemistry B* 110.24 (2006), pp. 11647–11653.

[7] G. Vankó et al. "Temperature-and pressure-induced spin-state transitions in $LaCoO_3$". In: *Physical Review B* 73.2 (2006), p. 024424.

[8] J. Badro et al. "Electronic transitions in perovskite: Possible nonconvecting layers in the lower mantle". In: *Science* 305.5682 (2004), pp. 383–386.

[9] M. Sikora et al. "Evolution of charge and spin state of transition metals in the $LaMn_{1-x}Co_xO_3$ perovskite series". In: *Journal of Applied Physics* 103.7 (2008), p. 07C907.

[10] H. Gretarsson et al. "Revealing the dual nature of magnetism in iron pnictides and iron chalcogenides using x-ray emission spectroscopy". In: *Physical Review B* 84.10 (2011), p. 100509.

[11] F. De Groot and A. Kotani. *Core level spectroscopy of solids*. CRC press, 2008.

[12] P. Glatzel and U. Bergmann. "High resolution 1s core hole X-ray spectroscopy in 3d transition metal complexes-electronic and structural information". In: *Coordination chemistry reviews* 249.1 (2005), pp. 65–95.

[13] R. G. Newton. *Scattering theory of waves and particles*. Springer Science & Business Media, 1982.

[14] *ALS. X-ray data booklet*. URL: http://xdb.lbl.gov/.

[15] O. Klein and Y. Nishina. "Über die Streuung von Strahlung durch freie Elektronen nach der neuen relativistischen Quantendynamik von Dirac". In: *Zeitschrift für Physik* 52.11-12 (1929), pp. 853–868.

[16] A. H. Compton. "A quantum theory of the scattering of X-rays by light elements". In: *Physical review* 21.5 (1923), p. 483.

[17] A. Einstein. "The photoelectric effect". In: *Ann. Phys* 17.132 (1905), p. 4.

[18] J. P. Rueff and A. Shukla. "Inelastic x-ray scattering by electronic excitations under high pressure". In: *Reviews of Modern Physics* 82.1 (2010), p. 847.

[19] H. A. Kramers and W. Heisenberg. "Über die streuung von strahlung durch atome". In: *Zeitschrift für Physik A Hadrons and Nuclei* 31.1 (1925), pp. 681–708.

[20] M. Blume. "Magnetic scattering of x rays". In: *Journal of Applied Physics* 57.8 (1985), pp. 3615–3618.

[21] D. J. Griffiths. *Introduction to quantum mechanics*. Cambridge University Press, 2016.

[22] F. E. Low. "Scattering of Light of Very Low Frequency by Systems of Spin 1/2". In: *Physical Review* 96.5 (1954), p. 1428.

[23] G. Ruocco and F. Sette. "Inelastic X-ray scattering: A new spectroscopy tool to investigate the atomic dynamics in condensed matter". In: *Conference Proceedings-Italian Physical Society*. Vol. 82. Editrice Compositori; 1999. 2003, pp. 623–658.

[24] P. Dirac. *The principles of quantum mechanics*. 4th. Oxford university press, 1966.

[25] A. Kotani and S. Shin. "Resonant inelastic x-ray scattering spectra for electrons in solids". In: *Reviews of Modern Physics* 73.1 (2001), p. 203.

[26] P. Glatzel, R. Alonso-Mori, and D. Sokaras. "Hard x-ray photon-in/photon-out spectroscopy: instrumentation, theory and applications". In: *X-Ray Absorption and X-Ray Emission Spectroscopy: Theory and Applications* 1 (2016).

[27] M. Rovezzi and P. Glatzel. "Hard X-ray emission spectroscopy: a powerful tool for the characterization of magnetic semiconductors". In: *Semiconductor Science and Technology* 29.2 (2014), p. 023002.

[28] U. Bergmann and P. Glatzel. "X-ray emission spectroscopy". In: *Photosynthesis research* 102.2-3 (2009), p. 255.

[29] C. Brouder. "Angular dependence of X-ray absorption spectra". In: *Journal of Physics: Condensed Matter* 2.3 (1990), p. 701.

[30] P. H. Butler. *Point group symmetry applications: methods and tables*. Springer US, 1981.

[31] R. S. Mulliken. "Electronic structures of polyatomic molecules and valence. IV. Electronic states, quantum theory of the double bond". In: *Physical Review* 43.4 (1933), p. 279.

[32] R. J. Lancashire. *Interpretation of the spectra of first-row transition metal complexes using Tanabe-Sugano diagrams*. URL: http://wwwchem.uwimona.edu.jm/courses/C21Jspec_TS.html.

[33] P. Glatzel. *X-ray fluorescence emission following K capture and 1s photoionization of Mn and Fe in various chemical environments*. Tech. rep. DESY, 2001.

[34] L. Mattheiss. "Electronic Structure of the 3 d Transition-Metal Monoxides. I. Energy-Band Results". In: *Physical Review B* 5.2 (1972), p. 290.

[35] A. Kotani and N. Suzuki. *Recent Advances in Magnetism of Transition Metal Compounds: Festschrift in Honour of Professor K Motizuki*. World Scientific, 1993.

[36] J. H. Van Vleck. *The theory of electric and magnetic susceptibilities*. Oxford University Press, 1932.

[37] F. De Groot et al. "Charge transfer multiplet calculations of the K beta X-ray emission spectra of divalent nickel compounds". In: *Journal of Physics: Condensed Matter* 6.34 (1994), p. 6875.

[38] E. J. Konopinski. *The theory of beta radioactivity*. Clarendon Press, 1966.

[39] P. Glatzel et al. "Influence of the core hole on Kβ emission following photoionization or orbital electron capture: A comparison using MnO and $^{55}Fe_2O_3$". In: *Physical Review B* 64.4 (2001), p. 045109.

[40] X. Wang et al. "High-resolution x-ray fluorescence and excitation spectroscopy of metalloproteins". In: *Journal of synchrotron radiation* 4.4 (1997), pp. 236–242.

[41] T. Tyson et al. "Valence state of Mn in Ca-doped $LaMnO_3$ studied by high-resolution Mn Kβ emission spectroscopy". In: *Physical Review B* 60.7 (1999), p. 4665.

[42] S. D. Gamblin and D. S. Urch. "Metal Kβ X-ray emission spectra of first row transition metal compounds". In: *Journal of Electron Spectroscopy and Related Phenomena* 113.2 (2001), pp. 179–192.

[43] X. Kβ Mainline. "X-ray Emission Spectroscopy as an Experimental Probe of Metal-Ligand Covalency Pollock, Christopher J.; Delgado-Jaime, Mario Ulises; Atanasov, Mihail; Neese, Frank; DeBeer". In: *Journal of the American Chemical Society* 136.26 (2014), pp. 9453–9463.

[44] F. Neese and E. I. Solomon. "Interpretation and Calculation of Spin-Hamiltonian Parameters in Transition Metal Complexes". In: *Magnetism: Molecules to Materials: 5 Volumes Set* (2003), pp. 345–466.

[45] C. Suzuki et al. "Electronic structures of 3d transition metal (Ti–Cu) oxides probed by a core hole". In: *Chemical physics* 247.3 (1999), pp. 453–470.

[46] X. Wang, F. M. de Groot, and S. P. Cramer. "Spin-polarized x-ray emission of 3d transition-metal ions: A comparison via Kα and Kβ detection". In: *Physical Review B* 56.8 (1997), p. 4553.

[47] A. Svyazhin et al. "Local moments and electronic correlations in Fe-based Heusler alloys: Kα x-ray emission spectra measurements". In: *Journal of Alloys and Compounds* 679 (2016), pp. 268–276.

[48] J. Kawai et al. “Charge-transfer effect on the linewidth of Fe Kα X-ray fluorescence spectra”. In: *Physical Review B* 50.16 (1994), p. 11347.

[49] C. Suzuki et al. “Local spin moment of $LaCoO_3$ probed by a core hole”. In: *Chemical physics* 241.1 (1999), pp. 17–27.

[50] *ESRF website*. URL: http://www.esrf.eu.

[51] J. Als-Nielsen and D. McMorrow. *Elements of modern X-ray physics*. John Wiley & Sons, 2011.

[52] N. W. Ashcroft, N. D. Mermin, and S. Rodriguez. *Solid state physics*. 1978.

[53] B. E. Warren. *X-ray Diffraction*. Courier Corporation, 1969.

[54] P. Glatzel et al. “Hard X-ray photon-in photon-out spectroscopy”. In: *Catalysis Today* 145.3 (2009), pp. 294–299.

[55] L. Ducotté et al. “Mechanical aspects of the ID26 emission spectrometer II: improving stability for a large instrument by the use of multiple air pad supports”. In: *Diamond Light Source Proceedings* 1.MEDSI-6 (2011), e26.

[56] M. Newville. “Fundamentals of XAFS”. In: *Reviews in Mineralogy and Geochemistry* 78.1 (2014), pp. 33–74.

[57] U. Bergmann et al. “Anisotropic valence→ core x-ray fluorescence from a $[Rh(en)_3][Mn(N)(CN)_5]\cdot H_2O$ single crystal: Experimental results and density functional calculations”. In: *The Journal of chemical physics* 116.5 (2002), pp. 2011–2015.

[58] J.-D. Cafun et al. “Absence of Ce^{3+} sites in chemically active colloidal ceria nanoparticles”. In: *ACS nano* 7.12 (2013), pp. 10726–10732.

[59] M. Oku, K. Wagatsuma, and T. Konishi. “Relation between 2p X-ray photoelectron and Kα X-ray emission spectra of manganese and iron oxides”. In: *Journal of electron spectroscopy and related phenomena* 98 (1999), pp. 277–285.

[60] P. Glatzel et al. “Site-selective EXAFS in mixed-valence compounds using high-resolution fluorescence detection: a study of iron in Prussian Blue”. In: *Inorganic chemistry* 41.12 (2002), pp. 3121–3127.

[61] A. Bocquet et al. “Electronic structure of 3d-transition-metal compounds by analysis of the 2p core-level photoemission spectra”. In: *Physical Review B* 46.7 (1992), p. 3771.

[62] A. Grosvenor et al. “Investigation of multiplet splitting of Fe 2p XPS spectra and bonding in iron compounds”. In: *Surface and Interface Analysis* 36.12 (2004), pp. 1564–1574.

[63] J.-P. Rueff et al. “Pressure-induced high-spin to low-spin transition in FeS evidenced by X-ray emission spectroscopy”. In: *Physical Review Letters* 82.16 (1999), p. 3284.

[64] G. Hölzer et al. “K$\alpha_{1,2}$ and K$\beta_{1,3}$ x-ray emission lines of the 3d transition metals”. In: *Physical Review A* 56.6 (1997), p. 4554.

[65] J. Gopalakrishnan et al. “Metallic and nonmetallic double perovskites: A case study of A_2FeReO_6 (A=Ca, Sr, Ba)”. In: *Physical Review B* 62.14 (2000), p. 9538.

[66] S. Lafuerza et al. “Evidences of Mott physics in iron pnictides from x-ray spectroscopy”. In: *arXiv: 1607.07417* (2016).

[67] J. Cutnell and K. Johnson. *Physics*. 4th. John Wiley and Sons Inc., 1998. ISBN: 0471191124.

[68] S. Lehner, K. Savage, and J. Ayers. “Vapor growth and characterization of pyrite (FeS_2) doped with Co, Ni, and As: variations in semiconducting properties”. In: *Journal of Crystal Growth* 286.2 (2006), pp. 306–317.

[69] M. Nakajima et al. “Normal-state charge dynamics in doped $BaFe_2As_2$: Roles of doping and necessary ingredients for superconductivity”. In: *arXiv preprint arXiv:1308.6133* (2013).

[70] C. K. Borg et al. “Strong anisotropy in nearly ideal tetrahedral superconducting FeS single crystals”. In: *Physical Review B* 93.9 (2016), p. 094522.

[71] B. Jeon et al. “Electronic structure of double perovskite A_2FeReO_6 (A= Ba, Ca): interplay between spin-orbit interaction, electron correlation, and lattice distortion”. In: *Journal of Physics: Condensed Matter* 22.34 (2010), p. 345602.

[72] D. Rai et al. “The electronic, magnetic and optical properties of double perovskite A_2FeReO_6 (A= Sr, Ba) from first principles approach”. In: *Computational Materials Science* 101 (2015), pp. 313–320.

[73] T. Omata et al. “Wurtzite-derived ternary I–III–O2 semiconductors”. In: *Science and Technology of Advanced Materials* 16.2 (2015), p. 024902.

[74] N. Yabuuchi et al. “P2-type $Na_x[Fe_{1/2}Mn_{1/2}]O_2$ made from earth-abundant elements for rechargeable Na batteries”. In: *Nature materials* 11.6 (2012), pp. 512–517.

[75] G. Peng et al. “High-resolution manganese X-ray-fluorescence spectroscopy-oxidation-state and spin-state sensitivity”. In: *Journal of the American Chemical Society* 116.7 (1994), pp. 2914–2920.

[76] T. Seda and G. Hearne. “Pressure induced $Fe^{2+}+Ti^{4+}\rightarrow Fe^{3+}+Ti^{3+}$ intervalence charge transfer and the Fe^{3+}/Fe^{2+} ratio in natural ilmenite ($FeTiO_3$) minerals”. In: *Journal of Physics: Condensed Matter* 16.15 (2004), p. 2707.

[77] N. Lee et al. “Probing valence orbital composition with iron Kβ X-ray emission spectroscopy”. In: *Journal of the American Chemical Society* 132.28 (2010), pp. 9715–9727.

[78] M. Wilke et al. “Oxidation state and coordination of Fe in minerals: An Fe K-XANES spectroscopic study”. In: *American Mineralogist* 86.5-6 (2001), pp. 714–730.

[79] J. Crocombette et al. “X-ray-absorption spectroscopy at the Fe $L_{2,3}$ threshold in iron”. In: *Physical Review B* 52.5 (1995), p. 3143.

[80] M. Benfatto et al. “Double-channel excitation in the X-ray absorption spectrum of Fe^{3+} water solutions”. In: *Chemical Physics* 282.3 (2002), pp. 441–450.

[81] A. Ludi. “Prussian blue, an inorganic evergreen”. In: *Journal of chemical education* 58.12 (1981), p. 1013.

[82] W. Zajac et al. “EVOLUTION OF MICROSTRUCTURE AND PHASE COMPOSITION UPON ANNEALING OF $LiFePO_4$ PREPARED BY A LOW TEMPERATURE METHOD”. In: *Functional Materials Letters* 4.02 (2011), pp. 117–122.

[83] G. Subías et al. “Investigation of pressure-induced magnetic transitions in $Co_xFe_{3-x}O_4$ spinels”. In: *Physical Review B* 87.9 (2013), p. 094408.

[84] H. Williamson. *Magnetic and charge order in $LuFe_2O_4$ and $YbFe_2O_4$ multiferroics*. 2012.

[85] J. Herrero-Martín et al. “X-ray absorption spectroscopic study on A_2FeReO_6 double perovskites”. In: *Journal of Physics: Condensed Matter* 17.33 (2005), p. 4963.

[86] T. Alamelu et al. “Structural and magnetic properties of $(Sr_{2-x}Ca_x)FeReO_6$”. In: *Journal of applied physics* 91.10 (2002), pp. 8909–8911.

[87] T. Sunaga et al. “Mössbauer study on a triangular lattice antiferromagnet $LuFeCoO_4$”. In: *Journal of the Physical Society of Japan* 70.12 (2001), pp. 3713–3718.

[88] M. Etter et al. “High-pressure phase transitions in the rare-earth orthoferrite $LaFeO_3$”. In: *Acta Crystallographica Section B: Structural Science, Crystal Engineering and Materials* 70.3 (2014), pp. 452–458.

[89] J.-R. Huang and C. Cheng. “Cation and magnetic orders in $MnFe_2O_4$ from density functional calculations”. In: *Journal of Applied Physics* 113.3 (2013), p. 033912.

[90] S. Lafuerza Bielsa. *X-ray absorption spectra using multiple scattering theory. Application to the $LaFe_{1-x}Ga_xO_3$ series*. 2010.

[91] J. Ma et al. “Role of magnetic exchange energy on charge ordering in $R_{1/3}Sr_{2/3}FeO_3$ (R= La, Pr and Nd)”. In: *Physical Review B* 84.22 (2011), p. 224115.

[92] J. Yang et al. “Charge disproportionation and ordering in $La_{1/3}Sr_{2/3}FeO_{3-\delta}$”. In: *Journal of Physics: Condensed Matter* 15.29 (2003), p. 5093.

[93] R. Alonso Mori et al. “Electronic structure of sulfur studied by X-ray absorption and emission spectroscopy”. In: *Analytical Chemistry* 81.15 (2009), pp. 6516–6525.